

THESIS

WIDEBAND NEAR-FIELD ARRAY SIGNAL PROCESSING USING THE SPARSE  
REPRESENTATION FRAMEWORK

Submitted by

Amanda Dinstel

Department of Electrical and Computer Engineering

In partial fulfillment of the requirements

For the Degree of Master of Science

Colorado State University

Fort Collins, Colorado

Fall 2012

Master's Committee:

Advisor: Mahmood R. Azimi-Sadjadi

Edwin Chong

Ali Pezeshki

Jay Breidt

## ABSTRACT

### WIDEBAND NEAR-FIELD ARRAY SIGNAL PROCESSING USING THE SPARSE REPRESENTATION FRAMEWORK

Recently, the field of sparse representation has attracted a great deal of attention from the perspective of target bearing (angle of arrival) estimation. This strategy takes the approach that a target present in a sensor array's field of view may be treated as a sparse signal, e.g. if a discrete grid is defined over the search area, very few of the points in the grid will contain sources. Source localization then reduces to identifying the sparse grid point(s) which correspond to the highest concentration of energy. Tools from the sparse representation framework may be used to provide exceptionally high resolution solutions to this localization problem. In this work, existing sparse representation-based localization concepts are evaluated and extended for use in the specific application of detection and localization of wideband near-field targets in sonar data.

While sparse representation offers a high-resolution detection and localization solution, the application of sparse representation-based techniques to the specific problem of sonar signal processing is challenging for several reasons. First, the general sparse representation-based angle of arrival problem formulation arises from a far-field array signal model, which allows source localization to be framed as a problem of identifying the unknown angle of arrival of sources in the search region. In contrast, the underwater targets under consideration in this work lie in the near-field which necessitates consideration of the unknown target range in addition to the unknown bearing angle. Second, a majority of current studies in the field of sparse representation-based source localization focus on narrowband signal processing. A handful of researchers have explored the extension of sparse recovery to the wideband problem, but most of these approaches require assumptions about the structure (i.e. sparsity profile) of the data, and these assumptions are not applicable to the sonar returns studied in this work. Further, sparse representation-based source localization methods

suffer from many of the same limitations as traditional sonar processing techniques, such as sensitivity to the effects of sonar platform motion and other sources of measurement error. Such uncertainties may present themselves as perturbations in the observed data, mismatch of the defined search grid, or both, and ultimately serve to degrade the performance of sparse representation-based source localization algorithms.

In this work, a near-field, wideband array signal processing method is developed which seeks to overcome these challenges inherent to sonar signal processing by expanding on existing concepts from the sparse representation framework. A comprehensive study was performed to evaluate the capabilities of the proposed sonar processing method for detection and localization of targets present in two sonar data sets, namely the Pond Experiment 2012 (PondEx10) data set, which was collected in a man-made pond facility using a rail-mounted sonar system, and the Davis Point data set, which was collected using the current generation buried object scanning sonar (BOSS) system. Sparse representation-based images were generated using two approaches. In the first, the effects of platform motion and other uncertainties were neglected, while in the second a mismatch compensation algorithm was incorporated to attempt to compensate for basis mismatch introduced by sonar platform motion and other non-ideal effects.

## TABLE OF CONTENTS

ABSTRACT . . . . .	ii
LIST OF TABLES . . . . .	v
LIST OF FIGURES . . . . .	vi
1 INTRODUCTION . . . . .	1
1.1 Problem Statement and Motivations . . . . .	1
1.2 Literature Review . . . . .	4
1.2.1 Traditional Sonar Array Processing . . . . .	4
1.2.2 Sparse Representation for Target Detection and Localization . . . . .	9
1.3 Research Objectives and Contributions . . . . .	12
1.3.1 Detection and Localization of Underwater Targets using the Sparse Representation Framework . . . . .	12
1.3.2 SAS-like Image Generation with Platform Motion and Other Uncer- tainties . . . . .	13
1.3.3 Evaluation of Developed Methods . . . . .	13
1.4 Thesis Organization . . . . .	14
2 A REVIEW OF SPARSE REPRESENTATION METHODS . . . . .	16
2.1 Introduction . . . . .	16
2.2 Sparse Representation Problem . . . . .	17
2.3 Measuring Sparsity: The Convexity Problem . . . . .	18
2.4 Recovery of a Unique Sparse Solution . . . . .	20
2.5 Sparse Solution Methods . . . . .	21
2.5.1 Greedy Algorithms . . . . .	22

2.5.2	Convex Relaxation Techniques . . . . .	23
2.6	Conclusions . . . . .	26
3	SONAR SYSTEMS AND DATA PROPERTIES . . . . .	27
3.1	Introduction . . . . .	27
3.2	Pond Setup and Data Set . . . . .	27
3.2.1	Pond Facility and Data Collection System . . . . .	28
3.2.2	PondEx10 Data Set and Properties . . . . .	29
3.3	BOSS System and Data Set . . . . .	33
3.3.1	Buried Object Scanning Sonar . . . . .	33
3.3.2	Davis Point Data Set and Properties . . . . .	36
3.4	Data Preprocessing . . . . .	39
3.5	Conclusions . . . . .	46
4	DETECTION AND LOCALIZATION USING SPARSE REPRESENTATION . . . . .	49
4.1	Introduction . . . . .	49
4.2	Sensor Array Processing as a Sparse Representation Problem . . . . .	50
4.3	Near-Field Narrowband Array Signal Model - 1D Case . . . . .	54
4.3.1	Near-Field Array Signal Model . . . . .	54
4.3.2	Near-Field to Far-Field Transformation . . . . .	56
4.3.3	Near-Field Angle of Arrival Estimation as a Sparse Representation Problem . . . . .	59
4.3.4	Simulations Demonstrating the 1D Near-Field Narrowband Detection and Localization Method . . . . .	61
4.4	Extension to Wideband Signals . . . . .	65
4.5	Near-field Narrowband Array Signal Model - 2D Case . . . . .	68
4.6	Conclusions . . . . .	73

5	EXPERIMENTAL RESULTS ON SONAR DATA . . . . .	75
5.1	Introduction . . . . .	75
5.2	Subarray Formation . . . . .	76
5.3	Localization of Targets in PondEx10 Data Set . . . . .	77
5.4	Localization of Targets in Davis Point BOSS Data Set . . . . .	80
5.5	Conclusions . . . . .	82
6	BASIS MISMATCH INHERENT TO SONAR ARRAY PROCESSING . . . . .	85
6.1	Introduction . . . . .	85
6.2	Sparsity Cognizant Total Least-Squares . . . . .	88
6.3	Localization of Targets in Davis Point BOSS Data Set . . . . .	93
6.4	Conclusions . . . . .	97
7	CONCLUSIONS AND SUGGESTIONS FOR FUTURE WORK . . . . .	99
7.1	Summary and Conclusions . . . . .	99
7.1.1	Detection and Localization Using Sparse Representation . . . . .	100
7.1.2	SAS-like Image Generation with Platform Motion . . . . .	102
7.2	Future Work . . . . .	103
	REFERENCES . . . . .	106

## LIST OF TABLES

3.1	List of targets used in Pond Experiment 2010 measurements. . . . .	32
3.2	Targets deployed during PondEx10 proud configuration measurements. . . .	32
3.3	Description of the PondEx10 data sequences. . . . .	33
3.4	Description for each object in the BOSS data set. OD = outside diameter. .	37

## LIST OF FIGURES

1.1	From a sparse representation perspective, target objects are treated as sparse sources lying in a search grid which is defined with respect to the position of the sensor array. . . . .	2
2.1	The behavior of $ x ^p$ (the core of the norm computation) for various values of $p$ . Note that as $p$ tends towards zero, $ x ^p$ approaches the indicator function, which can be thought of as a counter. . . . .	20
2.2	Mutual coherence for dictionaries formed using sensor arrays of varying length. For all cases, angle range of $\theta = -\pi/4 - \pi/4$ and angle grid resolution of $\pi/720$ are used. . . . .	24
3.1	Aerial view of the NSWCCD pond facility. . . . .	29
3.2	Layout of the PondEx10 target field (top view). . . . .	30
3.3	Six-element hydrophone array that is part of the first sonar system in the pond facility. . . . .	31
3.4	Objects in PondEx10 target field. . . . .	31
3.5	Target orientations for each PondEx10 data sequence. . . . .	34
3.6	LFM transmit signal and its frequency response. . . . .	35
3.7	Bluefin 12 UUV with wing BOSS payload (courtesy of the FAU Department of Ocean Engineering). . . . .	36
3.8	Layout of the Davis Point target field. . . . .	37
3.9	Raw and matched filtered versions of a typical sonar return from the Davis Point data set. . . . .	41
3.10	Images of all raw and matched filtered sonar returns for line T4e of the Davis Point data set. . . . .	42
3.11	Block diagram of the preprocessing steps used for sparse representation-based target detection and localization. . . . .	43

3.12	Windowed matched filtered signal for ping 300 of line T4e of the Davis Point data set. . . . .	45
3.13	Fixed versus dynamic starting locations for the ideal window. . . . .	47
3.14	Inverse filtered and windowed signal for ping 300 of line T4e of the Davis Point data set. . . . .	48
4.1	A comparison of far-field and near-field signal models. . . . .	50
4.2	Uniform linear subarray for 1D angle of arrival estimation. . . . .	54
4.3	For a fixed source angle of arrival, $\theta_i$ , the difference between the ranges to respective elements in two subarrays does not vary dramatically with range. Note the similar magnitude of $r_{y,m,i} - r_{x,m,i}$ in 4.3(a) and 4.3(b), despite the disparity in range, $r_i$ , for the two cases. . . . .	57
4.4	Using a dual subarray geometry allows the source range to be neglected, rendering the angle estimation problems at $h_1$ and $h_2$ equivalent. . . . .	58
4.5	Two example 1D angle of arrival grids projected onto the seafloor. . . . .	61
4.6	Overlapping azimuth and elevation dictionaries may be projected onto the seafloor to achieve 2D localization. However, when a linear subarray model is used, the two sparse representation problems must be solved separately. . . . .	62
4.7	Least-squares approximation of $ \Gamma_{0_i} $ when $M = 20$ . . . . .	64
4.8	Least-squares approximation of $ \Gamma_{0_i} $ when $M = 6$ . . . . .	64
4.9	OMP estimation of $ \Gamma_{0_i} $ when $M = 20$ . . . . .	65
4.10	OMP estimation of $ \Gamma_{0_i} $ when $M = 6$ . . . . .	65
4.11	Uniform planar subarray geometry for 2D angle of arrival estimation. . . . .	70
4.12	2D angle grid formed by using dual symmetric planar subarrays projected onto seafloor. . . . .	72
5.1	PondEx10 data set subarray construction and averaging operation. . . . .	77
5.2	BOSS Davis Point data set subarray construction and averaging operation. . . . .	78
5.3	Target localization for PondEx10 run 185. . . . .	79

5.4	Target localization for PondEx10 run 191. . . . .	81
5.5	Azimuth angle estimation for BOSS Davis Point run T4. Top: angle estimation using least-squares approximation. Bottom: conventional delay-and-sum SAS image. . . . .	82
5.6	Azimuth angle estimation for BOSS Davis Point run T10. Top: angle estimation using least-squares approximation. Bottom: conventional delay-and-sum SAS image. . . . .	83
5.7	Azimuth angle estimation for BOSS Davis Point run T3. Top: angle estimation using least-squares approximation. Bottom: conventional delay-and-sum SAS image. . . . .	83
6.1	The effects of platform instability and other uncertainties on dictionary construction and sparse representation target localization. . . . .	86
6.2	Azimuth angle estimation for BOSS Davis Point run T4. Top: angle estimation using WSS-TLS framework and coordinate descent solver. Middle: angle estimation using least-squares approximation. Bottom: conventional delay-and-sum SAS image. . . . .	94
6.3	Azimuth angle estimation for BOSS Davis Point run T10. Top: angle estimation using WSS-TLS framework and coordinate descent solver. Middle: angle estimation using least-squares approximation. Bottom: conventional delay-and-sum SAS image. . . . .	95
6.4	Azimuth angle estimation for BOSS Davis Point run T3. Top: angle estimation using WSS-TLS framework and coordinate descent solver. Middle: angle estimation using least-squares approximation. Bottom: conventional delay-and-sum SAS image. . . . .	96

# CHAPTER 1

## INTRODUCTION

### 1.1 Problem Statement and Motivations

Target detection and localization based on phased-array data processing are extremely useful in many areas, with particularly important applications in the fields of radar and sonar [1] - [15]. Using phased array processing, signals from an array of antennae/sensors may be combined into a single output signal in a manner that yields directional sensitivity for the system. This technique establishes an effective receptive conduit in some desired direction, while ideally suppressing signals propagating from other directions. The fundamental principle that provides this directional selectivity is to coherently combine the received signals in some manner and then find the total signal energy associated with source(s) located in some given direction. This technique can be used to determine the true direction of a signal source by systematically varying the ‘look angle’ to find maximum signal strength.

Such phased array processing approaches are prevalent in the fields of radar, where applications include determining the range, altitude, direction or speed of objects [1,25], and in sonar, where targets of interest may include natural and/or man-made underwater objects, and applications vary from biological surveys to military defense efforts [1]- [7], [51]. In the context of the work presented in this thesis, the specific target objects of interest are buried and/or proud underwater mine-like objects, and the data collection systems in use consist of linear sonar (hydrophone) arrays.

The problem of target detection in sonar returns is challenging due to several factors, including the presence of natural and man-made clutter, bottom reverberation effects, and the variability of target signatures with respect to the incident angle and range of the sonar transmitter(s). Accurate target localization is often made challenging by the effects of sensor array motion and other measurement uncertainties, as well as by resolution limitations inherent to existing array processing methods. In this work, a sonar imaging solution is

sought which provides robust target detection capabilities as well as improved localization resolution as compared to conventional array processing algorithms.

Recently, the field of sparse representation has attracted a great deal of attention from the perspective of target bearing (angle of arrival) estimation [23] - [30]. This tactic takes the approach that a target present in a sensor array's field of view may be treated as a sparse signal. e.g. if a discrete grid is defined over the search area, very few of the points in the grid will contain sources. The source signals present are sparse in the predefined search grid, allowing tools from the sparse representation framework to be utilized. This concept is illustrated in Figure 1.1.

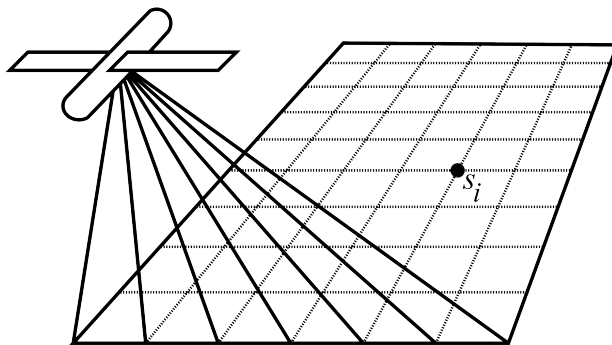


**Figure 1.1:** From a sparse representation perspective, target objects are treated as sparse sources lying in a search grid which is defined with respect to the position of the sensor array.

In the work of [23] - [30], angle of arrival estimation using a sensor array is posed as a sparse representation problem. It is further demonstrated [24, 25] that such a sparse representation-based array processing method may achieve improved localization resolution as compared to the limitations of classical sonar beamforming. Unfortunately, sonar data processing presents specific challenges which hinder the direct application of such methods. For example, existing sparse representation-based methods arise from a far-field point source model. Source localization is then achieved by defining a discrete grid of possible source bearing angles and then seeking a sparse solution to the underdetermined system of equations

that results from this formulation. In contrast to this, sonar data is generally near-field and therefore the resulting problem formulation must take into consideration the unknown source range as well as the unknown angle of arrival. As an additional challenge, existing sparse representation-based methods like those of [23] - [30] consider narrowband sources, whereas the sonar data underconsideration is wideband. Further, the successful implementation of sparse representation-based target bearing estimation is highly dependent on the target(s) lying exactly on a precise search grid which is defined with respect to the position of the sensor array. For a scenario where the position of the sensor array is strictly fixed, and the various measurement uncertainties may be accurately quantified, such a sparse representation-based approach may be very useful. However, many of the effects present in sonar data, such as variable seafloor contour, array platform motion, and other sources of measurement error introduce an apparent mismatch between the true sensor array position and the assumed sensor array position that is used to define the discrete search grid. For this reason, much of the existing work in the area of sparse representation-based target localization is geared towards array signal processing applications where the sensor array is stationary, which limits the usefulness of existing sparse solution algorithms in detection and localization of buried and proud underwater targets. The work presented in this thesis aims to provide a sonar array processing technique which utilizes sparse representation-based bearing estimation in order to achieve improved localization resolution, and which also addresses the various complications specific to sonar signal processing.

The research presented in this thesis is part of a project sponsored by the Office of Naval Research (ONR-32MCM). The remainder of this chapter provides a brief introduction to the driving factors behind this ONR study. Section 1.2 provides a survey of previous efforts in the areas of real and synthetic aperture sonar processing, and of existing work in the area of target localization using sparse representation techniques. Section 1.3 summarizes the specific objectives of this research, and Section 1.4 describes the organization of the remainder of this thesis.

## 1.2 Literature Review

In this section, a survey of existing work related to the efforts in this project is presented. First, a selection of common sonar array processing methods are compared and contrasted. Various inadequacies of these traditional methods are illuminated, which helps to motivate the development of a new sonar imaging method to address these shortcomings. Then, a summary of existing work in the area of sparse-representation-based target localization is provided.

### 1.2.1 Traditional Sonar Array Processing

As is discussed in [1], utilizing signals from a single sensor only allows for temporal processing, while incorporating data from an array of sensors allows for processing over both a temporal and spatial aperture, yielding both frequency and spatial selectivity. As mentioned previously, the fundamental principle that provides this selectivity is constructive (and destructive) interference that occurs when the signals collected by a sensor array are coherently combined. The result is that signals from a direction of interest are left unchanged, while signals propagating from other directions are ideally attenuated; this collective class of array processing methods is called beamforming. Beamforming algorithms can be divided into two general categories: conventional beamforming methods [1,4], and modern beamforming methods [1–3].

Conventional beamforming techniques are defined as those which yield fixed, non-varying beam patterns. These procedures are not dependent on the signal and noise properties (i.e. they do not adapt to changing characteristics of the acoustic environment) and therefore are computationally simple. Two major drawbacks of conventional methods are illuminated in [1]. First, for conventional beamforming methods which combine signals from real aperture elements, the beamwidth (and therefore spatial resolution) of the beamformer is dictated by the length of the array. These systems are generally incapable of discriminating between closely spaced targets. Secondly, conventional beamformers exhibit beam patterns with high side lobes. This lack of side lobe attenuation can result in signals of interest being masked

by interference impinging from directions corresponding to the high side lobes. (In fact, many sonar “jamming” mechanisms attempt to exploit the characteristic high side lobes of conventional beamformers.)

The second area of beamforming, modern beamforming, is a class of methods that seek to address these and other shortcomings of conventional beamformers [1] - [4]. Modern beamforming algorithms (often referred to as adaptive beamformers) share the common characteristic that they attempt to improve on conventional methods by incorporating information from the environment in order to produce more capable beam patterns. The work of [1] - [3] present a selection of adaptive beamforming approaches, each of which operate on the spatial correlation matrix of the sensor output data. In many adaptive beamforming methods this matrix is used to compute a vector of weight coefficients which are applied to the sensor array signals to provide adaptive attenuation and ideally an improved beam pattern with better sidelobe attenuation.

An example of a modern beamformer is the multiple sidelobe canceller [1] which computes the weight vector using the data correlation matrix and a signal from a main physical channel. The multiple sidelobe canceller exploits the correlation of the interfering signals between the main and auxiliary channels, which ultimately steers nulls in the directions of the interfering signals. While simple and effective, this method requires a specific sensor arrangement to provide main and auxiliary channels, which is a limiting factor for this approach.

Minimum variance-based approaches [3], on the other hand, place no requirements on the sensor array configuration. In this class of beamformers, the beam steered to direction  $\theta$  is formed by minimizing the array output power variance subject to the constraint that the gain at angle  $\theta$  is unity. The resulting expression for the adaptive weight vector is  $\mathbf{w} = \frac{\mathbf{R}^{-1}\mathbf{a}(\theta)}{\mathbf{a}(\theta)^H\mathbf{R}^{-1}\mathbf{a}(\theta)}$  where  $\mathbf{R}$  is the data covariance matrix and  $\mathbf{a}(\theta)$  denotes the array steering vector. Minimum variance approaches maximize the signal-to-noise ratio when the signal propagates from the direction  $\theta$ .

Another class of array processing methods which shares many similarities to beamforming is spatial spectrum analysis [1], [11]- [15]. While not strictly beamforming, this class of techniques also provide estimates of the arrival direction and power of signals impinging on an array of hydrophones. These methods do not utilize beamformer weights, but instead perform a spatial spectrum analysis directly on the sensor data. This class of array signal processing techniques can improve upon the cross-range resolution capabilities of conventional beamforming approaches using moderately sized arrays. When a linear array geometry is used, angle of arrival may be estimated in a single dimension (i.e. azimuth or elevation). Two-dimensional localization (i.e. simultaneous azimuth and elevation estimation) may readily be achieved using spectral analysis methods if a planar array geometry is adopted.

Much like traditional beamforming algorithms, spatial spectrum analysis estimates the angle of arrival and power of signals impinging on a sensor array. Generally, the signal correlation matrix is used as a measure of energy. The algorithms of [11] - [15] all utilize eigenvalue decomposition of the correlation matrix in order to estimate the arrival angle corresponding to the highest signal power. One such algorithm, multiple signal classification (MUSIC), is an eigenstructure-based approach that can provide resolution performance far exceeding that obtained through traditional beamforming [1]. It does not involve any array weighting, but instead processes the unaltered sensor data directly. The MUSIC techniques involve the decomposition of the spatial correlation matrix into its constituent eigenvalues and eigenvectors. Under the assumption of white noise, MUSIC shows that the smallest eigenvalues correspond to contributions from noise, and the largest eigenvalues correspond to signals impinging on the sensor array.

Synthetic aperture sonar (SAS) processing [4] - [9] allows for generating an “optical-like” sonar image of the seafloor from which one can perform object detection and localization. SAS images are intensity representations of the backscattered acoustic energy from a specific range and aspect angle. Synthetic aperture techniques use coherent combination over many

pings to create a longer effective aperture and therefore provide higher along-track resolution than those of standard methods. Implementation of SAS is made challenging by a number of factors, including the lack of coherence of the ocean medium, the effects of motion and measurement errors during data collection, and burdensome processing requirements. SAS imaging, which relies on the coherent combination of data from consecutive pings, is especially sensitive to the effects of platform motion and instability; however, with advances in motion-compensation techniques and computational capabilities, SAS has become a broadly-used technology in commercial and military seafloor imaging systems.

One straight forward approach is to incorporate measurements from inertial sensors into the SAS processing, allowing exact compensation for the motion of the data acquisition system. Algorithms such as those in the delay-and-sum family of SAS processing approaches [4,5] incorporate measured motion data in order to correct for motion-induced measurement errors and allow for coherent combination of the sensor array signals. Other strategies attempt to minimize the need for inertial sensors by estimating the sonar platform motion directly from the measured data. Examples of this class of approaches include the displaced phase center antenna (DPCA) algorithms (sometimes referred to as micronavigation) [18], [20] - [21], and autofocusing algorithms [19]. The basic idea of DPCA is to cancel the along-track ping-to-ping displacement of the sonar platform by synthesis of an effective displacement in the opposite direction using a subset of receiving elements. DPCA algorithms are less capable of handling the effects of motion in the cross-track direction. Autofocusing algorithms are similar to DCPA, and attempt to estimate and remove distortion in the image from the measured data. Typically, these approaches consist of creating images at consecutive pings using overlapping sensor apertures, and then combining these consecutive images in a way which produces maximum image intensity. One such autofocusing method is shear-averaging which works by exploiting redundant sea-floor clutter information captured by consecutive pings [22].

Recently, SAS-like methods have been developed that are more robust to motion effects and other sources of error. The goal of these methods is to provide imaging solutions with resolution comparable to that achievable using conventional SAS, while requiring little or no motion estimation and compensation. As an example, in [7] - [9] several methods are introduced which use a coherence analysis framework to generate SAS-like images that display acoustic color information. In contrast to conventional SAS processing, where coherency is achieved by estimating and compensating for the propagation time differences between the signals captured by each hydrophone element at each ping, the coherence analysis methods of [7] achieve coherency by linear transformation of the hydrophone data channels in the frequency domain. Specifically, the dominant canonical correlations of the mapped sonar data capture this coherency by correcting for all the propagations errors via canonical coordinate mappings. Further, because this canonical correlation analysis (CCA) algorithm [7] is applied to individual frequency ranges of the data separately, the resulting SAS-like images retain spectral information at each ping. In [7], this frequency-dependent information is used as a means of classifying objects (mine-like vs. non-mine-like) in sonar returns, demonstrating that this SAS-like processing approach is useful for target classification as well as localization.

To summarize, many strategies exist for handling sonar array data, each with their own advantages and disadvantages. Conventional beamforming methods [1] suffer from limited resolution and are susceptible to the effects of parasitic interference signals due to beam patterns with characteristically high side lobes. Adaptive beamforming algorithms [1]- [3] may be used to improve side lobe attenuation by incorporating information about the acoustic environment, but still suffer from resolution limitations related to the physical size of the sensor array. Synthetic aperture sonar (SAS) methods [4] - [6] are able to achieve dramatically better along-track resolution than traditional real-aperture methods by coherently combining data from multiple successive pings to give an optical-like intensity image of the seafloor. However, a significant drawback of SAS processing is that it is highly sensitive to

array platform motion and other sources of measurement error (such as that introduced by seafloor clutter, variable bottom contour, etc). In order to coherently combine successive ping information using SAS, compensation for the ping-to-ping differences in platform position is required. As such, SAS implementations often require either expensive inertial sensors and computationally intensive data pre-processing steps, or complicated, processor-intensive algorithms which seek to estimate the array motion directly from the data and compensate for these errors during construction of SAS images.

### 1.2.2 Sparse Representation for Target Detection and Localization

Assessing the various array signal processing strategies presented in the previous section motivates the development of an approach that leverages concepts from SAS to provide intensity images with good along-track resolution, as well as from spectral analysis array processing methods which are far more capable of resolving closely-spaced targets than traditional beamforming methods. Recently, it has been proposed that solution methods from the sparse representation framework might offer high resolution target localization capabilities [23] - [30]. These methods bear many similarities to high resolution spectral analysis in that for both approaches the general idea is to estimate arrival direction and power of signals impinging on an array of sensors, and the measure of power used is typically the signal covariance matrix. However, whereas most spectral analysis methods utilize eigenvalue decomposition approaches to find the arrival angle and signal power, the sparse representation class of approaches pose source localization as a sparsity-constrained underdetermined linear systems problem. To paraphrase the authors of [23], casting this problem using an overcomplete representation (e.g. as an underdetermined problem) allows us to exchange the problem of parameter estimation of the angle of arrival for the problem of sparse spectrum estimation of the source signal.

As was discussed earlier, the problem of source localization using sparse representation can be posed as searching for the candidate grid point(s) which corresponds to the maximum signal power. As a simplistic example, assume that the angle grid (or equivalently the grid of

spatial coordinates), can be represented by an  $M \times N$  dictionary matrix,  $\mathbf{A}_0$ , with  $M \ll N$ . Then, the signal power may be captured by a sparse length  $N$  vector,  $\Gamma_0$ . Then, given a measurement vector,  $\mathbf{b}$ , the problem can be cast into finding a sparse solution for an underdetermined system of equations,

$$\mathbf{b} = \mathbf{A}_0\Gamma \tag{1.1}$$

Note that here it is assumed that measurement noise is absent. Thus, the goal becomes to recover the sparse vector,  $\Gamma_0$ . Important recent developments [34] - [39] in this field have provided an increased understanding of this problem and several classes of solutions approaches have been developed for finding sparse solutions of (1.1).

The notion of posing target localization as a sparse representation problem has been addressed in several recent papers [23] - [30]. However, much of this work has focused on comparing and contrasting sparse solution algorithms for the general source localization problem. For example, [23] uses a far-field narrowband signal model to derive a problem formulation like that of (1.1) with the addition of Gaussian noise. A solution approach based on  $\ell_1$ -norm penalization is then proposed. In [24], the problem formulation of (1.1) is considered, and the FOcal Underdetermined System Solver (FOCUSS) algorithm [24] is used to localize the sources. The work in [25] uses a far-field point scattering model to develop an underdetermined linear systems problem like that of (1.1), and proposes that if the dictionary,  $\mathbf{A}_0$ , is constructed appropriately, a superresolution approximation of source angle of arrival may be estimated using an iteratively-weighted least-squares approach [25].

Sonar signal processing presents a unique set of challenges for the implementation of sparse representation methods, and at this time, very little work has been done in applying sparse representation-based methods to the specific application of underwater target detection using sonar arrays. Specifically, sonar returns are typically wideband and emanate from near-field (i.e. sea floor), whereas the majority of available results are derived from

far-field narrowband signal models. Only a handful of currently available studies have extended the sparse representation framework beyond the general source localization problem. The works of [26] - [28] pose the wideband source localization problem as a ‘joint-sparsity’ problem. From the joint-sparsity perspective, it is assumed that each frequency present in the wideband signal will exhibit the same sparsity profile, and this assumption is exploited to develop a sparse solution algorithm based on a mixed  $\ell_0/\ell_2$ -norm minimization approach. Each method in [26] - [28] starts with a similar wideband signal model, and under the assumption of joint-sparsity, develops a sparse solution method that leverages on ideas from the field of ‘block sparsity’. It has been shown that exploiting the block-sparse structure of signals can yield better reconstruction properties than treating the signal as being sparse in the conventional sense [72]. While this strategy may offer a promising means for handling some classes of wideband signals, the assumption of joint-sparsity across all frequency bands does not necessarily hold for sonar signals (as will be demonstrated in the results of Chapter 5).

The works of [29] and [30] consider the specific problem of angle of arrival estimation for sonar targets. However, [29] models the sonar returns as far-field signals, which does not adequately characterize most underwater sonar data. The work in [30], which was a precursor to the work described in this thesis, developed a near-field signal model for use in sonar target localization, but only arrived at a narrowband signal processing algorithm. While sparse representation offers a promising high resolution sonar signal processing strategy, there is an apparent lack of information available for this specific application at this time. This knowledge gap provides ample opportunity for development and expansion of SAS sonar imaging techniques based on the sparse representation framework.

Chapter 2 of this thesis reviews the current work in the field of sparse representation [34] - [45], and discusses the requirements for recovery of a unique and convergent sparse solution. In general, the ability to reconstruct a sparse solution relies on two factors: 1) the sparseness of the solution,  $\Gamma_0$ , and 2) the structure of the overcomplete basis,  $\mathbf{A}_0$ .

### 1.3 Research Objectives and Contributions

#### 1.3.1 Detection and Localization of Underwater Targets using the Sparse Representation Framework

As previously mentioned, the existing work demonstrated the usefulness of a sparse representation approach to target detection and localization. However, these methods concentrated almost exclusively on the detection of narrowband far-field sources, rendering them insufficient to address the specific problem of detecting and localizing underwater targets in sonar data, which are typically near-field and wideband. Therefore, a primary objective of this work is the development of a sparse representation-based detection and localization scheme with specific applications in detection of underwater targets. Development of this method involves extending the existing body of work in two specific ways. First, the new method must allow for the detection and localization of *near-field* sources. In this work, a near-field array processing approach is developed using techniques like those of [59] - [61] which demonstrate that by performing localization using symmetric subarrays, a transformation is yielded which exhibits the far-field-like rotational invariance property. That is, the near-field target detection problem may be transformed into a problem which may be solved using existing far-field approaches. Second, the new method must be useful for *wideband* sonar data. Several alternative means exist for addressing this requirement. However in this research, the extension from existing narrowband processing methods to a more capable wideband approach is accomplished using a frequency focusing method reminiscent of that presented in [66] and [67]. In these references, a transformation operation is applied to the data at each frequency, thereby transforming all data to one effective frequency prior to incoherent combination. In this work, it is demonstrated that such a frequency transformation approach may be rather elegantly combined with the sparse representation-based target localization algorithm to give a wideband processing approach that is simple to implement and highly computationally effective.

Ultimately, this work addresses these two significant shortcomings of the existing sparse representation-based target localization methods, and provides a sparse solution algorithm which may be useful to *wideband near-field* sonar data.

### **1.3.2 SAS-like Image Generation with Platform Motion and Other Uncertainties**

Like many traditional SAS methods, the currently available detection and localization work based on the sparse representation framework is highly susceptible to errors introduced by sonar platform motion and other uncertainties. Without addressing this deficiency, sparse representation-based methods offer little or no advantage over existing methods. Therefore, an important objective of this work is to develop an sparse representation-based processing approach which mitigates the effects of such uncertainties. In this research, a sparsity cognizant total least-squares algorithm [32] is considered which seek to address the issue of platform-motion-induced error. This approach treats motion error and other uncertainties as a case where the true target position can not be adequately represented by the predefined basis. That is, position estimation errors arise when the true target location does not lie exactly on the predefined search grid. This approach attempts to alleviate localization errors by defining a search grid which incorporates dynamically updated error parameters and is inherently more forgiving of this type of grid mismatch. In this thesis, the sparsity cognizant total least-squares algorithm is applied to a real sonar data set, specifically the Davis Point data set, which exhibits the effects of sonar array platform motion and other measurement uncertainties such as variable sea-floor roughness conditions.

### **1.3.3 Evaluation of Developed Methods**

The final objective of this research is to validate the developed methods by demonstrating their capabilities in detecting target objects in real sonar returns. Specifically, the SAS-like images generated using the proposed sparse representation-based detection algorithm are benchmarked against images generated using conventional delay-and-sum SAS processing [52, 53] and the SAS-like acoustic color processing of [7, 8]. The results of applying the

developed methods to two data sets, namely the Pond Experiment 2010 (PondEx10) and the Davis Point data sets, are evaluated and thoroughly discussed in this thesis.

## 1.4 Thesis Organization

The remainder of this thesis is organized as follows. Chapter 2 provides a survey of the fundamental principles of the sparse representation framework. The general sparse representation problem is presented, and the conditions and constraints for recovery of a unique sparse solution are discussed. Two specific sparse representation solution methods, which are implemented in this work, are reviewed in detail. Chapter 3 introduces the two wideband sonar data sets considered in this study, namely the (Pond Experiment 2010) PondEx10 data set, which was collected in a man-made pond facility under highly controlled data acquisition conditions, and the Davis Point data set, which was collected using a sonar array mounted to an unmanned underwater vehicle (UUV). Chapter 3 also describes the preprocessing steps applied to both the PondEx10 and Davis Point data sets in preparation for application of the target localization approach developed in this work. In Chapter 4, a detection and localization method for near-field targets is derived which leverages concepts from the sparse representation framework. This localization method is initially developed from a simple one-dimensional (1-D) narrowband signal model, resulting in a method capable of angle of arrival discrimination in a single plane (i.e. azimuth or elevation, depending on the orientation of the linear sensor array). Then, this method is extended to allow for two-dimensional (2-D) target localization (i.e. simultaneous azimuth and elevation). This chapter also presents a frequency focusing approach which is used to allow application of the proposed narrowband source localization method to wideband sonar data such as those of the PondEx10 and Davis Point data sets. Chapter 4 also provides simulation results which demonstrate application of the new target localization method on synthetic data. Chapter 5 presents the results of applying the proposed sparse representation-based localization method to both the PondEx10 and Davis Point data sets. These results are benchmarked against results obtained by delay-and-sum SAS processing and SAS-like acoustic color imaging. Chapter 6 discusses

the degrading effects of sonar platform motion and other sources of uncertainty on the performance of the detection and localization method, and evaluates a sparsity cognizant total least squares algorithm which attempts to minimize these effects. This mismatch compensation method is demonstrated on the Davis Point data set, which is inherently prone to the effects of sonar array motion and variant data acquisition and environmental conditions. Finally, Chapter 7 concludes the work presented in this thesis and discusses opportunities for continued work in this area.

## CHAPTER 2

### A REVIEW OF SPARSE REPRESENTATION METHODS

#### 2.1 Introduction

The underlying concept of sparse signal representation is to search for the most compact representation of a signal in terms of linear combinations of atoms in a predefined overcomplete dictionary. This topic has many important applications including feature selection [35, 36], signal restoration [34, 44], and super-resolution source localization [24, 25], among others. In the context of the work in this thesis, sparse representation is proposed as a candidate method for the problem of localizing underwater objects in sonar data. In this problem the objects of interest are considered to lie on an angle of arrival or spatial coordinate grid defined with respect to the position of the sensor array(s). In this manner the backscatter signals off of a target at a particular position are sparse with respect to the set of all possible positions in the predefined grid. Posing the localization problem in this way results in an underdetermined linear systems problem, which are generally considered to be intractable. However, with the added constraint that the solution must be sparse, a class of solution approaches from the sparse representation framework [34] - [43] is available for addressing this problem. This type of sparsity-constrained underdetermined linear systems problems has become a topic of increased interest in recent years, and only in the past decade have the fundamental conditions for sparse reconstruction become well-understood.

In this chapter, the fundamental theorems and proofs dictating the conditions for recovery of unique sparse solutions are briefly reviewed. In the work encompassed by this thesis, solution methods from the sparse representation framework are essentially treated as *tools*, and therefore this chapter is a substantially condensed representation of the body of theoretical work in this area. For more detailed information, the readers are referred to [34] - [46], among many other papers.

This chapter is organized as follows. First, the general underdetermined linear systems problem is presented in Section 2.2. A discussion is provided to describe how an underdetermined linear systems problem with a potentially infinite number of possible solutions may be reduced to a tractable problem in the case that the solution is sufficiently sparse. The notion of sparsity and the challenges associated with quantifying this measure are discussed in Section 2.3. Section 2.4 discusses the theoretical conditions for recovery of a sparse solution, and then several classes of solution finding methods are presented in Section 2.5, with specific emphasis being placed on the algorithms which are implemented in this work for the localization of underwater targets. Finally, concluding remarks on the topic of sparse representation are made in Section 2.6.

## 2.2 Sparse Representation Problem

The general sparse representation problem may be posed as follows. Given a full column rank matrix,  $\mathbf{A} \in \mathbb{R}^{M \times N}$  with  $M \ll N$ , consider the underdetermined linear system of equations,  $\mathbf{Ax} = \mathbf{b}$ . As defined, this system has infinitely many solutions. In order to narrow the choice to a unique solution, additional criteria must be imposed. One familiar approach is to define a function,  $J(\mathbf{x})$ , as a measure of the desirability of candidate solutions,  $\mathbf{x}$ . A general optimization problem may be defined as

$$\min_{\mathbf{x}} J(\mathbf{x}) \quad \text{subject to} \quad \mathbf{b} = \mathbf{Ax} \quad (2.1)$$

Selecting a strictly convex function  $J(\cdot)$  guarantees a unique solution, and one familiar approach is to select the Euclidean norm,  $\|\mathbf{x}\|_2^2$  or  $\ell_2$ -norm which is a measure of energy, and is in some cases a useful function to use. However, in the sparse representation framework, it is desirable instead to define a measure of the *sparsity* of the solution vector,  $\mathbf{x}$ . One straight forward measure of sparsity is the  $\ell_0$  “norm”, i.e.

$$\|\mathbf{x}\|_0 = \text{count}\{i : x_i \neq 0\} \quad (2.2)$$

which essentially provides a count of the number of non-zero elements in the vector  $\mathbf{x}$ . Thus, if  $\|\mathbf{x}\|_0 \ll N$ , the solution vector  $\mathbf{x}$  is “sparse”. However, unlike the  $\ell_2$ -norm solution which is always unique and can readily be computed using standard tools from linear algebra, the  $\ell_0$ -norm solution lacks intuitive insight to even the most basic questions, i.e. can a unique solution be obtained, and if so, under what conditions? Solving the  $\ell_0$ -norm optimization is a classical problem of combinatorial search. That is, it requires sweeping through all possible sparse candidate solutions, generating subsystems  $\mathbf{b} = \mathbf{A}_S \mathbf{x}_S$  (where  $\mathbf{A}_S$  denotes the matrix with  $|S|$  columns chosen from  $\mathbf{A}$ ), and checking whether  $\mathbf{b} = \mathbf{A}_S \mathbf{x}_S$  can be satisfied. The complexity of this exhaustive search is exponential with dimension  $N$  and it has been proven that, in general, this problem is NP-hard [46]. This debilitating limitation to resolving a sparse solution motivates the question of whether the  $\ell_0$ -norm problem may be solved by some other means. Recently, the body of work related to this question has grown immensely, with some examples in [34] - [46]. The results so far range from identifying conditions under which the problem has a unique solution, to conditions under which the sparsity measure may be approximated by the  $\ell_1$ -norm [43, 46] or even the  $\ell_2$ -norm [25], to conditions under which a solution may be reached by some “pursuit” algorithm [41, 44, 45].

### 2.3 Measuring Sparsity: The Convexity Problem

While the sparsity measure provided by the  $\ell_0$ -norm of (2.2) is rather intuitive, arriving at a measure of this quantity is challenging, and in many cases such a count of non-zero elements is not really the correct notion of sparsity. For instance, a vector of physical data will rarely be exactly representable by a vector of coefficients containing many strictly zero elements. A weaker notion of sparsity arises from the idea of approximately representing a vector using a small number of non-zeros and seeking to minimize the reconstruction error between this approximation and the original vector. This measure may be quantified using the weak  $\ell_p$  norms, which measure the tradeoff between the number of non-zeros, e.g. the sparsity, and the reconstruction error between the sparse solution and the measurement vector [35]. If we denote the number of entries in vector  $\mathbf{x}$  exceeding threshold  $\epsilon$  as  $N(\epsilon, \mathbf{x})$ ,

the weak  $\ell_p$  measures of sparsity are defined by

$$\|\mathbf{x}\|_{\text{weak}\ell_p} = \sup_{\epsilon > 0} N(\epsilon, \mathbf{x}) \cdot \epsilon^p. \quad (2.3)$$

The range  $0 < p \leq 1$  is the interesting range here, which gives a very powerful sparsity constraint. Nearly equivalent are the usual  $\ell_p$  norms, which are defined by

$$\|\mathbf{x}\|_p = \left( \sum_i |x_i|^p \right)^{1/p} \quad (2.4)$$

which for  $1 \leq p \leq \infty$  are familiar; however, for measuring sparsity the range  $0 < p < 1$  is of most interest.

Both the weak  $\ell_p$  norms and the usual  $\ell_p$  norms may be related to the sparsity measure of (2.2) [35] by recognizing that the  $\ell_0$  norm is the limit as  $p \rightarrow 0$  of the  $\ell_p$  norms in the following sense:

$$\|\mathbf{x}\|_0 = \lim_{p \rightarrow 0} \|\mathbf{x}\|_p^p = \lim_{p \rightarrow 0} \sum_{k=1}^m |x_k|^p. \quad (2.5)$$

This relationship illustrates that the count of non-zero elements in vector  $\mathbf{x}$  may be quantified by a familiar norm measure if we choose a  $p$  value that tends towards zero. Figure 2.1 presents the behavior of the function  $|x_k|^p$  for various values of  $p$ . It is clear from this illustration that as  $p$  approaches zero, the functional behavior approaches that of the indicator function. That is, the  $\ell_p$ -norm for  $p = 0$  behaves as a counter of non-zero elements in vector  $\mathbf{x}$ .

Unfortunately, as is apparent in Figure 2.1, the  $\ell_p$ -norm for  $0 < p < 1$  (the range of interest for our measure of sparsity) results in a non-convex function and an optimization problem which is generally NP-hard [46]. Inspecting the functional behavior of Figure 2.1 motivates two categories of strategies for tackling this challenging problem. The first group of strategies asks the question: may the  $\ell_p$ -norm solution for  $0 < p < 1$  be pursued in a manner that is computationally tractable? The resulting class of greedy algorithms [41,44,45] attempt to minimize the number of steps required to find the sparsest approximation of a

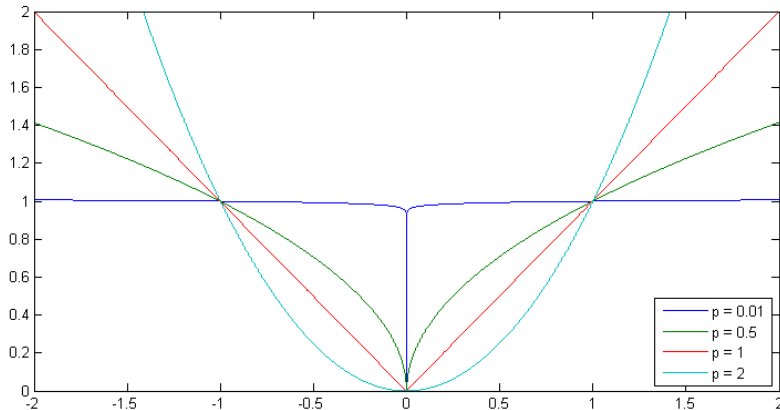


**Figure 2.1:** The behavior of  $|x|^p$  (the core of the norm computation) for various values of  $p$ . Note that as  $p$  tends towards zero,  $|x|^p$  approaches the indicator function, which can be thought of as a counter.

vector and avoid the complexity of combinatorial search. The second group asks: may the non-convex sparse solution be approximated by solving a convex optimization problem, i.e.  $\ell_p$ -norm for  $p \geq 1$ ? A central achievement of the sparse representation framework has been to characterize the fundamental connection between the non-convex  $\ell_0$ -norm and convex  $\ell_p$ -norm solutions, [34,35,38], and the result is a class of solution methods which employ convex relaxation [25,43,46] of the  $\ell_0$ -norm sparsity measure.

## 2.4 Recovery of a Unique Sparse Solution

In general, the ability to reconstruct a sparse solution relies primarily on two factors: 1) the sparseness of the solution,  $\mathbf{x}$ , and 2) the structure of the overcomplete basis,  $\mathbf{A}$ . In [25], it is shown that near-field source localization may be posed as a sparse representation problem due largely to the fact that angle of arrival estimation gives rise to a dictionary that adheres to the structural requirements necessary for recovery of a sparse solution. The sparse representation literature [34,35,38,46], highlights two concepts which help to define the conditions for recovery of unique sparse solutions. These are mutual coherence and the restricted isometry property of the dictionary matrix.

Mutual coherence of a given matrix  $\mathbf{A}$  is the largest absolute normalized inner product between different columns of matrix,  $\mathbf{A}$ . Denoting the  $k$ th column of  $\mathbf{A}$  by  $\mathbf{a}_k$ , the mutual

coherence is given by

$$\mu(\mathbf{A}) = \max_{1 \leq k, j \leq m, k \neq j} \frac{|\mathbf{a}_k^T \mathbf{a}_j|}{\|\mathbf{a}_k\|_2 \cdot \|\mathbf{a}_j\|_2}. \quad (2.6)$$

The mutual coherence essentially characterizes the dependence between columns in the dictionary,  $\mathbf{A}$ . In [34] and [35], conditions for recovery of a unique solution are framed in terms of the mutual coherence as follows. *If a system of linear equations  $\mathbf{A}\mathbf{x} = \mathbf{b}$  has a solution  $\mathbf{x}$  obeying  $\|\mathbf{x}\|_0 < \frac{1}{2}(1 + 1/\mu(\mathbf{A}))$ , this solution is necessarily the sparsest possible.*

The restricted isometry property [38] of matrix  $\mathbf{A}$  provides an alternative means for ensuring recovery of a unique sparse solution. An  $M \times N$  matrix  $\mathbf{A}$  is said to have the restricted isometry property  $RIP(\delta; k)$  if each submatrix  $\mathbf{A}_I$  formed by combining at most  $k$  columns of  $\mathbf{A}$  has its nonzero singular values bounded above by  $1 + \delta$  and below by  $1 - \delta$ , i.e.

$$(1 - \delta)\|\mathbf{x}\|_2^2 \leq \|\mathbf{A}_I \mathbf{x}\|_2^2 \leq (1 + \delta)\|\mathbf{x}\|_2^2. \quad (2.7)$$

Using this concept, [35, 37, 38] have shown that dictionaries construction exhibiting  $\mathbf{A} \in RIP(0.41; 2k)$  implies that the  $\ell_0$ -norm problem and the  $\ell_1$ -norm problem have identical solutions on all  $k$ -sparse vectors. The works of [36] and [37] discuss the kinds of matrices which satisfy the restricted isometry property.

## 2.5 Sparse Solution Methods

Several classes of solution approaches have been found to be capable of solving the  $\ell_0$ -norm problem under certain conditions. Here, two categories of solutions are described, namely the greedy algorithms, which abandon the exhaustive search for the solution of the  $\ell_0$ -norm problem in favor of performing a series of locally optimal single-term updates, and the convex relaxation techniques, which take advantage of the fact that under certain conditions finding the non-convex  $\ell_0$ -norm is equivalent to solving the  $\ell_1$ -norm or even in some cases the  $\ell_2$ -norm problem. Referring to Figure 2.1, it becomes clear that the  $\ell_1$ -norm is the closest convex approximant of the sparse  $\ell_0$ -norm.

### 2.5.1 Greedy Algorithms

The greedy algorithms abandon exhaustive search and instead perform a series of locally optimum single-term updates with the hope of finding a globally optimum solution. Starting from  $\mathbf{x}^0 = 0$ , the greedy approach iteratively constructs a  $k$ -term approximant  $\mathbf{x}^k$  by maintaining a set of active columns and at each iteration expanding that set by one column. The column selected at each stage minimizes the residual  $\ell_2$  error in approximating  $\mathbf{b}$  from the currently active set of columns. This iterative approach is continued until the residual  $\ell_2$  error falls below a specified threshold, at which point the algorithm terminates. In many cases, such a greedy approach will not recover the optimum solution, e.g. problems may arise in greedy algorithms if a non-ideal basis vector is selected in the initial stages of the process. However, under certain conditions on the overcomplete basis [44], the optimum sparse solution can be found.

In this research, a specific greedy algorithm called orthogonal matching pursuit (OMP) [41, 44] was investigated for localization of underwater targets. Under certain conditions on the structure of the dictionary matrix and the minimum magnitude of the non-zero components of the signal, OMP can exactly recover the support of the signal with high probability. Conditions for exact recovery and the effects of noise are discussed in [44]. The OMP algorithm used in this work is outlined below.

## Orthogonal Matching Pursuit

**Goal:** Approximate the solution of:  $\min_{\mathbf{x}} \|\mathbf{x}\|_0$  subject to  $\mathbf{Ax} = \mathbf{b}$ .

**Parameters:** matrix  $\mathbf{A}$ , vector  $\mathbf{b}$ , error threshold  $\epsilon_0$ .

**Initialization:** Initialize  $k = 0$  and set

- Initial solution  $\mathbf{x}^0 = 0$ .
- Initial residual  $\mathbf{r}^0 = \mathbf{b} - \mathbf{Ax}^0 = \mathbf{b}$ .
- Initial solution support  $\mathcal{S}^0 = \text{Support}\{\mathbf{x}^0\} = \emptyset$ .

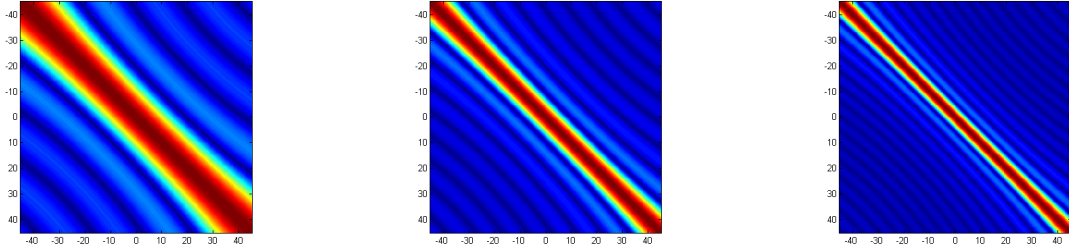
**Iterations:** Increment  $k$  by 1 and perform the following steps:

- **Sweep:** Compute errors  $\epsilon(j) = \min_{z_j} \|\mathbf{a}_j z_j - \mathbf{r}^{k-1}\|_2^2$  for all  $j$  using the optimal choice  $z_j^* = \mathbf{a}_j^T \mathbf{r}^{k-1} / \|\mathbf{a}_j\|_2^2$ .
- **Update Support:** Find a minimizer  $j_0$  of  $\epsilon(j)$ :  $\forall j \notin \mathcal{S}^{k-1}, \epsilon(j_0) \leq \epsilon(j)$ , and update  $\mathcal{S}^k = \mathcal{S}^{k-1} \cup \{j_0\}$ .
- **Update Provisional Solution:** Compute  $\mathbf{x}^k$ , the minimizer of  $\|\mathbf{Ax} - \mathbf{b}\|_2^2$  subject to  $\text{Support}\{\mathbf{x}\} = \mathcal{S}^k$ .
- **Update Residual:** Compute  $\mathbf{r}^k = \mathbf{b} - \mathbf{Ax}^k$ .
- **Stopping Criteria:** If  $\|\mathbf{r}^k\|_2 < \epsilon_0$ , stop. Otherwise, apply another iteration.

**Output:** The proposed solution is  $\mathbf{x}^k$  obtained after  $k$  iterations.

### 2.5.2 Convex Relaxation Techniques

A second way to render the  $\ell_0$ -norm problem more tractable is to replace the highly discontinuous  $\ell_0$ -norm with a friendlier continuous approximation. One such regularization scheme is to replace the  $\ell_0$ -norm with an  $\ell_p$ -norm for some  $p \in (0, 1]$ . The FOCUSS algorithm [24], for example, replaces the  $\ell_0$ -norm with the  $\ell_p$ -norm for some fixed  $p \in (0, 1]$  and seeks a solution using iteratively reweighted least-squares [24]. Another strategy is to replace the  $\ell_0$ -norm with its best convex approximation, the  $\ell_1$ -norm [43]. The problem may then be



(a)  $|\mathbf{A}^H \mathbf{A}|$  for  $M = 6$  sensors.      (b)  $|\mathbf{A}^H \mathbf{A}|$  for  $M = 12$  sensors.      (c)  $|\mathbf{A}^H \mathbf{A}|$  for  $M = 20$  sensors.

**Figure 2.2:** Mutual coherence for dictionaries formed using sensor arrays of varying length. For all cases, angle range of  $\theta = -\pi/4 - \pi/4$  and angle grid resolution of  $\pi/720$  are used.

cast as a linear programming problem and solved using a number of standard optimization methods [37, 47], such as interior-point or simplex methods.

Results from [25] show that under certain conditions the  $\ell_0$ -norm solution may be accurately estimated by solving the  $\ell_2$ -norm problem. Minimizing the  $\ell_2$ -norm favors solutions with many non-zero entries, which is contrary to the goal of sparse representation. However, if the dictionary,  $\mathbf{A}$ , is structured such that its columns are separated by some minimum distance, the  $\ell_2$ -norm solution will closely approximate the sparse solution,  $\ell_0$ . In other words, the basis vectors used to construct  $\mathbf{A}$  must be adequately dissimilar in order for this approximation to succeed. In the sparse representation literature, mutual coherence, which is defined as the maximum absolute value of the cross-correlations between the columns of  $\mathbf{A}$ , is used as this distance measure.

In the sparse representation-based source localization approach, an  $M \times N$  dictionary matrix,  $\mathbf{A}$ , is constructed with columns formed from steering vectors corresponding to signals received from  $N$  angle grids by  $M$  sensors in an array, i.e.  $\mathbf{A} = [\mathbf{a}(\theta_1), \dots, \mathbf{a}(\theta_N)]$ . Considering the definition of dictionary mutual coherence, it is clear that the ability to achieve source localization with such a dictionary is directly related to the physical array geometry, i.e. length,  $M$ , and the angle grid resolution used, i.e.  $N$ . In Figure 2.2, the mutual coherence measure (computed as  $|\mathbf{A}^H \mathbf{A}|$ ) is shown for several angle of arrival dictionaries to demonstrate the relationship between angle dictionary structure and sparse solution finding. For

this exercise, narrowband sources are considered with frequency  $f_0 = 15kHz$ . The speed of sound in water was  $c_0 = 1500m/s$  giving a wavelength,  $\lambda = c_0/f_0 = 0.1m$ . The inter-element spacing for the simulated sensor array was set as  $\lambda/4$  to prevent spacial aliasing. The angle range considered is  $-\pi/4$  to  $\pi/4$  and an angular resolution of  $\pi/720$  was used, resulting in a dictionary of size  $M \times 360$ . Figures 2.2(a), 2.2(b) and 2.2(c) are the dictionary mutual coherence, i.e.  $|\mathbf{A}^H \mathbf{A}|$ , for dictionaries formed using arrays of length  $M = 6$ ,  $M = 12$  and  $M = 20$ , respectively. Note that as the number of sensors in the array is increased, the mutual coherence tends towards the identity matrix, i.e.  $|\mathbf{A}^H \mathbf{A}| = \mathbf{I}$ . This is an intuitive result, since the dictionary which ideally maximizes the distance between its columns is one constructed from strictly orthogonal basis vectors.

For the sonar data sets under consideration, it is reasonable to assemble sensor arrays using the available pings and channels that lead to dictionaries that are adequately orthogonal to allow for target localization via the  $\ell_2$ -norm solution. In this work, a simple least-squares approximation of the  $\ell_2$ -norm is used, i.e.

$$\mathbf{x} = \mathbf{A}^+ \mathbf{b} \tag{2.8}$$

where  $^+$  denotes the Moore-Penrose pseudoinverse, which for a full column rank matrix,  $\mathbf{A}$ , is  $\mathbf{A}^+ = (\mathbf{A}^* \mathbf{A})^{-1} \mathbf{A}^*$  with  $^*$  denoting the Hermitian transpose. This least-squares approach was used in [25], where an  $\ell_2$ -norm approximation was proposed for super-resolution imaging for localization of far-field point sources in synthetic aperture radar (SAR) data. The problem formulation and resultant dictionary structure in [25] motivated the use of the least-squares approximation for underwater targets in sonar data. The viability of this convex relaxation approach was verified through simulations (see Section 4.3.4), which also helped to illuminate the relationship between array geometry and target localization capability.

## 2.6 Conclusions

Sparse representation involves searching for the most compact representation of a signal in terms of a linear combination of columns (bases) from a predefined dictionary. Underwater target localization naturally motivates such an approach if it is assumed that targets present in the search region on the seafloor are sparsely distributed. That is, if a search grid is defined over the area of interest, very few of the grid points will contain targets, and the goal becomes to identify those grid points. The sparsity condition imposed on this problem allows for the use of tools from the sparse representation framework.

Two general classes of sparse solution recovery methods were presented in this chapter. The first class of methods, commonly referred to as greedy algorithms, attempt to recover the globally optimal sparse solution by performing a series of locally optimal updates. One particular greedy algorithm, orthogonal matching pursuit, was used in this work for target localization. The second class of methods take the approach that under certain conditions on the structure of the overcomplete basis, the non-convex  $\ell_0$ -norm may be approximated by a convex function such as the  $\ell_1$ - or  $\ell_2$ -norm. It was illustrated in Section 2.5 that the particular problem of target localization may be tackled by finding the  $\ell_2$ -norm solution if the angle of arrival dictionary exhibits adequate distance between its columns, i.e. its mutual coherence. This mutual coherence measure is directly related to the physical array geometry and the angular resolution used to construct the overcomplete dictionary. Using the sonar data under consideration, it is possible to assemble subarrays from available pings and channels to achieve dictionary construction that allows for approximating the sparse solution with an  $\ell_2$ -norm solution (see Chapter 3 for a complete description of the sonar data sets). In this work, the simple least-squares approximation of the  $\ell_2$ -norm problem is utilized to estimate source angle of arrival, which is in keeping with the SAR imaging application of [25].

## CHAPTER 3

### SONAR SYSTEMS AND DATA PROPERTIES

#### 3.1 Introduction

This section discusses the sonar systems and their characteristics together with a description of the data collection processes that resulted in data sets used for the experiments in this study. This is important because understanding the sonar system and how it collects data is instrumental in developing robust and discriminatory underwater object detection and localization systems. The physical characteristics of the target fields used to collect the data sets, as well as the characteristics and properties of objects contained in each data set, are also highlighted. Analyzing the properties of the objects within each data set is an important issue, since understanding the similarities and differences that exist between the target and non-target classes can provide clues on how to devise effective detection and localization frameworks.

The outline of this section is as follows. Section 3.2 describes the rail-mounted hydrophone system used to collect the Pond Experiment 2010 (PondEx10) data set, and then provides details of the specific data sequences used in this study. Section 3.3 discusses the operating characteristics of the current generation wing BOSS system [55] and the improvements made to its design in relation to past BOSS systems. A discussion on the types of objects contained in the BOSS data set, the experimental settings, physical characteristics of the target field, and data collection issues are also discussed in this section. Section 3.4 discusses the data preprocessing steps that are necessary to prepare the data for application of the procedures that are discussed in this thesis. Finally, conclusions are made in Section 3.5.

#### 3.2 Pond Setup and Data Set

PondEx10 consists of a series of monostatic and bistatic acoustic scattering measurements that were conducted to investigate imaging and localization algorithm capabilities based on acoustic response for underwater unexploded ordnances (UXOs). These measurements were

carried out in March 2010 in a fresh water man-made pond facility at the Naval Surface Water Center - Panama City Division (NSWC PCD). In the next subsections, first the physical properties of the pond facility and data acquisition systems used for PondEx10 are described in detail. Then, the properties of the specific PondEx10 data sequences used in this work are described, including the object characteristics, target field layout, and data collection system experimental settings. In addition to the data specifications received from NSWC, descriptions from [48] - [51] provided supplementary information about the PondEx10 data set.

### **3.2.1 Pond Facility and Data Collection System**

The NSWC Pond setup contains two sonar systems in a man-made fresh water facility. An aerial photograph of this pond facility is provided in Figure 3.1. This roughly 9-million gallon pond has approximate dimensions of 110 m by 80 m. An approximately 1.5 m thick layer of sand covers the bottom of the pond, and the water depth over the region of target deployment is roughly 14 m. To achieve precise positioning of the objects deployed in the target field, a 21 m rail system was installed in the pond at a height of 4 m from the water-sand interface. Two anchor bolts were placed at a ground range of 11 m from the rail, and a guideline was stretched between the two anchors parallel to the rail. This guideline was marked at 4, 7, 10, 13, and 16 meters from the left (South) bolt anchor. These five positions are designated target patch #1 through #5 and indicate the centers of 1 m<sup>2</sup> regions where targets are deployed. Figure 3.2 depicts the positioning of these target patches with respect to the fixed rail.

The pond facility is equipped with two sonar systems for data collection from objects. The first sonar system consists of a six-element hydrophone array and an acoustic source mounted to a mobile tower attached to the fixed rail system on the bottom of the pond. The six hydrophones are arranged in a vertical linear array at an approximate height of 4 m from the water-sediment interface. Figure 3.3 illustrates this target field layout and hydrophone array geometry. The inter-element spacing of the six sensors is also depicted.



**Figure 3.1:** Aerial view of the NSW PCD pond facility.

Note that the four inner sensors are equi-spaced (0.1 m), while the two outermost sensors are positioned at 0.2 m from their adjacent sensors. These six receiver channels are designated as Channel 7 through Channel 12, with Channel 7 being the topmost hydrophone element. Each channel in the receiver on this mobile tower system records separately at a sampling rate of 1 MHz. When traveling from South to North, the acoustic source transmits a 6 ms linear FM chirp centered at 16 kHz with 30 kHz bandwidth. On the return trip, the source transmits a 4 ms linear FM chirp centered at 40 kHz with 20 kHz bandwidth. The second sonar system consists of a series of stationary hydrophone receivers mounted on horizontal pan and vertical tilt motors, which allows the main lobe of the receivers to be aligned with the desired target patches during data collection. These stationary receivers record data at a sampling rate of 500 kHz. The two sonar receiver systems are indicated in Figure 3.2 as “mobile tower” and “stationary tower”, respectively.

### **3.2.2 PondEx10 Data Set and Properties**

During the PondEx10 measurements, either a total of five or a total of seven objects were deployed in the target field. All twelve target objects and their descriptions are listed

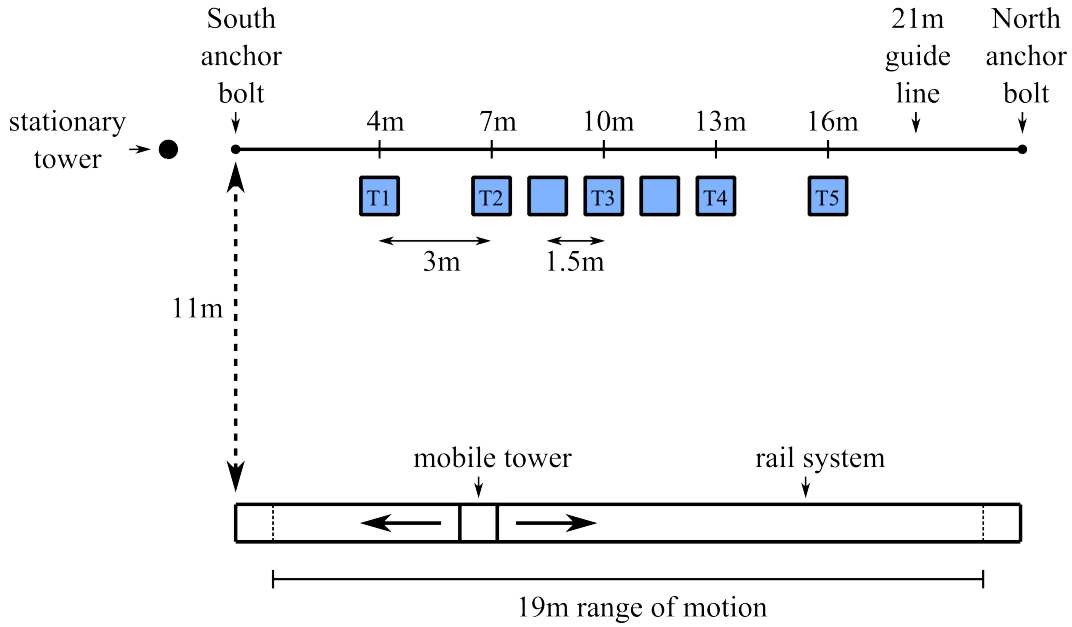


**Figure 3.2:** Layout of the PondEx10 target field (top view).

in Table 3.1. In the case where five targets were used, the five objects were placed in target patches #1 through #5 giving a separation of 3 m between adjacent targets. In the case where seven targets were deployed, five targets were placed in target patches #1 through #5, and two targets were placed in the regions between target patches #2 and #3, and target patches #3 and #4, respectively, leading to inter-target separations of either 3 m or 1.5 m. These target positions are shown in blue on Figure 3.2. For each 1 m<sup>2</sup> target patch, the sides of the square region perpendicular to the direction of the rail were bordered with two carefully leveled aluminum rails. Prior to a set of measurements, the target patches were smoothed by scraping a third aluminum bar along these two rails to level the sediment in the target region; in the event that low spots were observed, they were filled with sand from outside the target field.

For the work presented in this thesis, a specific subset of the PondEx10 data was used. During acquisition of these particular sequences, five target objects were deployed in a proud configuration at a grazing angle of approximately 20° with respect to the fixed rail system.

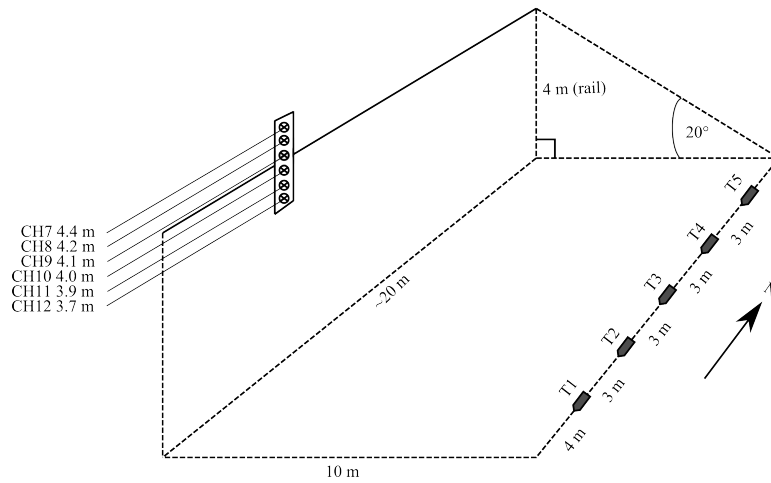


**Figure 3.3:** Six-element hydrophone array that is part of the first sonar system in the pond facility.

These five specific targets are listed in Table 3.2 and are pictured in Figure 3.4. Targets T2 - T5 are projectiles, and T1 is a wedged cylinder (the wedged end is designated as the “nose” of this target).

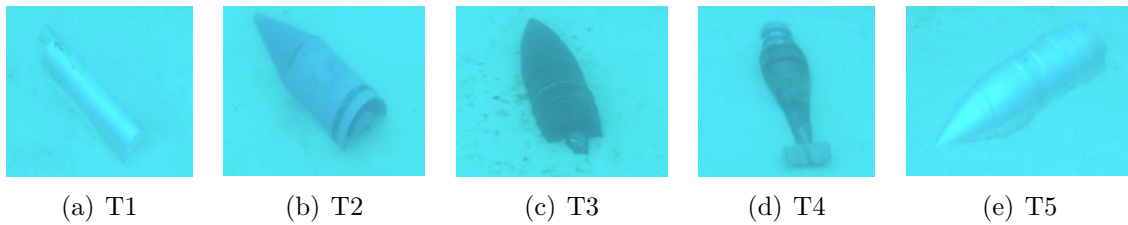


**Figure 3.4:** Objects in PondEx10 target field.

Collection of the PondEx10 sequences under consideration was performed using the “mobile tower” system. Data was acquired during South-to-North passes of the mobile hydrophone array, and hence, the transmit signal used was the 6 ms linear FM chirp centered at 16 kHz with 30 kHz bandwidth. This tower system was moved at a rate of 0.05 m/s with the source transmitting every 0.5 s. The total distance traveled along the rail is 19 m. Ten data sequences were collected, each containing raw data from all six channels in the receiver array. During collection of each of these sequences, the mobile tower traversed the full range of motion along the rail (19 m) and data was collected at 0.025 m increments. The primary

**Table 3.1:** List of targets used in Pond Experiment 2010 measurements.

Label	Description
1	Solid Aluminum Cylinder (2 ft long, 1 ft OD)
2	Aluminum Pipe (2 ft Long, 1ft ID, 3/8 in Wall Thickness)
3	Inert 81 mm Mortar Filled with Cement
4	Solid Steel Artillery Shell
5	Machined Aluminum UXO #1
6	Machined Aluminum UXO #2
7	Machined Steel UXO
8	De-Militarized 152 mm TP-T Round
9	De-militarized 155 mm Empty Projectile (No Fuse or Lifting Eye)
10	Small Notched Aluminum Cylinder
11	Rock #1
12	Rock #2

**Table 3.2:** Targets deployed during PondEx10 proud configuration measurements.

Label	Description
T1	Small Notched Aluminum Cylinder
T2	De-Militarized 152 mm TP-T Round
T3	Machined Steel UXO
T4	Inert 81 mm Mortar Filled with Cement
T5	Machined Aluminum UXO #1

variability between data sequences was the angular orientation of the target objects with respect to the rail. In order to achieve the desired target rotation during each sequence, a square PVC frame with dimensions slightly larger than the target patches was constructed. A series of marking holes in the PVC frame allowed for selection of an angle ranging from  $-80^\circ$  to  $80^\circ$  in  $20^\circ$  increments. For the UXO target objects,  $0^\circ$  was defined as broadside to the rail with the “nose” pointed towards the stationary tower (refer to Figure 3.2). The target orientations and other details for each of the ten sequences are provided in Table 3.3. Figure 3.5 depicts the direction of the nose of the targets with respect to the rail for each of the ten data sequences.

In summary, there are several properties of the PondEx10 data set that provide excellent opportunities to benchmark various object localization and seafloor imaging algorithms against each other. Some of the key properties are as follows.

**Table 3.3:** Description of the PondEx10 data sequences.

Seq	Target Orientation
185	targets parallel to rail, noses pointed South: $0^\circ$ (newly smoothed field)
187	targets $10^\circ$ off nose end towards rail, designated $-80^\circ$
189	targets $30^\circ$ off nose end towards rail, designated $-60^\circ$
191	targets $40^\circ$ off broadside to rail, nose slightly towards rail, designated $-40^\circ$
193	targets $20^\circ$ off broadside to rail, nose slightly towards rail, designated $-20^\circ$
195	targets parallel to rail, noses pointed South: $0^\circ$
197	targets $20^\circ$ off broadside to rail, nose slightly away from rail, designated $20^\circ$
199	targets $40^\circ$ off broadside to rail, nose slightly away from rail, designated $40^\circ$
201	targets $30^\circ$ off blunt end towards rail, designated $60^\circ$
203	targets $10^\circ$ off blunt end towards rail, designated $80^\circ$

- The transmitter and receiver used to collect the data for this study are mounted on a fixed rail system, which mitigates the effects of platform motion and other positioning uncertainties that are common for most sonar data sets, e.g., those collected by UUVs.
- Since the target field contains minimal clutter (i.e. unknown objects not listed in Table 3.1) and known objects are positioned in precise locations, there exists a well-defined “ground-truth”, which can be used to benchmark performance of localization and SAS processing algorithms.
- Object orientation represents the only variability between different data sequences, thus providing the opportunity to test the robustness of each method to this variation, and examine its impact on how objects are imaged.

### 3.3 BOSS System and Data Set

#### 3.3.1 Buried Object Scanning Sonar

The BOSS system was originally created with the goal of generating composite images and target strength measurements for buried underwater target detection in real-time [53]. BOSS processing involves a sequence of operations that include chirp sonar processing, 3-D near field focusing using data from a real or synthetic receiving aperture to generate a 3-D map of acoustic intensity for each transmission event, transmission beam steering that allows target illumination at a broad range of aspect angles, real-time 3-D image reconstruction of

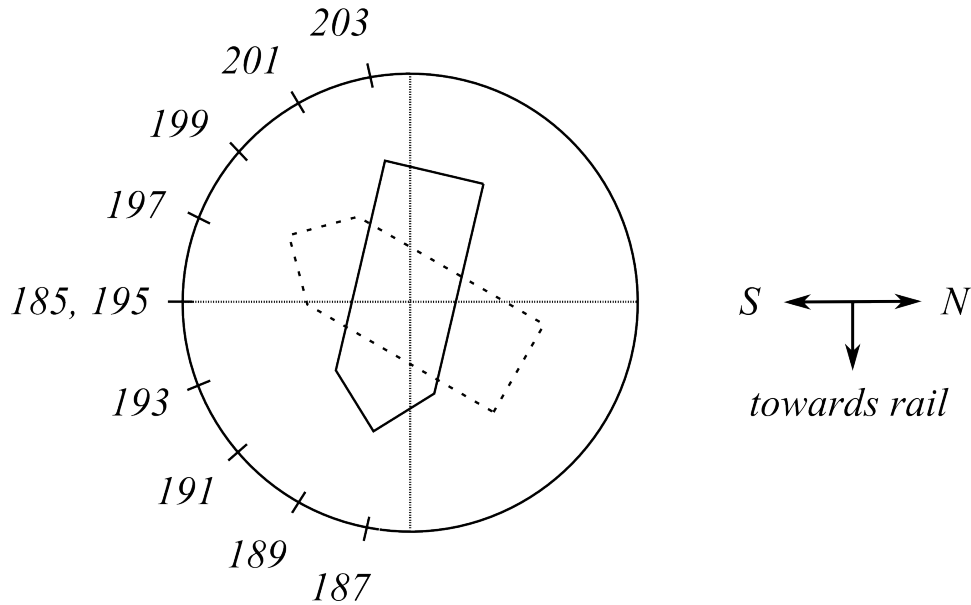


**Figure 3.5:** Target orientations for each PondEx10 data sequence.

buried objects showing their burial depth, shape, orientation, and location, and real-time buried object detection [54].

The wing BOSS [55] is designed to scan for buried or proud underwater objects using a spherical acoustic source mounted in the same horizontal plane as the receiver array. This omnidirectional source generates a 5 millisecond linear FM (LFM) signal over the band of 3-19 kHz. The time series of the LFM transmit signal and its magnitude spectrum are shown in Figures 3.6(a) and (b), respectively. Ideally, the magnitude spectrum shown in Figure 3.6(b) would have the same gain at all frequencies. However, the implementation of the circuitry that generates this transmit signal produces imperfections at the beginning and end of each transmission due to its transient response. Since the transmit signal is LFM, the low and high frequency components are found at the beginning and end of the signal, respectively, and therefore only the portions of the magnitude spectrum corresponding to these frequencies are affected.

The wing BOSS contains two 1 m hydrophone arrays mounted on the wings of the Bluefin 12 [57] unmanned underwater vehicle (UUV) as shown in Figure 3.7. Each wing contains

20 hydrophone channels, yielding a 40-channel strip array used to collect the sonar returns. The wing BOSS is smaller and more mobile than the older generation disk BOSS, as the wing arrays tend to produce less drag than the large circular array [55]. The larger array size and increased drag of the disk BOSS means it had to be towed instead of deployed on a UUV when collecting data. In order to improve the resolution of target imagery, the wing BOSS utilizes time-delay focusing extended to hydrophone data collected over several transmissions. With synthetic aperture sonar (SAS) processing, the along-track resolution of target imagery improves with distance traveled while forming the synthetic aperture [55]. The use of SAS processing also allows the along-track length of the array to be significantly reduced, thereby reducing the hydrophone array drag and surface area and increasing the ease in which BOSS can be deployed on UUV's [55].

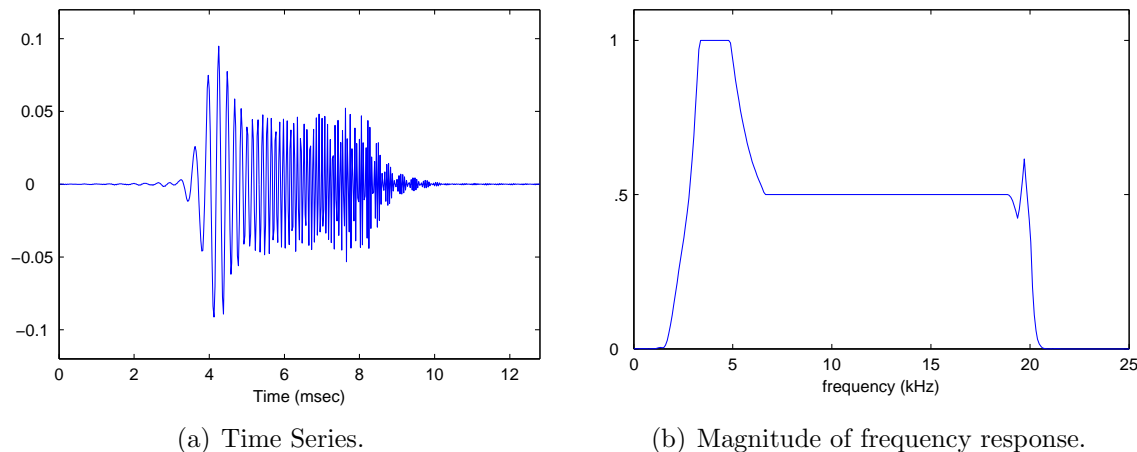


**Figure 3.6:** LFM transmit signal and its frequency response.

Images of the seafloor generated with BOSS SAS processing can be used to detect and localize potential targets, though classification of these objects is generally not reliable using time-delay focusing. While lower resolution images can be generated in real-time and used for detection, generating high resolution images is very computationally intensive, and is currently not feasible in real-time. This is due to the fact that sonar data from several pings collected by each hydrophone element must be coherently integrated by applying the appropriate time-delays, which is a consequence of using a synthetic aperture and a single line



**Figure 3.7:** Bluefin 12 UUV with wing BOSS payload (courtesy of the FAU Department of Ocean Engineering).

array of hydrophones. However, it has been shown [52] that a single line array of hydrophones provides near optimal performance when sediments behave as randomly distributed fixed point scatterers. That is, additional lines of hydrophone arrays did not significantly improve the SNR of a target echo in the presence of stationary volume scattering. However, in practice, performance improvement is observed as the number of hydrophone line arrays is increased. This is due to the single-ping processing gain of a physical aperture over non-stationary scatterers such as water column biogenic scatterers and sea surface reverberation.

### 3.3.2 Davis Point Data Set and Properties

The Davis Point data set was collected in St. Andrews Bay, Panama City, FL in March, 2007 using the wing BOSS system. The Davis Point target field contains fourteen different objects, including a mixture of target and non-target objects. The bottom type of the target field is smooth and sandy. A number of naturally occurring objects (such as rocks) are also present in the target field. Fig. 3.8 shows the relative position of each object in the target field, while Table 3.4 gives the list of the objects, their properties, and burial conditions whether proud or buried. The position of each object is based on the ground truth coordinates as determined during a Naval Surface Warfare Center (NSWC) diver survey exercise.

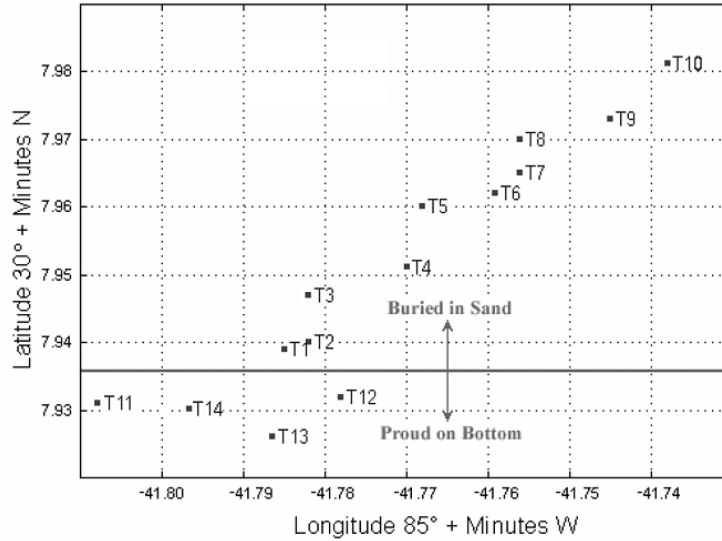


**Figure 3.8:** Layout of the Davis Point target field.

**Table 3.4:** Description for each object in the BOSS data set. OD = outside diameter.

Label	Description	Status
T1	1.83 m Bomb-Shaped Marker (0.46 m OD)	Buried
T2	0.51 m Artillery Shell	Buried
T3	1.68 m Bomb-Shaped Target (0.28 m OD)	Buried
T4	1.83 m Iron Cylinder (0.46 m OD)	Buried
T5	1.52 m Iron Cylinder (0.18 m OD)	Buried
T6	0.36 m Stainless Steel Sphere	Buried
T7	0.89 m Artillery Shell	Buried
T8	0.36 m Stainless Steel Sphere	Buried
T9	0.61 m Iron Cylinder (0.15 m OD)	Buried
T10	1.83 m Bomb-Shaped Marker (0.46 m OD)	Buried
T11	2.44 m Concrete Pipe (0.46 m OD)	Proud
T12	1.83 m Concrete Pipe (0.46 m OD)	Proud
T13	1.83 m Concrete Pipe (0.46 m OD)	Proud
T14	1.83 m Concrete Pipe (0.46 m OD)	Proud

When collecting sonar ping data from the objects in the Davis Point target field, the Bluefin 12 UUV with wing BOSS payload traveled at an altitude that was generally between 2.25 m and 3.00 m. The speed of the UUV was approximately 1.2-1.5 m/s (2.33-2.92 knots) with a ping repetition rate of 25 pings/s. The sonar data collected by the wing BOSS was sampled at 43,043 Hz. The vehicle speed and ping rate used in the collection of the

Davis Point data set corresponds to a physical separation between two consecutive pings of approximately 4.8 cm to 6 cm.

Sonar pings were collected over a variety of different runs through the target field. In particular, the Bluefin 12 UUV initially made five groups of 15-18 runs, where each group centered around either object T1, T3, T4, T5, or T10. These objects were chosen as the centers of groups mostly because their locations in the target field allow a single run over them to capture sonar returns from a large number of other surrounding objects. The runs in each group form a “star-shaped” path around the object the group was centered over. For the remainder of this thesis, the different runs that form star-shaped patterns will be referred to by the object the run was centered over as well as a letter corresponding to the run number (e.g. line T1b refers to the second run centered on object T1). Included in the 15-18 runs over each object were runs that were made in north-south, east-west, and northwest-southeast trajectories at varying distances from the center object. This method of data collection allowed pings from different runs to capture signatures from each object from a variety of aspects and with different depression angles measured between the sonar and an object in the across track vertical plane. This allows for the evaluation of the SAS processing methods’ sensitivity to variations in these depression angles.

In addition to the runs centered on specific objects, the Bluefin 12 UUV made 18 diagonal runs in a northeast-southwest trajectory over the entire target field, capturing one to four objects per run. These longer runs will simply be referred to by the run number (e.g. line 2 refers to the second long diagonal run). The long diagonal runs not only obtained more data on all the objects covered by the star-shaped groups, except T12 and T13, but were also able to capture sonar returns from objects not covered by the star-shaped groups, namely those of T11, T14, T7, and T8. Note that the data collection for each run actually begins and ends far away from objects that the run goes over. Therefore, only a portion of the pings collected for each run actually correspond to areas containing one or more of the objects listed in Table 3.4. The actual number of useful pings that capture objects of interest is

approximately 500-800 pings for runs in the star-shaped groups and 500-1200 pings for long diagonal runs.

In summary, there are several properties of the Davis Point data set that provide challenges for target localization and detection and generation of SAS-like images. Many of these properties also make it very useful for benchmarking various methods. These issues, in order of importance, are as follows.

- Widely different shapes, sizes, and/or compositions of objects of interest, causing a potentially large variety in appearances in SAS images for different types of objects.
- Diverse variations in the number of available aspects and depression angles for different objects, which may result in imbalance in accurate representation of the properties of these objects.
- Buried (at different depths) and proud (flush) objects on the bottom have sonar returns off them that could be widely different.
- The slight variations of altitude (2.25-3.00 m) and speed (1.2-1.5 m/s) of the Bluefin 12 UUV during data collection, which could potentially lead to further variations in the sonar returns that capture the objects.

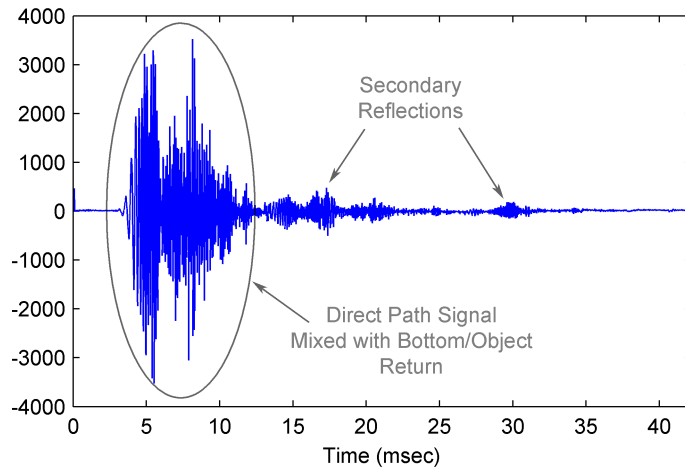
Clearly, these challenges indicate that good imaging performance on the Davis Point data set would require development of robust methods that account for these variations in the environmental and operating conditions that are realistic in any mine-hunting scenario.

### **3.4 Data Preprocessing**

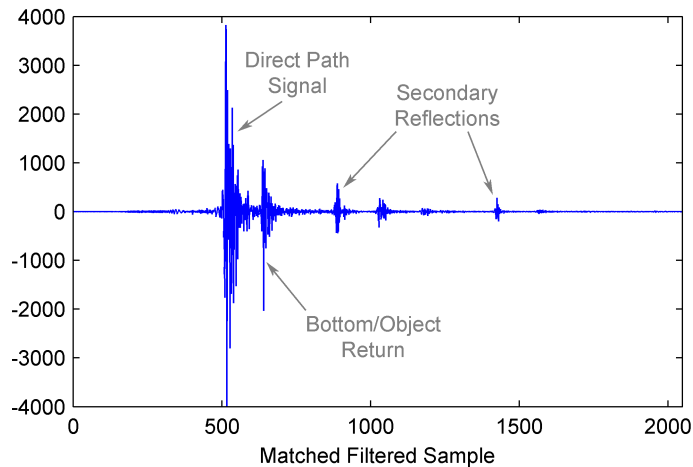
In Chapter 4, a new sparse representation framework for precise object localization is presented. Before this method can be implemented, however, certain steps must be taken to remove portions of the signal that would be detrimental to the processes. These preprocessing steps are discussed in detail below using sonar returns from the Davis Point data set as an example.

Raw sonar returns from buried or bottom objects are typically composed of the desired portion of the signal from the actual objects along with undesirable portions of the signal, which include the direct path return, the bottom return, bottom reverberation, and returns off the hydrophone baffle. These unwanted portions of the signal can be thought of as a correlated interference, and may cause the features to change dramatically. For the data used in this study, the difficulty lies in the fact that objects are buried at varying depths and may even be proud on the bottom at times. Thus, removing the bottom effects from the return off the object in an automatic fashion is a very challenging task. Figure 3.9(a) shows the time series for a typical sonar return in the Davis Point data set. As can be seen, delineation of the direct path signal, bottom return, object return, and various echoes is quite difficult in the time domain. Figure 3.10(a) shows a color image plot of raw sonar returns (for all pings) recorded by Channel 1 of the wing BOSS array for line T4e of the Davis Point data set. The left-most column in this image corresponds to the time series of the first ping in this run. As can be seen, the separation of the bottom effects, reverberation, and other sources of noise and interference is not an easy task when given the original sonar returns.

In order to overcome this problem, the inverse filtering algorithm [16] that relies on windowing in the matched filter domain is adopted. Inverse filtering is applied to the windowed signal in order to recover the “clean signal”, which is ideally free of interference effects. This method exploits the fact that the direct path signal, reverberation, and hydrophone baffle return are more separated from the bottom and main object returns in the matched filter domain than in the original signal domain. Figure 3.9(b) demonstrates this fact by showing the matched filtered version of the signal shown in Figure 3.9(a). In the matched filtered signal, the first prominent peak corresponds to the direct path signal from the projector to the hydrophone, which has the highest magnitude. The next peak shows the bottom return, and the object return immediately follows the bottom return. The other peaks correspond to bottom reverberation. As can be seen by comparing the original sonar ping with that



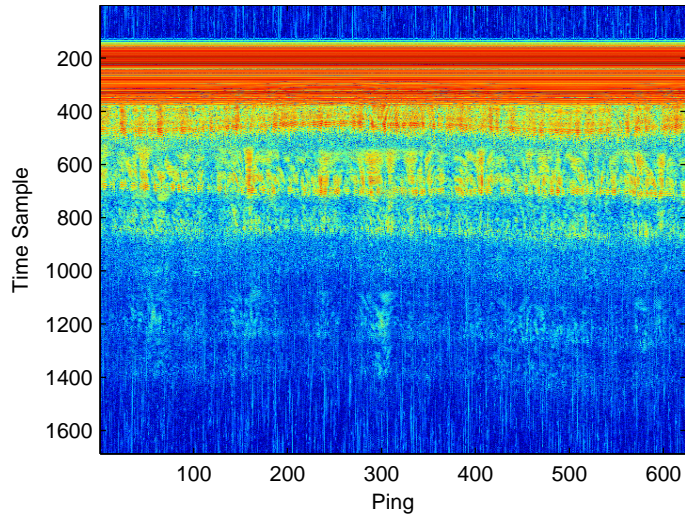
(a) Raw sonar return for ping 300 of line T4e of the Davis Point data set.



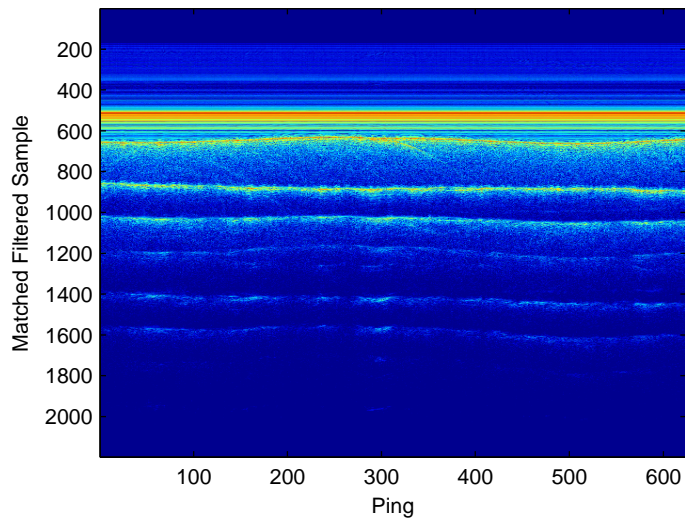
(b) Matched filtered sonar return for ping 300 of line T4e of the Davis Point data set.

**Figure 3.9:** Raw and matched filtered versions of a typical sonar return from the Davis Point data set.

of the matched filtered ping, the matched filtering has resulted in better separation of the sonar returns. Figure 3.10(b) shows the matched filtered image obtained from line T4e of the Davis Point data set using Channel 1 of the wing BOSS array. As can be seen from Figures 3.10(a) and (b), the returns representing different portions of the signal are indeed more separable in the matched filtered domain than in the raw image. A graphical representation of the steps used in this preprocessing is shown in Figure 3.11, and the details of this process are provided below.



(a) All raw sonar returns.



(b) All matched filtered sonar returns.

**Figure 3.10:** Images of all raw and matched filtered sonar returns for line T4e of the Davis Point data set.

Consider a raw sonar return, denoted by  $x_p[n]$ , captured by a single hydrophone element at ping  $p$ . An example of such a signal was discussed above and can be seen in Figure 3.9(a). This raw sonar return can be expressed as

$$x_p[n] = h_p[n] * s[n] + f_p[n] * s[n] + v_p[n] \quad (3.1)$$

where  $s[n]$  is the transmit signal, the first term on the right-hand side represents the return

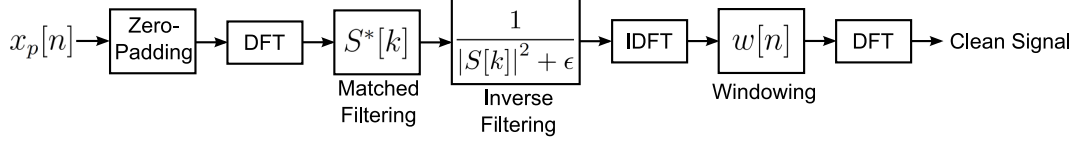


**Figure 3.11:** Block diagram of the preprocessing steps used for sparse representation-based target detection and localization.

signal off the target with impulse response  $h_p[n]$ , the second term is the collective effect of all correlated clutter with impulse response  $f_p[n]$ , and  $v_p[n]$  represents uncorrelated ambient noise. The correlated noise represents such effects as the direct path return, returns off the hydrophone baffle, secondary reflections, reverberation, etc. Note that this model assumes time invariance of  $h_p[n]$  and  $f_p[n]$  between consecutive pings. As mentioned, the goal of this preprocessing is to extract the portion of the signal corresponding to the bottom and object. The steps needed to accomplish this are as follows. In contrast to the block digram shown in Figure 3.11, all the steps below are shown in the frequency domain.

1. *Matched Filtering:* The recorded signal,  $x_p[n]$ , is first matched filtered in order to better separate the bottom and target returns from those of the correlated clutter. The effects of the matched filter are shown in Figure 3.9(b). In the frequency domain, this process yields

$$X_p[k]S^*[k] = H_p[k]|S[k]|^2 + F_p[k]|S[k]|^2 + V_p[k]S^*[k] \quad (3.2)$$

where “\*” denotes the complex conjugate operation,  $X_p[k]$  is the discrete Fourier transform (DFT) of  $x_p[n]$  (zero-padded), and the other terms are similarly defined. Zero-padding is necessary to ensure the product  $X_p[k]S^*[k]$  produces the frequency domain equivalent of the linear convolution  $x_p[n] * s[-n]$ .

2. *Windowing:* To remove the correlated noise effects, windowing is applied to the matched filtered signal in the time or frequency domains. The window in the time domain,  $w[n]$ , is chosen such that the windowed signal contains the main bottom

return (unavoidable) and main object return. This is done by placing the leading edge of the window at a fixed sample number chosen to coincide with the onset of the bottom return. The size of the window is determined based upon the extent of the autocorrelation function of the transmit signal, which is large enough to capture all of  $h_p[n]$ . The direct path return is removed since it precedes the bottom return and the secondary reflections are also removed since they are typically separated from the object return enough to be outside the window (see Figure 3.9(b)). This process yields

$$(X_p[k]S^*[k]) * W[k] \approx H_p[k] |S[k]|^2 + (V_p[k]S^*[k]) * W[k]. \quad (3.3)$$

Note that it is assumed that the window captures the entire object and bottom response without any modification, and removes the effects of the correlated noise.

3. *Inverse Filtering:* The signal is then inverse filtered, thus producing

$$\hat{X}_p[k] = (X_p[k]S^*[k]) * W[k] \frac{S[k]}{|S[k]|^2 + \epsilon} \approx H_p[k]S[k] \quad (3.4)$$

where  $\epsilon$  is a small quantity used to avoid singularity problems. In (3.4), the effect of uncorrelated noise after inverse filtering is ignored as it does not impact the results because its ping-to-ping coherence is negligible. The recovered clean signal in the time domain can be found via

$$\hat{x}_p(n) = \text{Real}\{\mathcal{IDFT}[\hat{X}_p[k]]\} \quad (3.5)$$

where  $\mathcal{IDFT}$  stands for the inverse DFT. Unfortunately, this simple inverse filtering approach may cause some unwanted ringing artifacts in the recovered signal, and hence it may be desirable to utilize a more elaborate signal separation approach to solve this problem. However, owing to the simplicity of the inverse filtering process, this method is used here.

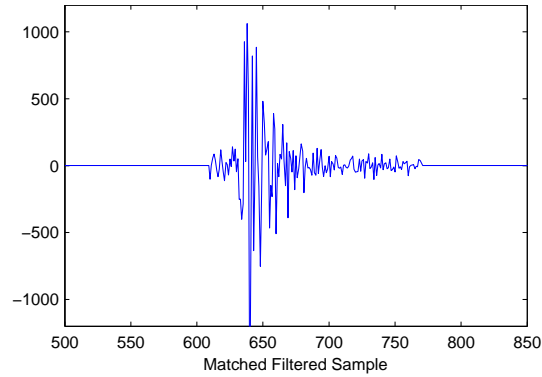


**Figure 3.12:** Windowed matched filtered signal for ping 300 of line T4e of the Davis Point data set.

Note that, for buried objects, the bottom return is first observed, followed by the return from the object itself. However, if an object is not fully buried, the corresponding returns from the bottom and the objects are completely overlapping. Due to this problem, only the effects of direct path return, reverberation, and returns off the hydrophone baffle are removed, while bottom returns are included in the processing and feature extraction. Including the bottom return does not considerably impact the localization and detection method, since all snapshots for targets and non-targets will contain effects from the bottom. Thus, the bottom return will not be a discriminating factor between target and non-target location.

From the matched filtered version of each sonar channel, a window of 161 samples are extracted and then zero-padded to the length of the original matched filtered result. In this study, an ideal window is chosen such that the windowed matched filtered result is able to capture the bottom as well as the object returns with equal weighting of all the samples. Figure 3.12 shows the windowed matched filtered result for the typical sonar return shown in Figure 3.9(a). As can be seen, the windowing process has successfully removed the undesired portions of the signal and kept only the bottom returns and the returns of the object.

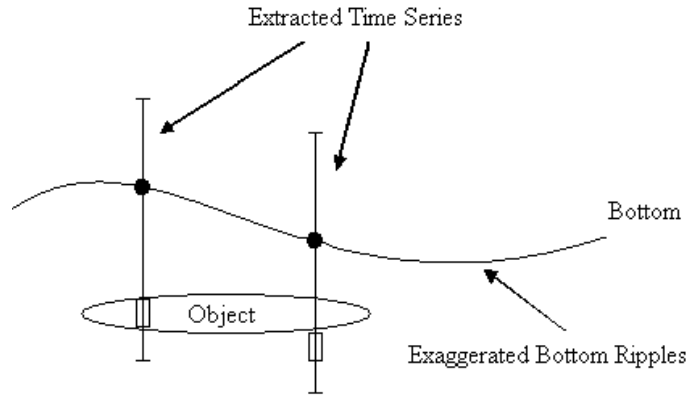
Although it is possible to dynamically adjust the starting point of the window for every sonar ping based on a peak or power detection algorithm [17] as shown in Figure 3.13(a), this

is not done due to the fact that in certain conditions, this could lead to a large amount of ping-to-ping coherence that is not dependent on the object. From this figure, we see that when the start of the window is dynamically adjusted, the bottom is located in approximately the same location in the time series from ping-to-ping, whereas the relative location of the object in the time series has changed. This leads to a large amount of coherence between pings, as far as the bottom returns are concerned, while the ping-to-ping coherence of the objects is reduced. Clearly, this is detrimental to the goal of extracting coherence-based features that represent the buried objects. In our system, the fixed window location shown in Figure 3.13(b) is used. By fixing the window starting point, the object remains in approximately the same location from ping-to-ping, hence yielding coherence patterns that are more dependent on the actual objects. The relative location of the bottom returns in the time series will vary from ping-to-ping, hence the effects of the bottom returns are somewhat less emphasized, especially in rough bottom conditions. In the Davis Point data set, samples 610 through 770 were determined to adequately capture the bottom and object returns.

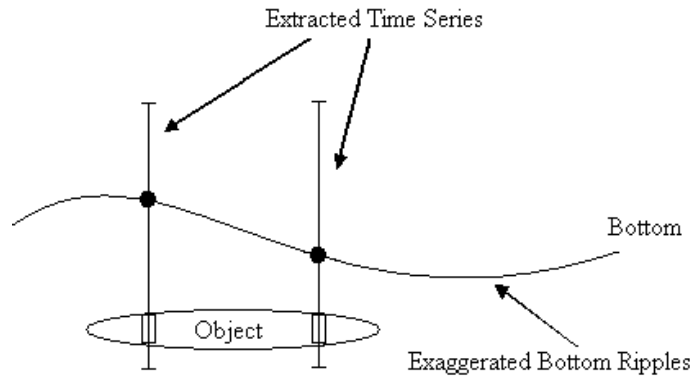
Figure 3.14 shows the recovered clean time series for the sonar return shown in Figure 3.9(a). Since zero-padding was applied during the preprocessing, the signals contain a large number of zeros, and hence only the useful part should be extracted. It is apparent from Figure 3.14 that, for the Davis Point data set, the signals of interest are located between samples 821 and 1120. Hence, for every sonar return in the Davis Point data set, 200 data points (821 to 1020) are extracted for each of the 40 receiver channels.

### 3.5 Conclusions

In this section, the data sets used to conduct the experiments presented in subsequent sections, as well as the systems used to collect them, were described. First, the PondEx10 data set was introduced. This data set was gathered in a man-made pond facility using a six-element hydrophone array mounted to a fixed rail. The linear array moved at a constant velocity through the water, and the seafloor conditions were well-controlled (i.e. level and smooth). During each sequence, five target objects were placed in precisely located target



(a) Variable window starting location.



(b) Fixed window starting location.

**Figure 3.13:** Fixed versus dynamic starting locations for the ideal window.

patches at carefully measured angular orientations with respect to the hydrophone rail. This carefully executed data acquisition provided a data set that is free of many of the types of errors typical of sonar, such as array platform motion, bottom clutter, etc. This makes this data set ideal for the proposed object localization and imaging (i.e. SAS) algorithms presented in this thesis since a rather precise ground-truth exists to which generated results may be compared.

Then, the wing BOSS system was introduced, which uses a spherical source and a rectangular receiver array built into the wings of a UUV. The wing BOSS was used to collect the Davis Point data set, which is drawn from numerous runs through the target field. These runs have wide variation of trajectories centered over many different objects in the target field. This data collection method creates a rich database of sonar returns since multiple

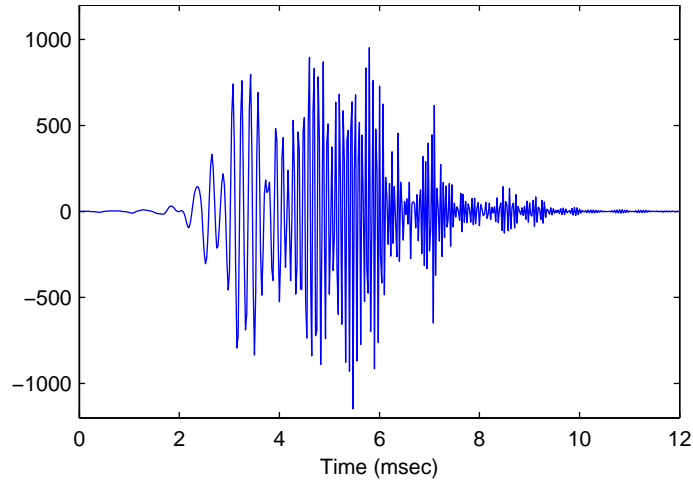


**Figure 3.14:** Inverse filtered and windowed signal for ping 300 of line T4e of the Davis Point data set.

looks of each object were captured in many cases. However, because of vehicle trajectories, not all the objects present in the target field have a large amount of data available for them.

Each sonar return must undergo preprocessing steps to allow for the application of the proposed target detection and localization method; the steps needed to accomplish this in each case were discussed. For this application, the goal of preprocessing is to extract the portion of each sonar return that corresponds to the object, even though these returns are typically overlapping with those of the bottom when an object is buried. Preprocessing for the data sets used in this study is accomplished by applying a matched filter to the raw sonar return followed by windowing so that only the portion of the signal corresponding to the object and bottom is retained, and then applying an inverse filter to the windowed matched filtered result to recover the interference-free signal. This procedure is repeated for all pings of sonar data collected for each of the objects of interest in a given data set.

In Chapter 4, a detection and localization method for underwater targets is developed which leverages concepts from the sparse representation framework. In Chapter 5, this newly developed method is applied to the PondEx10 and Davis Point data sets described in this chapter.

## CHAPTER 4

### DETECTION AND LOCALIZATION USING SPARSE REPRESENTATION

#### 4.1 Introduction

The underlying concept of sparse signal representation is to search for the most compact representation of a signal in terms of linear combinations of atoms in a predefined overcomplete dictionary. This topic has many important applications including feature selection [35, 40], signal restoration [36], and super-resolution source localization [23] - [30], among others. In the context of the work in this thesis, sparse representation approximation is proposed as a candidate solution for the problem of localization of underwater objects in sonar data. The problem of target detection lends itself readily to the application of sparse representation methods; sparsity arises naturally in this problem when the objects of interest are considered to lie on an angle of arrival or spatial coordinate grid on the seafloor defined with respect to the position of the sensor array(s). In this manner of thinking, signals propagating from a target object at a particular position are very sparse with respect to the set of all possible positions in the predefined grid. Posing the localization problem in this way results in an underdetermined linear systems problem, which are generally considered to be intractable. However, with the added constraint that the solution must be sparse, a class of solution approaches from the sparse representation framework are available for addressing this problem. This type of sparsity-constrained underdetermined linear systems problems has become a topic of increased interest in recent years [34] - [39], and only in the past decade have the fundamental conditions for sparse reconstruction become well-understood.

The upcoming sections are arranged as follows. First, in Section 4.2, formulations are presented which illustrate how target localization using sensor arrays may be framed as a sparse representation problem. It is shown here how the general sparse representation-based problem arises naturally from a far-field point source model. This discussion is used to further illuminate the challenges inherent to sonar signal processing, namely that sonar data

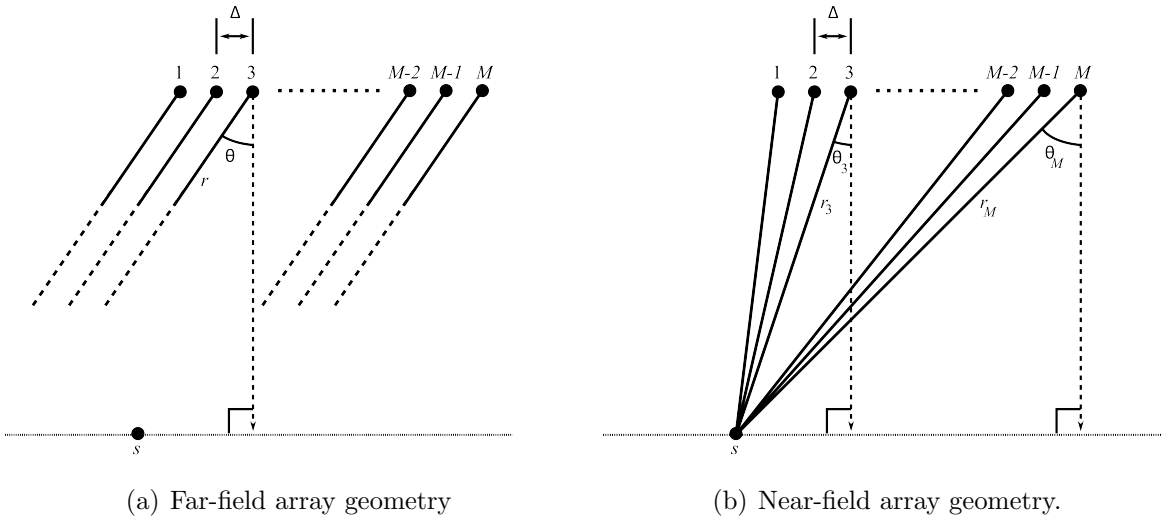


**Figure 4.1:** A comparison of far-field and near-field signal models.

is typically near-field and wideband. In Section 4.3 we provide derivations that extend the existing sparse representation-based localization framework to achieve localization of near-field wideband targets. Initially, a 1-D narrowband signal model is considered, and then this model is expanded to provide a localization method applicable to wideband near-field sources. 2-D localization is also considered. Finally, Section 4.6 provides concluding remarks regarding the proposed sparse representation-based localization method. In Chapter 5, the proposed underwater detection and localization method is demonstrated on the PondEx10 and BOSS Davis Point data sets.

## 4.2 Sensor Array Processing as a Sparse Representation Problem

The idea of achieving target detection and localization using sparse representation is not unique to this research project. In fact, it is quite straight-forward to pose far-field narrowband source localization as a sparse estimation problem, and the majority of past work in the area of sparse representation-based target localization has explored the problem that arises from a far-field signal model [23] - [27].

Consider the far-field array geometry of Figure 4.1(a), which depicts a planar wavefront propagating from source  $s$  at bearing angle  $\theta$  impinging on a linear array consisting of  $M$  sensors. At the  $n$ th snapshot, the  $M \times 1$  signal vector received by the sensor array (in the

absence of noise) may be modeled as

$$\mathbf{x}(n) = \mathbf{A}\mathbf{s}(n) \quad (4.1)$$

where  $\mathbf{s}(n)$  is the  $d \times 1$  source signal vector where  $d$  denotes the number of sources present, and  $\mathbf{A}$  is the  $M \times d$  array manifold matrix.  $\mathbf{A} = [\mathbf{a}(\theta_1), \mathbf{a}(\theta_2), \dots, \mathbf{a}(\theta_d)]$  where  $\mathbf{a}(\theta_i)$  denotes the far-field steering vector associated with source  $s_i$ . In the far-field case,  $\mathbf{A}$  captures the received signal's dependence on the source angle(s) of arrival and the sensor array geometry. One simple approach to find  $\theta_i$ 's is to reformulate this problem as an underdetermined linear systems problem by introducing an overcomplete representation of  $\mathbf{A}$ , call it  $\mathbf{A}_0$ , which represents  $N$  candidate angles of arrival where  $M \ll N$ , e.g.  $\mathbf{A}_0$  is a  $M \times N$  dictionary. Angle of arrival estimation in this case reduces to recovering  $\mathbf{s}$  that is  $d$ -sparse using one of the methods mentioned in subsection 2.5.

Now consider the near-field array geometry depicted in Figure 4.1(b). The narrowband signal received by the sensor array at the  $n$ th snapshot may similarly be modeled as

$$\mathbf{x}(n) = \mathbf{A}\mathbf{s}(n) \quad (4.2)$$

where in this case,  $\mathbf{A} = [\mathbf{a}(r_1, \theta_1), \mathbf{a}(r_2, \theta_2), \dots, \mathbf{a}(r_d, \theta_d)]$  is the array manifold matrix and  $\mathbf{a}(r_i, \theta_i)$  denotes the near-field steering vector associated with source  $s_i$ . A significant attribute of the near-field model lies in the structure of the array manifold matrix,  $\mathbf{A}$ . In the near-field case, the structure of  $\mathbf{A}$  characterizes the received signal's dependence on not only the source angle(s) of arrival and the sensor array geometry, but also on the source range(s). That is, near-field source localization involves estimation of two unknown parameters,  $\theta_i$  and  $\mathbf{r}_i$ . For this reason, the near-field array signal model does not give rise naturally to an underdetermined linear systems problem like that derived from the far-field model. It may seem reasonable in the near-field case to tackle this problem by constructing an overcomplete basis with gridding in range as well as in angle of arrival, and then to search for a solution

vector that is sparse in both range and bearing. However, due to the coupled nature of the range and angle parameters, such a problem does not have a unique angle of arrival solution, e.g. many possible combinations of range and angle may all concurrently solve this problem. Arriving at a unique expression for angle of arrival in this case requires either 1) estimating or measuring the range, and then using this fixed quantity to construct the dictionary,  $\mathbf{A}$ , or 2) reformulating the problem such that dependence on the unknown target range is eliminated.

In the underwater target localization problem at hand, the first method may be applied directly because the elevation of the sonar array platform is typically known (and the elevation may be used to map each angle in the overcomplete dictionary to a corresponding fixed range). However, it can also be shown that a sparse representation problem may equivalently be formulated that does not require estimation or measurement of the elevation/range. The work of [59] provides hints as to how this may be accomplished; therein, it is demonstrated that near-field signals impinging on corresponding sensor elements in dual symmetric subarrays are related through a simple transformation which may be shown to be independent of range (under certain assumptions and approximations). This property, often referred to as rotational invariance, has been exploited in a number of papers [59] - [65] to effectively transform near-field signal processing problems into more tractable far-field-like problems, e.g. ones that are independent of range. In keeping with this, a dual symmetric subarray model is adopted in this work to allow application of this type of near-field transformation.

In addition to implementing a signal model which allows near-field source localization to be posed as a sparse representation problem, the derivations in the upcoming sections address the challenge of dealing with wideband sonar data. From the perspective of the sparse representation framework, there two classes of strategies for handling wideband data. The first is to extend the narrowband sparse representation formulation to allow for sparse estimation in angle and frequency. This approach requires making certain assumptions regarding the sparsity profile of the data, e.g. that the data exhibits sparsity in frequency

as well as in angle, or that the data has a common sparsity profile across all frequencies. Such assumptions cannot be made about the sonar data under consideration, so in this work an alternative approach to wideband data handling is utilized. This strategy treats each frequency in the wideband data as a separate narrowband problem. Then, to allow coherent combination of all the frequency results at each ping, a frequency focusing approach like that of [66] is implemented, but simple modifications are made which allow us to take advantage of the dual symmetric subarray configuration to provide a computationally efficient wideband processing algorithm. By addressing the challenge of wideband signal processing as well as near-field source localization, this work ultimately provides a sparse representation-based technique well-suited for detection and localization of near-field targets in wideband sonar returns.

In what follows, we first derive a narrowband near-field 1D localization method in Section 4.3. A uniform linear subarray model is presented in 4.3.1 and the near-field manifold matrices associated with this sensor geometry are considered. It is shown in 4.3.2 that the steering vectors associated with the two subarrays are related through a simple transformation. It is then shown in Section 4.3.3 how the angle of arrival estimation problem arising from the subarray signal model may be posed as a sparse representation problem. Simulations on synthetic data are provided in Section 4.3.4 to validate this approach and demonstrate the capabilities of two sparse solution methods. In Section 4.4, the narrowband formulation of Section 4.3 is extended to allow for processing wideband data like that typical of sonar returns. This wideband processing scheme is based largely on the frequency focusing approach described in [66]. Lastly, Section 4.5 describes how the uniform linear subarray model of Section 4.3 naturally motivates the use of a uniform planar subarray configuration to generate a problem formulation that allows for simultaneous angle of arrival discrimination in two planes.

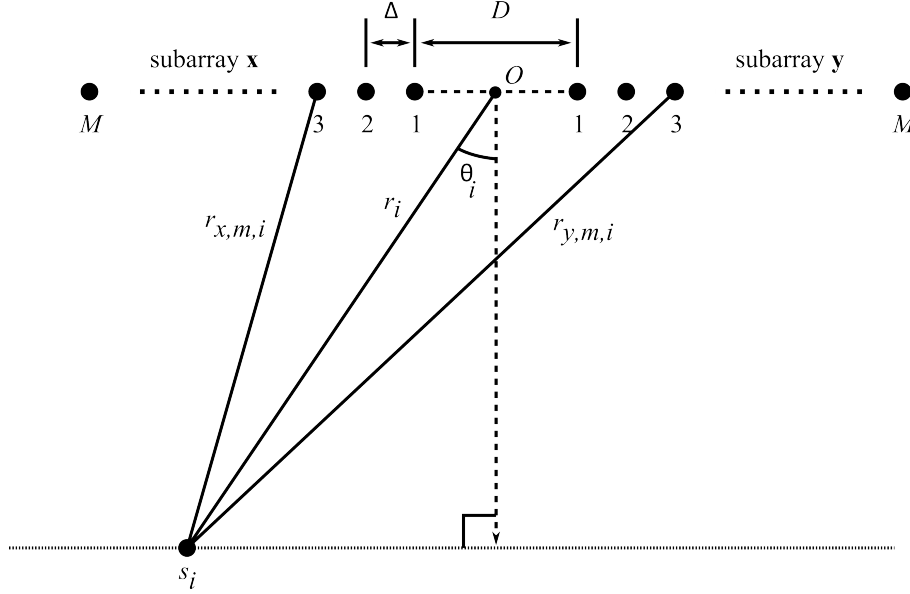


**Figure 4.2:** Uniform linear subarray for 1D angle of arrival estimation.

### 4.3 Near-Field Narrowband Array Signal Model - 1D Case

#### 4.3.1 Near-Field Array Signal Model

In order to exploit the rotational invariance property mentioned previously, a sensor configuration consisting of dual symmetric subarrays was employed. Consider two uniform linear subarrays each consisting of  $M$  sensors. Figure 4.2 shows the geometry of a near-field source,  $s_i$ , with respect to the two subarrays. The separation of the two subarrays is  $D$  and the inter-element spacing is  $\Delta$ . Assume there are  $d$  independent sources present, where  $d \leq M$ . At the  $n$ th snapshot, the signals received by the two subarrays can be modeled as

$$\begin{aligned} \mathbf{x}(n) &= \mathbf{A}_x \mathbf{s}(n) + \mathbf{n}_x(n) \\ \mathbf{y}(n) &= \mathbf{A}_y \mathbf{s}(n) + \mathbf{n}_y(n). \end{aligned} \tag{4.3}$$

Here,  $\mathbf{x}(n) \in \mathbb{C}^M$  and  $\mathbf{y}(n) \in \mathbb{C}^M$  are the output vectors of the two arrays,  $\mathbf{n}_x(n) \in \mathbb{C}^M$  and  $\mathbf{n}_y(n) \in \mathbb{C}^M$  are the zero-mean noise vectors of the two arrays,  $\mathbf{s}(n)$  is the source signal vector where  $\mathbf{s}(n) = [s_1(n), s_2(n), \dots, s_d(n)]^T$  and  $\mathbf{A}_x$  and  $\mathbf{A}_y$  are  $\mathbb{C}^{M \times d}$  subarray manifold

matrices both of which are full column rank. They can be written as

$$\begin{aligned}\mathbf{A}_x &= [\mathbf{a}_x(r_1, \theta_1), \mathbf{a}_x(r_2, \theta_2), \dots, \mathbf{a}_x(r_d, \theta_d)] \\ \mathbf{A}_y &= [\mathbf{a}_y(r_1, \theta_1), \mathbf{a}_y(r_2, \theta_2), \dots, \mathbf{a}_y(r_d, \theta_d)]\end{aligned}\tag{4.4}$$

where  $\mathbf{a}_x(r_i, \theta_i)$  and  $\mathbf{a}_y(r_i, \theta_i)$  denote the near-field steering vectors of the source  $s_i$  with respect to the two subarrays,  $i = 1, 2, \dots, d$ . Ignoring the fading affect, it follows that

$$\begin{aligned}\mathbf{a}_x(r_i, \theta_i) &= [e^{-j\frac{2\pi}{\lambda}r_{x,1,i}}, e^{-j\frac{2\pi}{\lambda}r_{x,2,i}}, \dots, e^{-j\frac{2\pi}{\lambda}r_{x,M,i}}]^T \\ \mathbf{a}_y(r_i, \theta_i) &= [e^{-j\frac{2\pi}{\lambda}r_{y,1,i}}, e^{-j\frac{2\pi}{\lambda}r_{y,2,i}}, \dots, e^{-j\frac{2\pi}{\lambda}r_{y,M,i}}]^T\end{aligned}\tag{4.5}$$

where  $i = 1, 2, \dots, d$ , operator  $T$  denotes matrix transpose, and  $r_{x,m,i}$  and  $r_{y,m,i}$  are the path lengths from the source  $s_i$  to the  $m$ th sensors of subarray  $\mathbf{x}$  and subarray  $\mathbf{y}$ , respectively. The paths  $r_{x,m,i}$  and  $r_{y,m,i}$  can be found from the geometry in Figure 4.2 using the Law of Cosines as

$$\begin{aligned}r_{x,m,i} &= \sqrt{r_i^2 + \left(\frac{D}{2} + (m-1)\Delta\right)^2 - 2r_i\left(\frac{D}{2} + (m-1)\Delta\right)\sin\theta_i} \\ r_{y,m,i} &= \sqrt{r_i^2 + \left(\frac{D}{2} + (m-1)\Delta\right)^2 + 2r_i\left(\frac{D}{2} + (m-1)\Delta\right)\sin\theta_i}\end{aligned}\tag{4.6}$$

where  $r_i$  and  $\theta_i$  are the unknown range and bearing of the source  $s_i$  with respect to the reference origin  $O$  in Figure 4.2. Let  $D = 2\alpha\Delta$  with  $\alpha > 0$  describe the relationship between the subarray separation ( $D$ ) and the inter-element spacing ( $\Delta$ ). Then,  $r_{x,m,i}$  and  $r_{y,m,i}$  can be written as

$$\begin{aligned}r_{x,m,i} &= \sqrt{r_i^2 + ((\alpha + m - 1)\Delta)^2 - 2r_i(\alpha + m - 1)\Delta\sin\theta_i} \\ r_{y,m,i} &= \sqrt{r_i^2 + ((\alpha + m - 1)\Delta)^2 + 2r_i(\alpha + m - 1)\Delta\sin\theta_i}.\end{aligned}\tag{4.7}$$

Using the steering vectors in (4.5) we can easily arrive at the relationship between the two subarrays

$$\mathbf{a}_x(r_i, \theta_i) \odot \mathbf{a}(r_i, \theta_i) = \mathbf{a}_y(r_i, \theta_i) \quad (4.8)$$

where  $\mathbf{a}(r_i, \theta_i) = [e^{-j\frac{2\pi}{\lambda}(r_{y,1,i}-r_{x,1,i})}, e^{-j\frac{2\pi}{\lambda}(r_{y,2,i}-r_{x,2,i})}, \dots, e^{-j\frac{2\pi}{\lambda}(r_{y,M,i}-r_{x,M,i})}]$  and may be considered a transformation from  $\mathbf{a}_x(r_i, \theta_i)$  to  $\mathbf{a}_y(r_i, \theta_i)$ , and  $\odot$  represents the Schurr-Hadamard, or element-wise product. In the formulation of (4.8),  $\mathbf{a}_x(r_i, \theta_i)$  and  $\mathbf{a}_y(r_i, \theta_i)$  are related through a transformation  $\mathbf{a}(r_i, \theta_i)$  which is a function of the path lengths  $r_{x,m,i}$  and  $r_{y,m,i}$  which are in turn functions of the range,  $r_i$ , and angle,  $\theta_i$  in (4.9) or (4.7). In the underwater target localization problem under consideration, the steering vectors  $\mathbf{a}(r_i, \theta_i)$  associated with each angle in the defined grid may be constructed by using the known sonar platform elevation to compute the ranges,  $r_{y,m,i}$  and  $r_{x,m,i}$ . This approach also provides a direct mapping from the angle dictionary to a grid of spatial coordinates on the seafloor.

In the next section, an approximation is presented to convert this near-field model to a “far-field-like” array signal model which can ultimately allow for the development of an angle of arrival estimation method formulated in terms of only the unknown angle of arrival,  $\theta_i$ , and independently of the range of the source,  $\mathbf{r}_i$ .

### 4.3.2 Near-Field to Far-Field Transformation

As mentioned before, the transformation  $\mathbf{a}(r_i, \theta_i)$  in (4.8) is dependent on the source angle of arrival and the *difference* between the path lengths to respective sensors in the two subarrays, i.e., on  $r_{y,m,i} - r_{x,m,i}$ . The use of dual symmetric subarrays gives rise to this relationship, which may ultimately be used to simplify the near-field localization problem to a problem that is not dependent on the unknown range. Figure 4.3 provides a visualization of the rotational invariance property as applied to the relationship between the path lengths to respective sensors in two symmetric subarrays. Note that for both cases, the source angle of arrival,  $\theta_i$ , is the same, but the range,  $r_i$ , differs between the two configurations. Despite this, it can be seen that the difference  $r_{y,m,i} - r_{x,m,i}$  is very close in magnitude for both cases. This property gives rise to a near-field to far-field transformation which is commonly

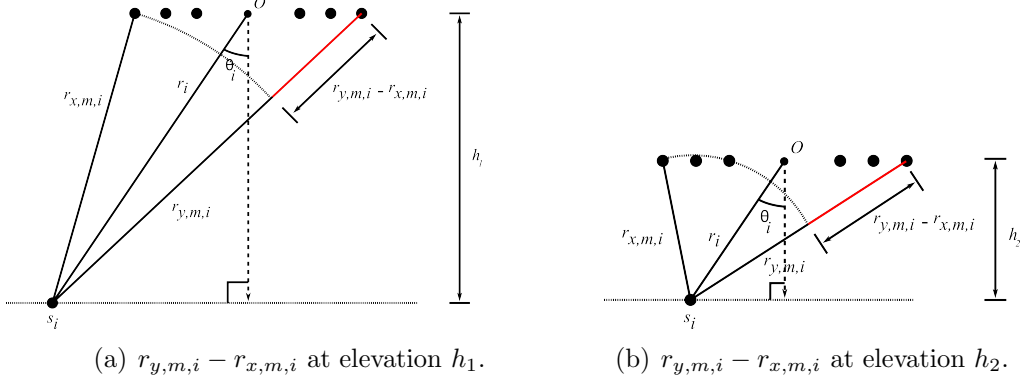


**Figure 4.3:** For a fixed source angle of arrival,  $\theta_i$ , the difference between the ranges to respective elements in two subarrays does not vary dramatically with range. Note the similar magnitude of  $r_{y,m,i} - r_{x,m,i}$  in 4.3(a) and 4.3(b), despite the disparity in range,  $r_i$ , for the two cases.

used to reduce the near-field relationship of (4.8) to an expression independent of range. This is accomplished by deriving an expression for  $\mathbf{a}(r_i, \theta_i)$  which uses an approximation of  $r_{y,m,i} - r_{x,m,i}$  that does not depend the range; i.e.,  $\mathbf{a}(r_i, \theta_i)$  may be reduced to  $\mathbf{a}(\theta_i)$ . To achieve this simplification, the approach of [59, 60] is used here, wherein the lengths  $r_{x,m,i}$  and  $r_{y,m,i}$  are approximated using the Taylor expansion, and it is ultimately shown that while the approximated lengths of  $r_{y,m,i}$  and  $r_{x,m,i}$  themselves are dependent on range, the difference  $r_{y,m,i} - r_{x,m,i}$  is not.

Defining a dummy variable for expansion,  $\beta = \frac{\Delta}{r_i}$ ,  $\Delta \ll r_i$ , the path lengths of (4.7) may be expressed as

$$\begin{aligned}
 r_{x,m,i} &= r_i \sqrt{1 + (\alpha + m - 1)^2 \beta^2 - 2(\alpha + m - 1) \sin \theta_i \beta} \\
 r_{y,m,i} &= r_i \sqrt{1 + (\alpha + m - 1)^2 \beta^2 + 2(\alpha + m - 1) \sin \theta_i \beta}.
 \end{aligned} \tag{4.9}$$

Using Taylor expansions of  $r_{x,m,i}$  and  $r_{y,m,i}$  as given by (4.9) around  $\beta = 0$  gives

$$\begin{aligned}
 r_{x,m,i} &= r_i - \Delta(\alpha + m - 1) \sin \theta_i + \frac{\Delta^2}{r_i} \frac{(\alpha + m - 1)^2}{2} \cos^2 \theta_i + H.O.T. \\
 r_{y,m,i} &= r_i + \Delta(\alpha + m - 1) \sin \theta_i + \frac{\Delta^2}{r_i} \frac{(\alpha + m - 1)^2}{2} \cos^2 \theta_i + H.O.T.
 \end{aligned} \tag{4.10}$$

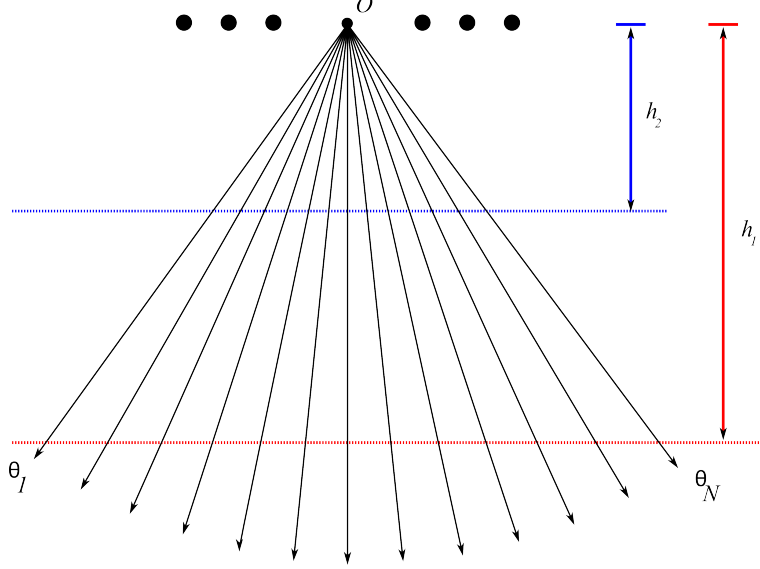


**Figure 4.4:** Using a dual subarray geometry allows the source range to be neglected, rendering the angle estimation problems at  $h_1$  and  $h_2$  equivalent.

where *H.O.T.* denotes the higher-order terms. Ignoring *H.O.T.*'s, it is easy to see that

$$r_{y,m,i} - r_{x,m,i} = 2\Delta(\alpha + m - 1) \sin \theta_i. \quad (4.11)$$

This result allows for the reformulation of (4.8), which may now be expressed as

$$\mathbf{a}_x(r_i, \theta_i) \odot \mathbf{a}(\theta_i) = \mathbf{a}_y(r_i, \theta_i) \quad (4.12)$$

where  $\mathbf{a}(\theta_i) = [e^{-j\frac{2\pi}{\lambda}2\Delta(\alpha+1-1)\sin\theta_i}, e^{-j\frac{2\pi}{\lambda}2\Delta(\alpha+2-1)\sin\theta_i}, \dots, e^{-j\frac{2\pi}{\lambda}2\Delta(\alpha+M-1)\sin\theta_i}]^T$ . Hence, by using these approximations for  $r_{y,m,i}$  and  $r_{x,m,i}$ , the steering vectors  $\mathbf{a}_y(r_i, \theta_i)$  and  $\mathbf{a}_x(r_i, \theta_i)$  may be related through a transformation  $\mathbf{a}(\theta_i)$  which is not dependent on range. Figure 4.4 provides an intuitive representation of this result. By using a dual subarray geometry, we are able to consider the angle of arrival,  $\theta_i$ , defined with respect to the subarray origin,  $O$ , without requiring knowledge of the target range. Essentially, the angle  $\theta_i$  may be projected onto a surface at  $h_1$ ,  $h_2$ , or any arbitrary elevation, and the resulting angle of arrival problems will be equivalent.

### 4.3.3 Near-Field Angle of Arrival Estimation as a Sparse Representation Problem

In a general beamforming scheme, the signals from each sensor in the detector array are combined in some manner, and then the total signal energy associated with source(s) present in some given direction,  $\theta_a$  is computed. Many strategies exist for combining the sensor array signals, as well as for quantifying the signal energy present at a particular angle. Here, the dual symmetric subarray signal model motivates the use of the signal cross-covariance as a measure of the energy at each candidate angle.

Consider the element-by-element cross-covariance at snapshot  $n$  between two length  $M$  subarray signal vectors,  $\mathbf{x}(n)$  and  $\mathbf{y}(n)$  given by their Schurr-Hadamard product,

$$\mathbf{s}_{xy} = E \{ \mathbf{x}^*(n) \odot \mathbf{y}(n) \}. \quad (4.13)$$

Using the signal model of (4.8) and invoking mutual independence of signal and noise, we have

$$\mathbf{s}_{xy} = E \left\{ \left[ \sum_{i=1}^d \mathbf{a}_x(r_i, \theta_i) s_i(n) + \mathbf{n}_x(n) \right]^* \odot \left[ \sum_{j=1}^d \mathbf{a}_y(r_j, \theta_j) s_j(n) + \mathbf{n}_y(n) \right] \right\} \quad (4.14)$$

or

$$\mathbf{s}_{xy} = \sum_{i=1}^d \mathbf{a}(r_i, \theta_i) \gamma_{si} \quad (4.15)$$

where  $\gamma_{si}$  is the variance of the  $i$ th source,  $\gamma_{si} = E \{ \mathbf{s}_i^2(n) \}$  and  $\mathbf{a}(r_i, \theta_i) = \mathbf{a}_x^*(r_i, \theta_i) \odot \mathbf{a}_y(r_i, \theta_i)$ .

The expression of (4.15) may alternatively be written using matrix notation as

$$\mathbf{s}_{xy} = \mathbf{A} \Gamma_s \quad (4.16)$$

where  $\Gamma_s = [\gamma_{s1}, \gamma_{s2}, \dots, \gamma_{sd}]^T$ , and  $\mathbf{A} = [\mathbf{a}(r_1, \theta_1), \mathbf{a}(r_2, \theta_2), \dots, \mathbf{a}(r_d, \theta_d)]$ . Equation (4.16) essentially represents a measure of energy of signals propagating from near-field sources,  $s_i$ ,

at bearing angles  $\theta_i$  and ranges  $r_i$ ,  $i = 1, 2, \dots, d$ . In practical applications, the source angles of arrival,  $\theta_i$ , are unknown and it is desirable to solve for them.

In the expression above,  $\mathbf{A}$  is a matrix representating the unknown angles of arrival of the  $d$  sources present. As mentioned before, this can readily be expressed as an underdetermined linear systems problem by introducing an overcomplete representation of  $\mathbf{A}$

$$\mathbf{s}_{xy} = \mathbf{A}_0 \Gamma_0 \quad (4.17)$$

where  $\mathbf{A}_0$  is a full dictionary of candidate angles of arrival,  $\mathbf{A}_0 \in \mathbb{C}^{M \times N}$ . In this formulation,  $\Gamma_{0,i}$  (i.e., the  $i$ th element of the vector  $\Gamma_0$ ) is zero if a source signal is not emanating from the angle corresponding to the  $i$ th column of the dictionary,  $\mathbf{A}_0$ . That is, the detection and localization amounts to finding the unknown angle(s) of arrival corresponding to locations of the non-zero terms of  $\Gamma_0$ . Several sparse reconstruction methods [38]- [46] may readily be applied to this problem, and a unique solution for  $\Gamma_0$  will be obtained if the dictionary  $\mathbf{A}_0$  is constructed to exhibit a structure that adheres to the requirements of mutual coherency and the restricted isometry property that dictate unique sparse solution recovery [34] - [36].

For the specific application of sonar signal processing, the hydrophone array elevation is typically known, and therefore the dictionary,  $\mathbf{A}_0$  in (4.17) may be constructed as  $\mathbf{A} = [\mathbf{a}(r_1, \theta_1), \mathbf{a}(r_2, \theta_2), \dots, \mathbf{a}(r_N, \theta_N)]$ . The steering vectors,  $\mathbf{a}(r_i, \theta_i)$ , may be constructed using the known platform height to compute the path lengths,  $r_{y,m,i}$  and  $r_{x,m,i}$ . That is, if the platform elevation is assumed known, each angle in the dictionary may readily be assigned a corresponding range, effectively removing the range ambiguity which makes this near-field problem challenging. However, in the event that the platform elevation is unknown, the range-independent transformation vectors obtained using the Taylor expansion may be used, i.e.  $\mathbf{A}_0 = [\mathbf{a}(\theta_1), \mathbf{a}(\theta_2), \dots, \mathbf{a}(\theta_N)]$ . In this case, angle of arrival may be estimated but no assumptions are placed on the target range. The resulting localization results may only

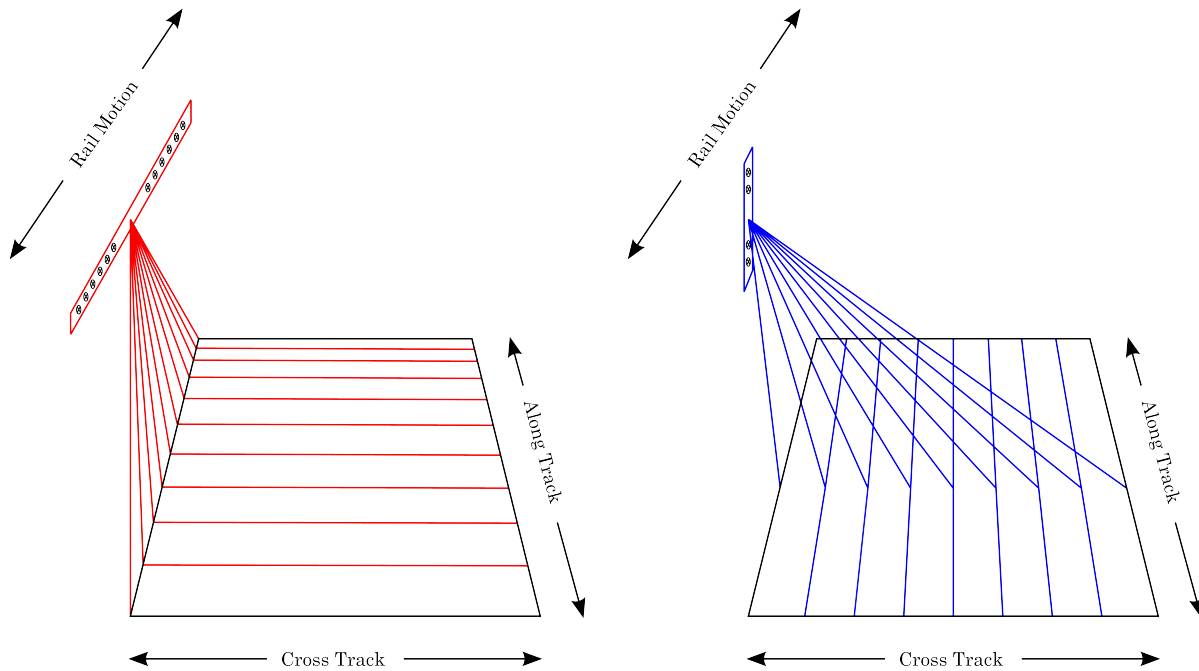


**Figure 4.5:** Two example 1D angle of arrival grids projected onto the seafloor.

be expressed in terms of angular position, rather than mapping each angle in the dictionary to a corresponding point on the seafloor.

Figure 4.5 depicts the results of projecting two example angle dictionaries onto the seafloor using the known height of the sonar platform. Note that the direction in which angle selectivity is achieved depends on the subarray orientation with respect to the target field. In Figure 4.6, it is demonstrated how two sets of linear subarrays may be combined to achieve localization in both the azimuth and elevation directions, which in this case map to along-track and cross-track spatial position on the seafloor, respectively.

#### 4.3.4 Simulations Demonstrating the 1D Near-Field Narrowband Detection and Localization Method

A simple simulation was designed to illustrate the validity of the problem formulation developed in the previous sections, and to demonstrate the implementation of the sparse representation solution methods reviewed in Section 2.5. Here it is illustrated how different levels of noise and number of sensors impact the accuracy of the estimation.

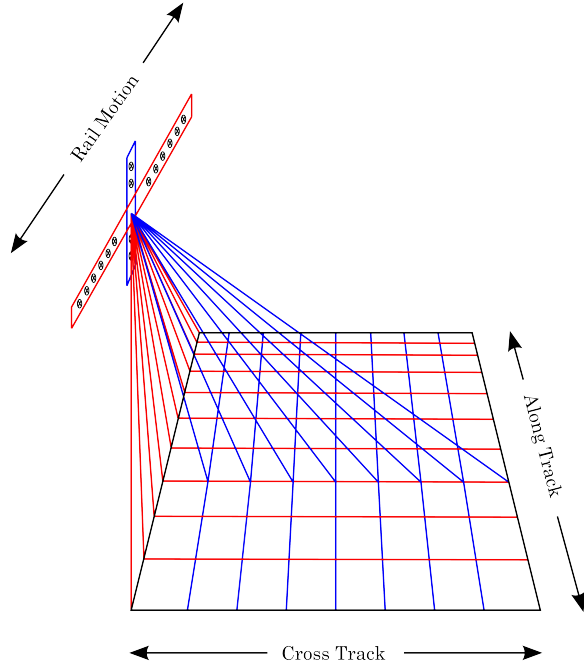


**Figure 4.6:** Overlapping azimuth and elevation dictionaries may be projected onto the seafloor to achieve 2D localization. However, when a linear subarray model is used, the two sparse representation problems must be solved separately.

Two  $M$  element subarrays like those shown in Figure 4.2 were considered. For these simulations, the inter-element spacing is  $\lambda/4$  and the displacement of the two arrays is  $D = 10\lambda$ , where  $\lambda = 0.1\text{m}$ . There are  $d = 3$  point sources, whose angles with respect to the center of the two arrays are  $\theta_1 = -20^\circ$ ,  $\theta_2 = 0^\circ$ , and  $\theta_3 = 50^\circ$ . The elevation of the sonar arrays (platform) from the plane of the sources is kept constant at  $r_0 = 3\text{m}$ . (Note that this range is used only for modeling the source signals, but is not necessary for estimating the source angles of arrival.)

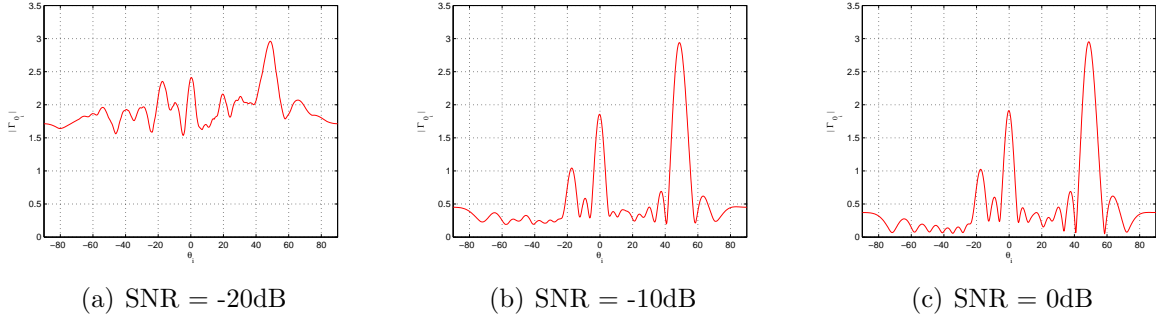
The sources are assumed to be zero-mean and independent random signals. For this simulation, they are modeled by a first-order auto-regressive (AR) model with coefficients  $\phi_i$ , i.e. at the  $n$ th snapshot,

$$s_i(n) = \phi_i s_i(n-1) + \varepsilon_i(n), \quad i \in [1, d] \quad (4.18)$$

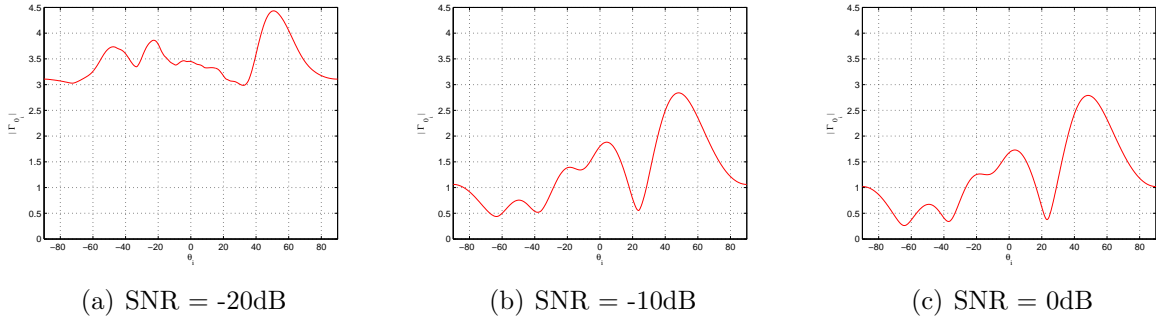
where  $\varepsilon_i(n)$ 's are the driving processes that are assumed to be independent zero-mean white Gaussian. In this case, the variance of each source is  $\sigma_{s_i}^2 = \frac{\sigma_{\varepsilon_i}^2}{1-\phi_i^2}$ . Gaussian noise is considered and the noise signals of different sensors are assumed to be uncorrelated with each other. The coefficients of the AR model in (4.18) for the 3 sources were chosen to be  $\phi_1 = 0.75$ ,  $\phi_2 = 0.85$ , and  $\phi_3 = 0.80$ , the variances of 3 sources are chosen as  $\sigma_{s_1}^2 = 1.0$ ,  $\sigma_{s_2}^2 = 2.0$ ,  $\sigma_{s_3}^2 = 3.0$ , and the  $SNR$  is set using the variances of sources. The received signal can be simulated according to (4.3), with the transformation matrices  $\mathbf{A}_x$  and  $\mathbf{A}_y$  constructed as (4.4).

Figure 4.7 and Figure 4.8 show the results of angle of arrival estimation,  $|\Gamma_{0_i}|$ , for different noise levels and numbers of sensors, which were calculated using the least-squares approximation described in Section 2.5. As can be seen in Figure 4.7, there are 3 main peaks located at  $\hat{\theta}_1 = -20.0^\circ$ ,  $\hat{\theta}_2 = 0^\circ$ , and  $\hat{\theta}_3 = 49^\circ$  when  $M = 20$  sensors are used and  $SNR \geq -10dB$ . In contrast to the least-squares results, the corresponding result when  $M = 6$  does exhibit prevalent peaks at the expected angles, with the  $M = 6$  result perhaps consisting of a combination of a larger number of bases than the  $M = 20$  result. That is, under the same noise conditions, comparable results were obtained using either six or twenty sensor elements. For the OMP sparse solution recovery, it is clear that the noise level impacts the bearing estimation more dramatically than the array length, e.g. under low noise conditions an accurate sparse solution may be obtained using a relatively short receiver array. These results should not be surprising; recall that the relationship between sensor array length was also discussed in Section 2.5, where it was shown that increased array size leads to increased mutual coherence, which is a common measure of an algorithms ability to recover a sparse solution. Refer to Figure 2.2 for a visualization of the array length vs. mutual coherence relationship.

Figure 4.9 and Figure 4.10 show the results of angle of arrival estimation,  $|\Gamma_{0_i}|$ , for different noise levels and numbers of sensors, which were calculated using the orthogonal matching pursuit algorithm described in Section 2.5. As can be seen in Figure 4.9, there are



**Figure 4.7:** Least-squares approximation of  $|\Gamma_{0_i}|$  when  $M = 20$ .



**Figure 4.8:** Least-squares approximation of  $|\Gamma_{0_i}|$  when  $M = 6$ .

3 main peaks located at  $\hat{\theta}_1 = -18.0^\circ$ ,  $\hat{\theta}_2 = 0^\circ$ , and  $\hat{\theta}_3 = 48.8^\circ$  when  $M = 20$  sensors are used and  $SNR \geq -10dB$ . In comparison, the corresponding result when  $M = 6$  does not exhibit prevalent peaks at the expected angles; the result is spread over a much wider angle region. That is, under the same noise conditions, dramatic improvements are observed by increasing the number of sensor elements from  $M = 6$  to  $M = 20$ . Comparing the results of Figures 4.10 and 4.9, it can be observed that the number of sensors impact the angle of arrival estimation results more significantly than the noise level, and the sources can be detected and localized under low  $SNR$  if more sensors are used.

In the following sections, it is demonstrated that this simple narrowband localization approach may be expanded to provide a more capable and useful localization method. First, derivations are provided which demonstrate how the narrowband method may be expanded to provide wideband signal processing capabilities. Then, the uniform linear array signal

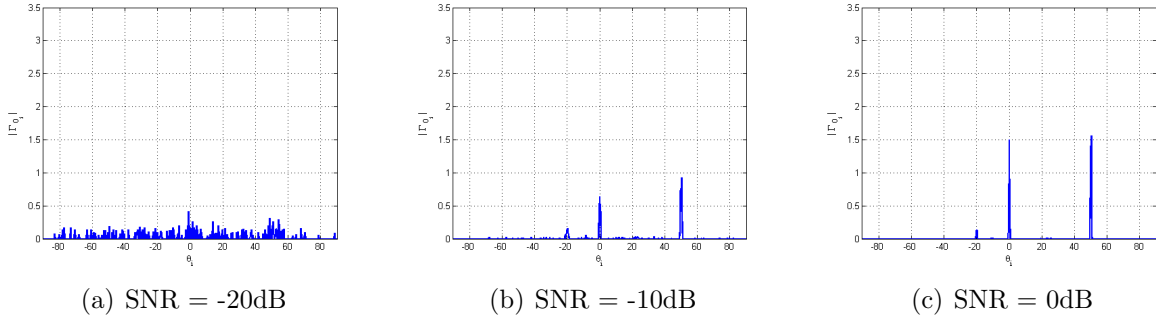


**Figure 4.9:** OMP estimation of  $|\Gamma_{0_i}|$  when  $M = 20$ .

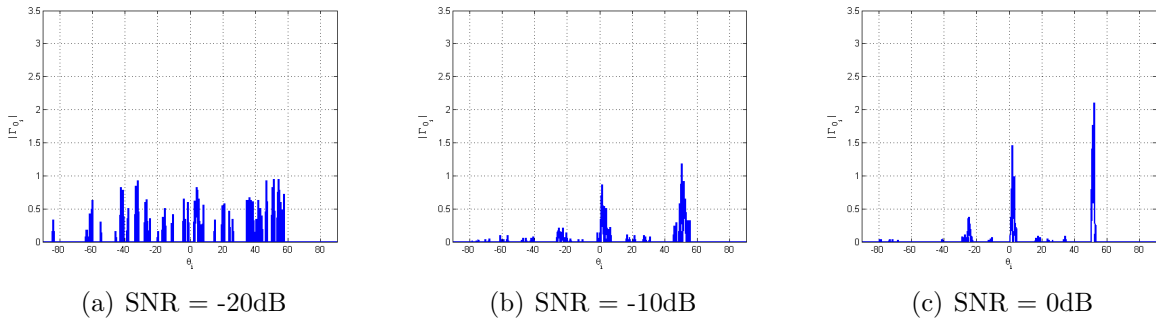


**Figure 4.10:** OMP estimation of  $|\Gamma_{0_i}|$  when  $M = 6$ .

model is expanded to a planar subarray configuration to allow for simultaneous estimation of azimuth and elevation arrival angles.

#### 4.4 Extension to Wideband Signals

The problem formulation of (4.17) is identical to the type of sparsity-constrained underdetermined linear systems problems introduced in Section 2.2. However, because this formulation arises from a narrowband signal model, it is not immediately applicable to the wideband data typical of sonar returns. In the context of sparse representation, there are three general approaches for handling wideband signals.

1. The first is to search for a solution which is sparse in both the angle of arrival *and* in frequency. For this approach, the wideband data would be vectorized and an overcomplete dictionary would be constructed with gridding in the frequency dimension as well as in angle. A solution would then be sought that is sparse in this frequency/angle basis.

2. The second approach is to assume that for a given snapshot, a wideband signal exhibits a common sparsity profile across all frequencies. This ‘joint-sparsity’ assumption allows for the application of methods from the field of block-sparse representation.
3. The third and perhaps the simplest approach is to treat each frequency in the wideband data as a separate narrowband problem of the type previously considered, and then by some means coherently combine the angle of arrival results from all frequency bands into a single result at each ping.

In the case of target signatures present in sonar data, sparsity in frequency (as required for Method 1) is not a good assumption, and neither is the assumption of a jointly-sparse profile across all frequency bands (required for Method 2). Therefore, in this work, the third approach is adopted and processing steps are incorporated to treat each frequency present in the wideband data as a separate narrowband signal. The following notational convention is used throughout this section: the frequency dependent observation vector,  $\mathbf{x}(f_k, \theta_i, r_i)$  is expressed as  $\mathbf{x}(f_k)$ . While this quantity is dependent on range and angle of arrival of the  $i$ th source as well as frequency band, for the purpose of notational simplicity only the frequency-dependent relationships are expressed here.

The frequency focusing method used in this work borrows from the concepts presented in [66]. Therein, the wideband signal is effectively collapsed to a single common frequency in order to allow for solving a single angle of arrival problem at each ping. In order to achieve this, a frequency-dependent focusing operator,  $\mathbf{T}(f_k)$  is used to focus the data at each frequency,  $f_k$ , to a common frequency,  $f_0$ . At each frequency, these focused data are used to form the covariance matrix,  $\mathbf{s}_{xx}$ . Then, the covariance matrices associated with each of the  $K$  total frequencies are combined into a single effective covariance matrix.

In this research, the general approach of [66] is applied rather directly, with a small modification to allow for the dual subarray configuration in this work. Focusing transformations

$\mathbf{T}_x(f_k)$  and  $\mathbf{T}_y(f_k)$  are defined to focus the data vectors  $\mathbf{x}(f_k)$  and  $\mathbf{y}(f_k)$  to  $\mathbf{x}(f_0)$  and  $\mathbf{y}(f_0)$ , respectively. Unitary focusing matrices of the form used in [66] are chosen here, i.e.,

$$\begin{aligned}\mathbf{T}_x(f_k) &= \text{diag}[a_{x1}(f_0)/a_{x1}(f_k), a_{x2}(f_0)/a_{x2}(f_k), \dots, a_{xM}(f_0)/a_{xM}(f_k)] \\ \mathbf{T}_y(f_k) &= \text{diag}[a_{y1}(f_0)/a_{y1}(f_k), a_{y2}(f_0)/a_{y2}(f_k), \dots, a_{yM}(f_0)/a_{yM}(f_k)]\end{aligned}\tag{4.19}$$

where  $a_{xi}(f_k)$  is the  $i$ th element of the steering vector  $\mathbf{a}_x(f_k)$  at the frequency  $f_k$ . The cross-covariance measure of signal energy formed using these focused data vectors can be written as

$$\mathbf{s}_{xy}(f_{0k}) = E\{\mathbf{T}_x^*(f_k)\mathbf{x}^*(f_k) \odot \mathbf{T}_y(f_k)\mathbf{y}(f_k)\}.\tag{4.20}$$

where  $\mathbf{s}_{xy}(f_{0k})$  denotes the focused cross-covariance computed at the  $k$ th frequency band. This may equivalently be written as

$$\mathbf{s}_{xy}(f_{0k}) = \mathbf{T}_x^*(f_k)\mathbf{T}_y(f_k)E\{\mathbf{x}^*(f_k) \odot \mathbf{y}(f_k)\}\tag{4.21}$$

which simplifies to

$$\mathbf{s}_{xy}(f_{0k}) = \mathbf{T}_{xy}(f_k)\mathbf{s}_{xy}(f_k)\tag{4.22}$$

where  $\mathbf{T}_{xy}(f_k) = \mathbf{T}_x^*(f_k)\mathbf{T}_y(f_k)$ . In other words, a single focusing computation may be applied to  $\mathbf{s}_{xy}(f_k)$  which incorporates the transformation for both data vectors, rather than focusing the subarray data separately. The approaches are equivalent, but due to the array geometry utilized here we may make this convenient computational simplification. After  $\mathbf{s}_{xy}(f_{0k})$  is computed for all  $K$  frequencies, these quantities may be coherently averaged to give an effective cross-covariance matrix for the wideband signal. The frequency focusing algorithm built from this approach is outlined next.

## Frequency Focusing Algorithm

**Goal:** Form focused effective cross-covariance for wideband data, find one sparse angle of arrival estimate at each ping.

**For each ping:**

1. For each frequency,  $f_k, k = 1 \dots K$ :
  - Form subarray signals,  $\mathbf{x}(f_k)$  and  $\mathbf{y}(f_k)$ .
  - Form cross-covariance,  $\mathbf{s}_{xy}(f_k) = E\{\mathbf{x}^*(f_k) \odot \mathbf{y}(f_k)\}$
  - Focus this cross-covariance to frequency,  $f_0$ ,

$$\mathbf{s}_{xy}(f_{0k}) = \mathbf{T}_{xy}(f_k)\mathbf{s}_{xy}(f_k).$$

2. Form coherent average of focused cross-covariances to give one effective cross-covariance,

$$\hat{\mathbf{s}}_{xy}(f_0) = \frac{1}{K} \sum_{k=1}^K \mathbf{s}_{xy}(f_{0k})$$

3. Compute angle of arrival using effective cross-covariance:

- Solve  $\hat{\mathbf{s}}_{xy}(f_0) = \mathbf{A}(f_0)\hat{\Gamma}(f_0)$  for  $\hat{\Gamma}(f_0)$  using fixed dictionary  $\mathbf{A}(f_0)$ .

### 4.5 Near-field Narrowband Array Signal Model - 2D Case

The uniform linear subarray geometry used to develop the sparse representation problem in the previous sections only allows for discrimination of the angle of arrival of a target in a single plane, i.e. only azimuth *or* elevation may be estimated using the proposed approach. For the purpose of this research, such a 1D solution approach is sufficient, because the resultant SAS-like images can be compared directly with images generated using delay-and-sum SAS and SAS-like acoustic color processing. However, it is interesting to note that the

1D problem formulation may easily be extended to allow for simultaneous approximation of azimuth and elevation angle of arrival. As in the 1D case, it is desirable to devise an array geometry which leads to a useful relationship that is not dependent on the unknown range. The dual linear subarray configuration in the previous section motivates a rather direct extension to a 2D problem formulation.

Consider two uniform planar subarrays each consisting of  $M \times N$  sensors. Figure 4.11 shows the geometry of the near-field source  $s_i$  with respect to the two subarrays. The horizontal separation of the two subarrays is  $D$  and the horizontal inter-element spacing is  $\Delta_m$ . The vertical separation of the two subarrays is  $H$  and the vertical inter-element spacing is  $\Delta_n$ . Assume there are  $d$  independent sources present, where  $d \leq MN$ . At the  $n$ th snapshot, the signals received by the two subarrays can be modeled as

$$\begin{aligned}\mathbf{x}(n) &= \mathbf{A}_x \mathbf{s}(n) + \mathbf{n}_x(n) \\ \mathbf{y}(n) &= \mathbf{A}_y \mathbf{s}(n) + \mathbf{n}_y(n).\end{aligned}\tag{4.23}$$

Here,  $\mathbf{x}(n) \in \mathbb{C}^{MN}$  and  $\mathbf{y}(n) \in \mathbb{C}^{MN}$  are the output vectors of the two subarrays,  $\mathbf{n}_x(n) \in \mathbb{C}^{MN}$  and  $\mathbf{n}_y(n) \in \mathbb{C}^{MN}$  are the zero-mean noise vectors of the two subarrays,  $\mathbf{s}(n)$  is the source signal vector where  $\mathbf{s}(n) = [s_1(n), s_2(n), \dots, s_d(n)]^T$ . and  $\mathbf{A}_x$  and  $\mathbf{A}_y$  are  $\mathbb{C}^{MN \times d}$  subarray manifold matrices, both of which are full column rank. They can be written as

$$\begin{aligned}\mathbf{A}_x &= [\mathbf{a}_x(r_1, \theta_1, \phi_1), \mathbf{a}_x(r_2, \theta_2, \phi_2), \dots, \mathbf{a}_x(r_d, \theta_d, \phi_d)] \\ \mathbf{A}_y &= [\mathbf{a}_y(r_1, \theta_1, \phi_1), \mathbf{a}_y(r_2, \theta_2, \phi_2), \dots, \mathbf{a}_y(r_d, \theta_d, \phi_d)],\end{aligned}\tag{4.24}$$

where  $\mathbf{a}_x(r_i, \theta_i, \phi_i)$  and  $\mathbf{a}_y(r_i, \theta_i, \phi_i)$  denote the length  $MN$  near-field steering vectors of the source  $s_i$  with respect to the two subarrays,  $i = 1, 2, \dots, d$ . Ignoring the fading affect, it

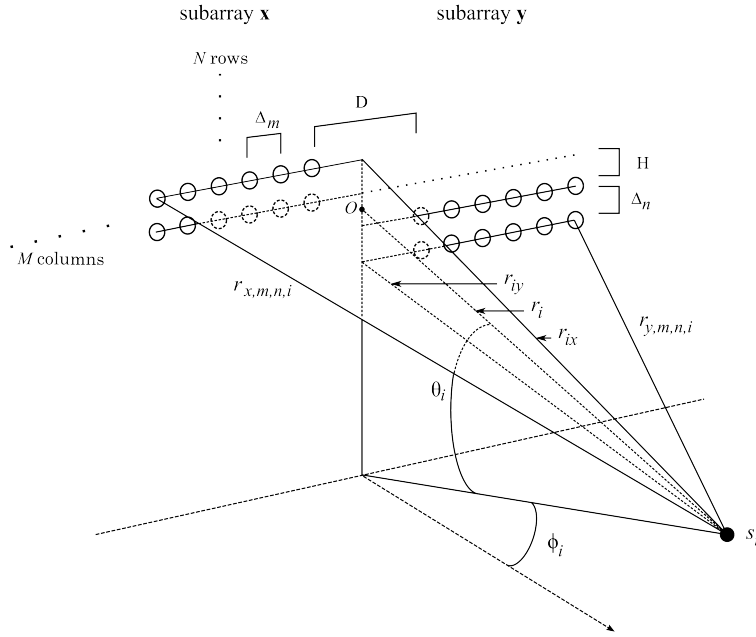


**Figure 4.11:** Uniform planar subarray geometry for 2D angle of arrival estimation.

follows that

$$\begin{aligned}
 \mathbf{a}_x(r_i, \theta_i, \phi_i) &= [e^{-j\frac{2\pi}{\lambda}r_{x,1,1,i}}, \dots, e^{-j\frac{2\pi}{\lambda}r_{x,M,1,i}}, e^{-j\frac{2\pi}{\lambda}r_{x,1,2,i}}, \dots, e^{-j\frac{2\pi}{\lambda}r_{x,M,2,i}}, \dots, \\
 &\quad e^{-j\frac{2\pi}{\lambda}r_{x,1,N,i}}, \dots, e^{-j\frac{2\pi}{\lambda}r_{x,M,N,i}}]^T \\
 \mathbf{a}_y(r_i, \theta_i, \phi_i) &= [e^{-j\frac{2\pi}{\lambda}r_{y,1,1,i}}, \dots, e^{-j\frac{2\pi}{\lambda}r_{y,M,1,i}}, e^{-j\frac{2\pi}{\lambda}r_{y,1,2,i}}, \dots, e^{-j\frac{2\pi}{\lambda}r_{y,M,2,i}}, \dots, \\
 &\quad e^{-j\frac{2\pi}{\lambda}r_{y,1,N,i}}, \dots, e^{-j\frac{2\pi}{\lambda}r_{y,M,N,i}}]^T
 \end{aligned} \tag{4.25}$$

where  $i = 1, 2, \dots, d$ , operator  $T$  denotes matrix transpose, and  $r_{x,m,n,i}$  and  $r_{y,m,n,i}$  are the paths from the source  $s_i$  to the  $(m, n)$ th sensors of subarray  $\mathbf{x}$  and subarray  $\mathbf{y}$ , respectively. As with the 1D signal model, the paths  $r_{x,m,n,i}$  and  $r_{y,m,n,i}$  may be found from the geometry in Figure 4.11. First, the Law of Cosines can be used to find  $r_{ix}$  and  $r_{iy}$  as

$$\begin{aligned}
 r_{ix} &= \sqrt{r_i^2 + \left(\frac{H}{2} + (n-1)\Delta_n\right)^2 + 2r_i\left(\frac{H}{2} + (n-1)\Delta_n\right)\sin\theta_i} \\
 r_{iy} &= \sqrt{r_i^2 + \left(\frac{H}{2} + (n-1)\Delta_n\right)^2 - 2r_i\left(\frac{H}{2} + (n-1)\Delta_n\right)\sin\theta_i},
 \end{aligned} \tag{4.26}$$

where  $r_i$  and  $\theta_i$  are the unknown range and elevation angle of the source  $s_i$  with respect to the reference origin  $O$  in Figure 4.11. Using these lengths  $r_{ix}$  and  $r_{iy}$  and applying the Law of Cosines a second time leads to the following expression for the paths  $r_{x,m,n,i}$  and  $r_{y,m,n,i}$ .

$$\begin{aligned} r_{x,m,n,i} &= \sqrt{r_{ix}^2 + \left(\frac{D}{2} + (m-1)\Delta_m\right)^2 - 2r_i\left(\frac{D}{2} + (m-1)\Delta_m\right)\sin\phi_i} \\ r_{y,m,n,i} &= \sqrt{r_{iy}^2 + \left(\frac{D}{2} + (m-1)\Delta_m\right)^2 + 2r_i\left(\frac{D}{2} + (m-1)\Delta_m\right)\sin\phi_i}, \end{aligned} \quad (4.27)$$

where  $\phi$  denotes the unknown azimuth angle of the source  $s_i$  with respect to the reference origin. Equation (4.26) may then be substituted into (4.27) and the resulting path lengths substituted into the steering vectors of (4.25). A relationship like that of the one-dimensional signal model results.

$$\mathbf{a}_x(r_i, \theta_i, \phi_i) \odot \mathbf{a}(r_i, \theta_i, \phi_i) = \mathbf{a}_y(r_i, \theta_i, \phi_i) \quad (4.28)$$

where  $\mathbf{a}(r_i, \theta_i, \phi_i) = [e^{-j\frac{2\pi}{\lambda}(r_{y,1,1,i}-r_{x,1,1,i})}, \dots, e^{-j\frac{2\pi}{\lambda}(r_{y,M,1,i}-r_{x,M,1,i})}, e^{-j\frac{2\pi}{\lambda}(r_{y,1,2,i}-r_{x,1,2,i})}, \dots, e^{-j\frac{2\pi}{\lambda}(r_{y,M,2,i}-r_{x,M,2,i})}, \dots, e^{-j\frac{2\pi}{\lambda}(r_{y,1,N,i}-r_{x,1,N,i})}, \dots, e^{-j\frac{2\pi}{\lambda}(r_{y,M,N,i}-r_{x,M,N,i})}]^T$  is a length  $MN$  vector which may be considered a transformation relating  $\mathbf{a}_x(r_i, \theta_i, \phi_i)$  and  $\mathbf{a}_y(r_i, \theta_i, \phi_i)$ .

Now it is evident that the transformation  $\mathbf{a}(r_i, \theta_i, \phi_i)$  is dependent on the *difference* between the path lengths to corresponding sensors in the two respective arrays. As for the 1D case, we may construct an overcomplete dictionary by either using a known platform height to compute the ranges  $r_{y,m,n,i}$  and  $r_{x,m,n,i}$  associated with each angle grid, or by approximating the difference  $r_{y,m,n,i} - r_{x,m,n,i}$  using a Taylor expansion to yield an expression that is not dependent on the unknown range.

Again, by analyzing the element-by-element cross-covariance vector of the measurements from the two subarrays, we can formulate a source localization problem in the same manner as in the 1D case. This yields

$$\mathbf{s}_{xy} = \mathbf{A}\Gamma_s \quad (4.29)$$

where  $\Gamma_s = [\gamma_{s1}, \gamma_{s2}, \dots, \gamma_{sd}]^T$ , and  $\mathbf{A} = [\mathbf{a}(r_1, \theta_1, \phi_1), \mathbf{a}(r_2, \theta_2, \phi_2), \dots, \mathbf{a}(r_d, \theta_d, \phi_d)]$ . We can re-write this as a sparse representation problem

$$\mathbf{s}_{xy} = \mathbf{A}_0 \Gamma_0 \quad (4.30)$$

where  $\mathbf{A}_0$  is the full dictionary of possible source angles of arrival,  $\mathbf{A}_0 \in \mathbb{C}^{MN \times N_1 N_2}$ ,  $\Gamma_0 \in \mathbb{C}^{N_1 N_2 \times 1}$ . Here,  $N_1$  is the number of angles in the  $\phi$  dictionary and  $N_2$  is the number of angles in the  $\theta$  dictionary, i.e.  $N_1$  and  $N_2$  are indicative of the resolution of the angle of arrival search grid utilized in solving the localization problem. Again,  $\Gamma_{0,i} = 0$  if the  $i$ th source is not present. Hence, it is clear that finding the unknown angles of arrival,  $\phi$  and  $\theta$ , can be thought of as seeking the locations and values of the non-zero terms of  $\Gamma_0$ . In this formulation, the azimuth and elevation angles may be estimated simultaneously. Figure 4.12 portrays the 2D angle of arrival grid obtained by forming uniform planar subarrays projected onto the seafloor.

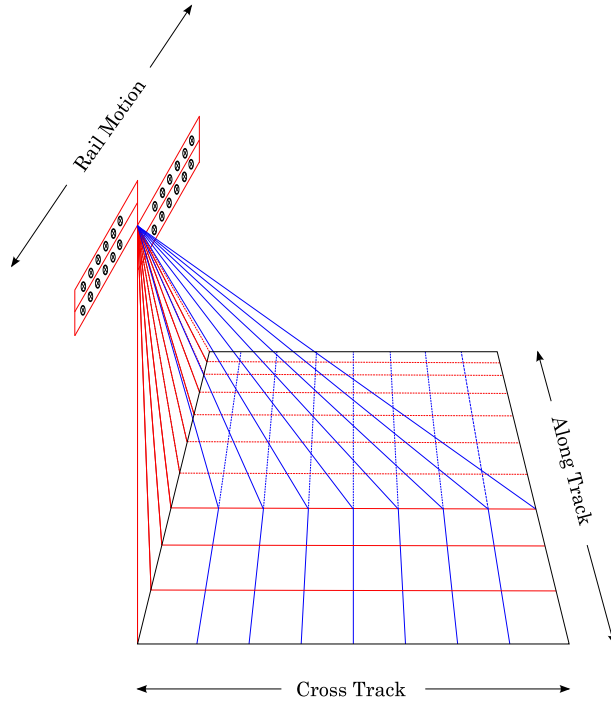


**Figure 4.12:** 2D angle grid formed by using dual symmetric planar subarrays projected onto seafloor.

## 4.6 Conclusions

The derivations of Section 4.2 demonstrate how target localization may be posed as a sparse representation problem. In fact, it is very straight forward to derive a sparse representation problem from a far-field narrowband signal model. However, in this work we consider wideband sonar returns collected in the near-field region, therefore such a model cannot adequately characterize the data. In order to apply sparse representation methods to wideband near-field sonar data, steps were taken to reformulate the problem into one that allows for utilization of sparse representation techniques.

First, the near-field characteristic of sonar returns was considered in Section 4.3. Near-field localization, unlike the far-field case, does not give rise naturally to a sparse recovery problem due to the fact that near-field target localization is dependent on target range in addition to angle of arrival. The coupled nature of these two quantities leads to a problem formulation that does not produce unique results, e.g. many potential combinations of range and bearing may equivalently solve the problem. To deal with this complication, steps are taken to reformulate the near-field problem as one that is not dependent on the unknown source range so that the unknown angle of arrival may be estimated using sparse recovery methods. The concept used in this research leverages the fact that a range-independent relationship exists between signals collected by dual symmetric subarrays. In this work, a uniform linear subarray signal model is adopted which ultimately allows a sparse representation problem to be formulated in terms of the range-independent transformation that relates the signals received by the two subarrays. Working from such a subarray signal model leads to a problem which can be solved using standard far-field methods. The near-field-to-far-field transformation and the resulting 1D sparse representation problem were discussed in Section 4.3. Simulations were provided to validate this problem formulation and demonstrate two sparse solutions methods considered in this research.

Secondly, processing steps were developed in Section 4.4 to allow for handling the wide-band data typical of sonar signals. In this work, each frequency sub-band present in the data

is treated as a separate narrowband signal processing problem. In order to allow coherent combination of the results from all frequencies, a focusing operator was introduced to transform the results to a common frequency. In the frequency focusing method used here, the data cross-covariance is averaged across all focused frequencies for a given ping and a single angle of arrival estimate is computed. This approach requires focusing the data at each frequency band to a common frequency to allow for the cross-covariances to be coherently combined.

Additionally, it was also demonstrated in Section 4.5 that the 1D localization method can easily be extended to achieve 2D localization for simultaneous azimuth and elevation estimation by employing a dual planar subarray configuration. In this work, the 1D method is used to generate SAS-like results images, since this approach produces images which can readily be compared to the results obtained using alternative sonar processing methods such as delay-and-sum SAS [55] or the SAS-like acoustic color processing of [7], [8]. These results are presented in the next chapter.

## CHAPTER 5

### EXPERIMENTAL RESULTS ON SONAR DATA

#### 5.1 Introduction

In this chapter, the sparse representation-based near-field source localization method developed in Chapter 4 is applied to two data sets. The first data set, ‘Pond Experiment 2010’, or PondEx10, was collected under very controlled conditions using a hydrophone array mounted to a fixed rail system in a man-made pond facility. The second data set, the Davis Point data set, was collected in a natural body of water using a hydrophone array mounted to an unmanned underwater vehicle. In this work, the controlled nature of the PondEx10 data set made it very useful for evaluating new sonar processing methods. The PondEx10 data set was collected using a rail-mounted hydrophone system traveling at a known velocity. The target objects were carefully positioned, and the seafloor conditions were well controlled, e.g. the sandy bottom was smoothed prior to data acquisition, and the target region was kept free of clutter. Due to these characteristics, the truth for this data set is well-defined. In contrast, the Davis Point data set, which was collected using a UUV-mounted sonar system, provided interesting challenges due to the less controlled nature of the data acquisition and the varying seafloor conditions present in the search region. This data set is more representative of sonar data collected under natural conditions, and exhibits the effects of non-uniform UUV motion as well as non-ideal seafloor conditions. Despite these challenges, the Davis Point BOSS data is appropriate for use with the new sparse representation-based localization method due to the physical configuration of the sensors on the UUV wings. The 40 channel BOSS data allows for the dual subarray geometry proposed in Chapter 4 to be achieved in a variety of ways. Conversely, the possible subarray configurations that can be formed using the six PondEx10 channels is limited. These two data sets and the conditions under which they were collected are described in detail in Chapter 3.

The remainder of this chapter is organized as follows. First, the processing steps applied to the two data sets are described in Section 5.2. This section describes the construction of the uniform subarrays from the available data points in each data set and discusses the manner in which successive pings or adjacent channels are combined to create SAS-like images. Then, in Section 5.3, target localization results are presented for the PondEx10 data set. Localization and detection are performed using two sparse solution algorithms, namely orthogonal matching pursuit [41, 44, 45] and least-squares approximation [25, 43, 46]. The results obtained using the newly developed near-field source localization method are compared and contrasted with images generated using omega- $k$  SAS processing [7, 8]. In Section 5.4, the new detection and localization method is applied to the Davis Point BOSS data. The results are compared and contrasted with images formed using traditional delay-and-sum SAS [52, 53]. Concluding remarks are provided in Section 5.5.

## 5.2 Subarray Formation

In order to facilitate near-field localization using the methods prescribed in Chapter 4, a dual symmetric subarray geometry was adopted. For the results presented in this report, linear subarrays were constructed which allowed for angle of arrival estimation in a single plane. The construction of the dual linear subarrays and the resultant angle of arrival estimates for the PondEx10 and BOSS Davis Point data sequences are dictated by the physical geometry of the sensor arrays used to collect the data, i.e. the six-element vertical hydrophone array used to collect the PondEx10 data versus the horizontal wing hydrophone arrays of the BOSS system used to collect the Davis Point sequences.

For the PondEx10 data sequences, the  $\mathbf{x}$  and  $\mathbf{y}$  subarrays of length  $M = 8$  are formed in the synthetic aperture direction with  $D = 2$  ping separation between the two subarrays, which allows for angle of arrival discrimination in the along-track direction (i.e. source azimuth). In this case, the expectation operation of (4.13) is performed in the real-aperture direction, i.e. over the six channels of the PondEx10 data. The PondEx10 subarray formation and averaging operation are depicted in Figure 5.1.

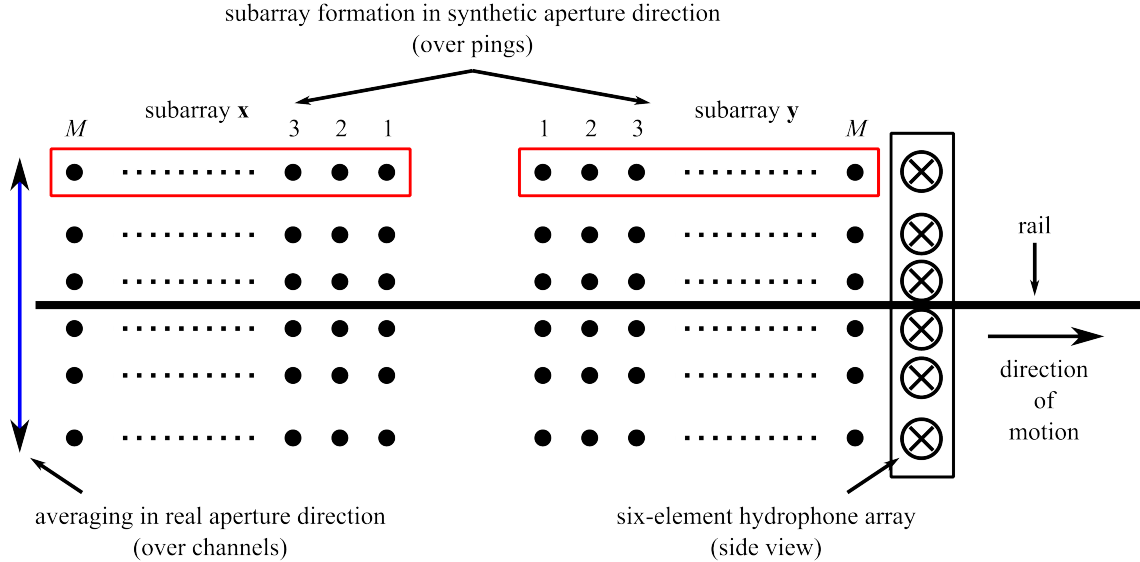


**Figure 5.1:** PondEx10 data set subarray construction and averaging operation.

For the BOSS Davis Point data sequences, the  $\mathbf{x}$  and  $\mathbf{y}$  subarrays of length  $M = 10$  are formed in the real aperture direction by using the signals from every other sensor on the 20-element arrays on each wing of the BOSS system, with subarray separation of  $D = 0.5m$  which is the distance between the two wings of the BOSS system. Construction of the subarrays in the real aperture direction allows for angle of arrival discrimination in the across-track direction (i.e. source elevation). In this case, the expectation operation of (4.13) is performed in the synthetic aperture direction over 20 consecutive pings of the Davis Point data. The Davis Point subarray formation and averaging operation are depicted in Figure 5.2.

### 5.3 Localization of Targets in PondEx10 Data Set

The results of applying the sparse representation-based localization method to the PondEx10 data are shown in this section. Figures 5.3(a) and 5.3(b) show the results of applying the sparse solution approach to PondEx10 Run 185 using the least-squares method and the OMP algorithm, respectively. In both cases, the subarray length is fixed at  $M = 8$  sensors, and the search angle range is set to  $-\pi/8$  to  $\pi/8$ . In Run 185, all of the targets are placed

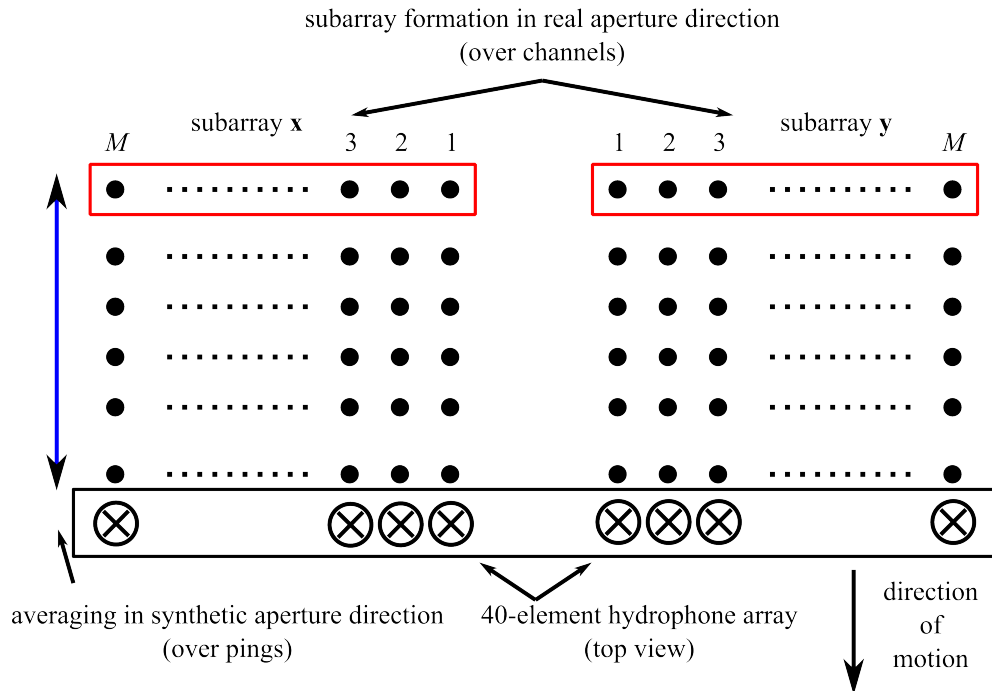
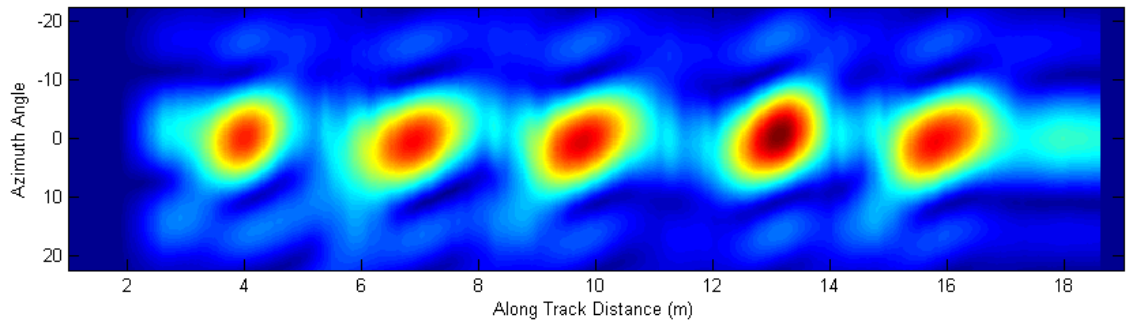


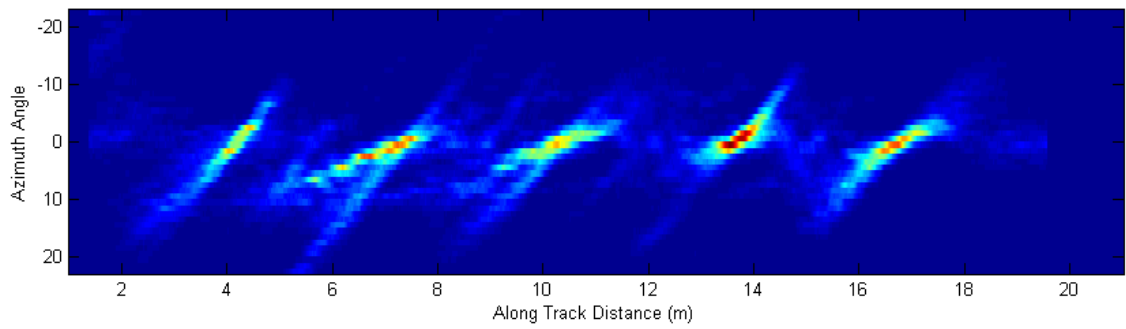
**Figure 5.2:** BOSS Davis Point data set subarray construction and averaging operation.

half-proud on the seafloor at a grazing angle of  $20^\circ$ . The five objects are oriented broadside to the rail-mounted hydrophone array, and the bottom of the test field was been freshly smoothed since this was the first data run gathered during the half-proud PondEx10 experiments. From these results, it is evident that the least-squares approach provides a better depiction of source location, despite the fact that this approach does not provide a sparse solution. This may be attributed to the fact that the targets are not point targets, as is assumed in the formulations.

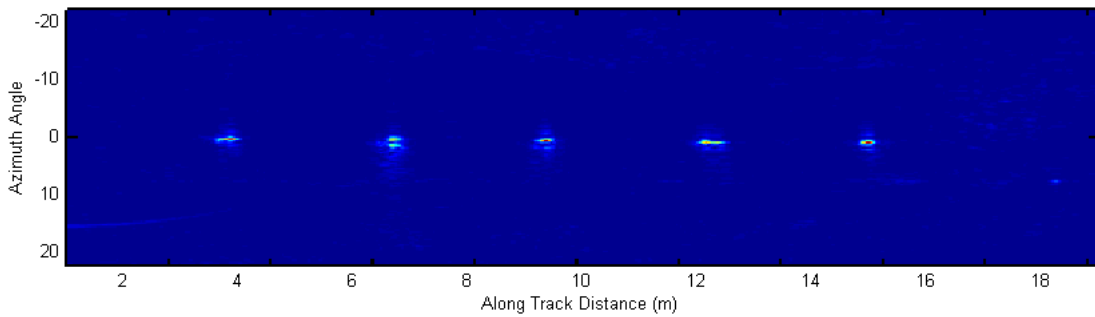
Figure 5.4 shows the results of applying the sparse solution approach to PondEx10 Run 191. Subfigures 5.4(a) and 5.4(b) depict the results of using the least-squares solution approach and the OMP algorithm, respectively. In both cases, the subarray length is fixed at  $M = 8$  sensors, and the search angle range is set to  $-\pi/8$  to  $\pi/8$ . In Run 191, the targets are positioned with their major axes  $80^\circ$  off parallel with their blunt ends pointed towards the rail (designated  $+80^\circ$ ). From these results, it is again clear that the least-squares approach



(a) Angle estimation using least-squares.



(b) Angle estimation using OMP.



(c) Localization using omega- $k$  SAS processing.

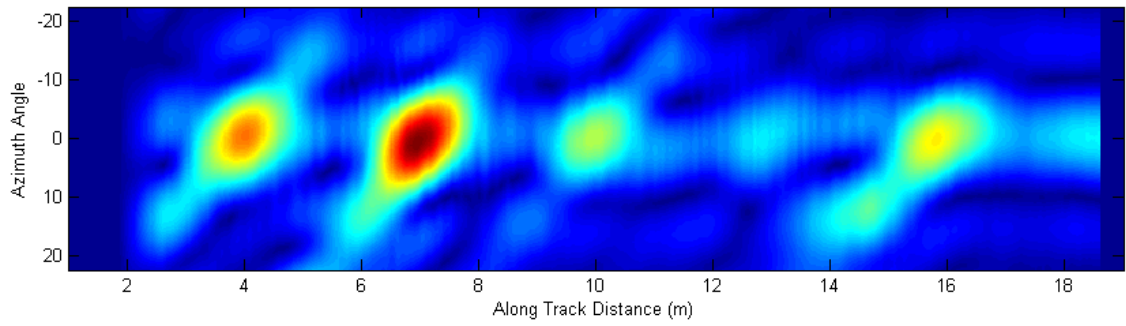
**Figure 5.3:** Target localization for PondEx10 run 185.

provides a better SAS-like image of source location with much better localization when compared to that generated using the OMP method. These results may also be contrasted with the results of applying omega- $k$  SAS processing shown in subfigure 5.4(c). Owing to the advantages of the least-squares method for this problem, the results on the BOSS Davis Point data set are generated using this method only.

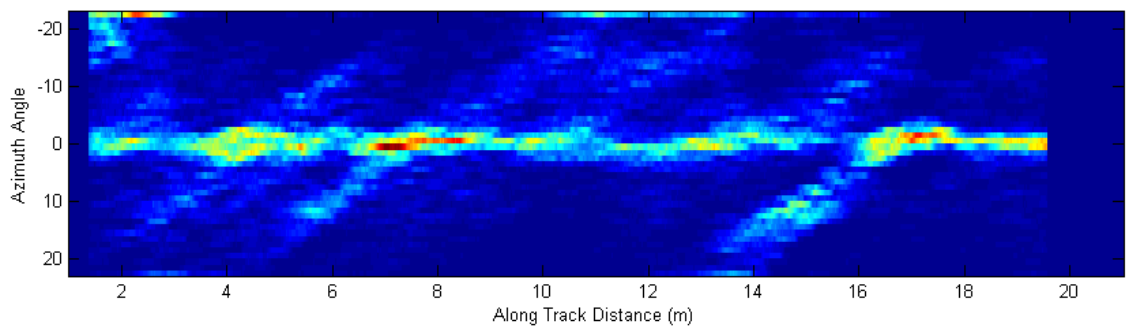
#### 5.4 Localization of Targets in Davis Point BOSS Data Set

Figures 5.5, 5.6, and 5.7 illustrate the results of applying the least-squares approach to several sequences from the Davis Point BOSS data, namely runs T4, T10, and T3. T4 is an iron cylinder, T3 is a bomb-shaped target, and T10 is a bomb-shaped marker. The subarray length was set to  $M = 10$  by using every other element on the 20-element hydrophone arrays on the two wings of the UUV-mounted BOSS system. Frequency focusing was performed according to the method prescribed in Chapter 4 to effectively collapse the wideband data to a single narrowband problem at each ping. As a baseline, conventional delay-and-sum SAS images of the corresponding seafloor regions are provided to illustrate the location(s) of objects of interest in each data sequences.

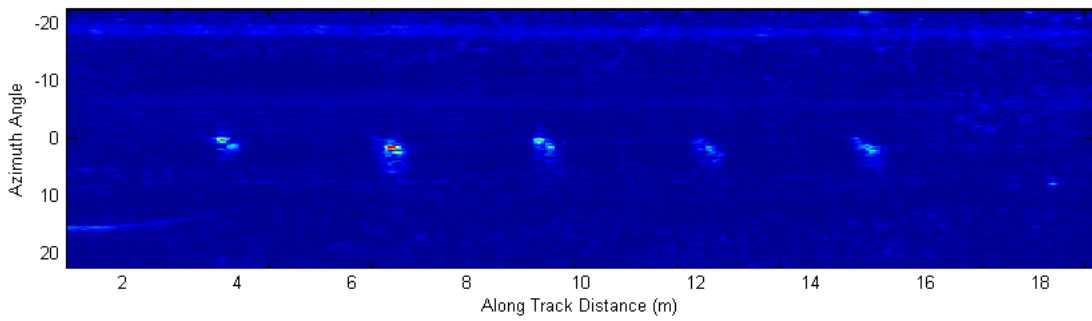
From Figures 5.5, 5.6, and 5.7, it is evident that the least-squares solution approach provides images portraying target location with fair success. However, in contrast to the PondEx10 results of Figures 5.3(a) and 5.4(a) which provide exceptional localization capability, the Davis Point BOSS results exhibit somewhat more spurious results. For example, the image of Figure 5.6 highlights the position of object T10 as a dark red region, but also contains highlighted areas that do not correspond to the position of any target object. These characteristics may be attributed to the non-ideal seafloor conditions, i.e. clutter, roughness, etc, of the Davis Point search region, as well as the non-uniform motion of the UUV-mounted BOSS system. However, despite the presence of these effects, the least-squares based solution produces SAS-like images which are representative of target location and demonstrates the usefulness of the proposed method for the detection and localization of targets in real sonar data.



(a) Angle estimation using least-squares.



(b) Angle estimation using OMP.



(c) Localization using  $\omega$ - $k$  SAS processing.

**Figure 5.4:** Target localization for PondEx10 run 191.

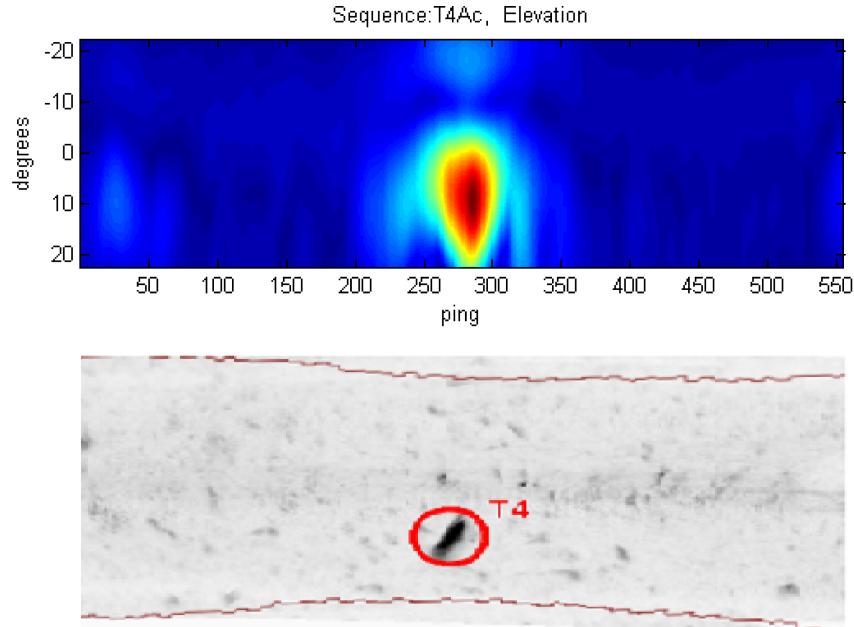


**Figure 5.5:** Azimuth angle estimation for BOSS Davis Point run T4. Top: angle estimation using least-squares approximation. Bottom: conventional delay-and-sum SAS image.

## 5.5 Conclusions

In Chapter 4, simulations were provided to validate the sparse representation problem formulation and benchmark two sparse solutions methods considered in this research. In this work, we examined a greedy algorithm (orthogonal matching pursuit (OMP)) and a convex relaxation technique (least-squares approximation). The simulations of Section 4.3.4 demonstrated that the OMP method is highly susceptible to noise, but provides excellent reconstruction under low noise levels with even a fairly short sensor array length. The least-squares approximation, on the other hand, is fairly robust to noise, but is impacted more dramatically by the length of the sensor subarray used. This is a rather intuitive result since it was shown in 2.5 that relaxing the sparse estimation problem to the  $\ell_2$ -norm approximation requires that the dictionary exhibit adequate mutual coherence. In the case of array signal processing, mutual coherence increases as the number of sensors in the array increases.

These simulation results were further confirmed by applying the sparse representation-based detection and localization method to two sonar data sets. The results of applying

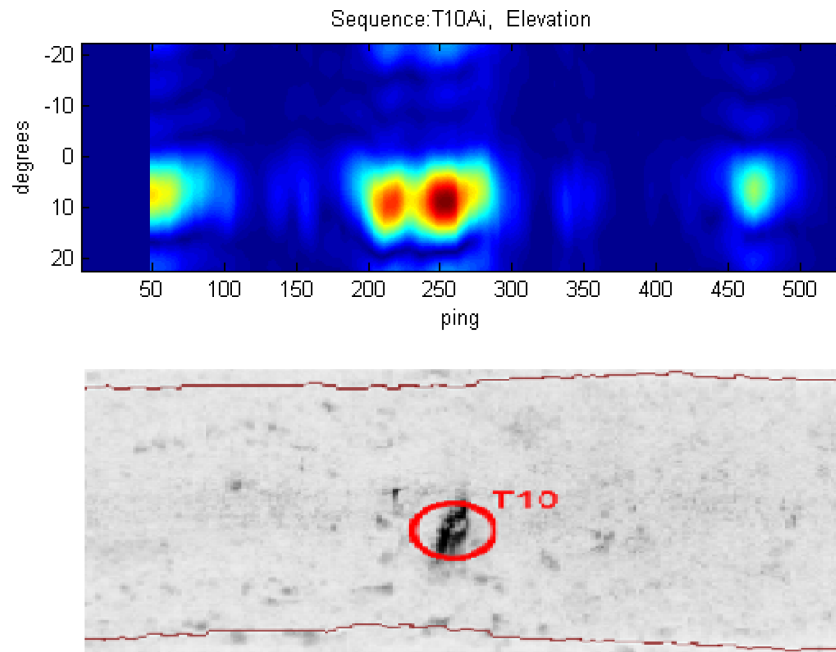


**Figure 5.6:** Azimuth angle estimation for BOSS Davis Point run T10. Top: angle estimation using least-squares approximation. Bottom: conventional delay-and-sum SAS image.

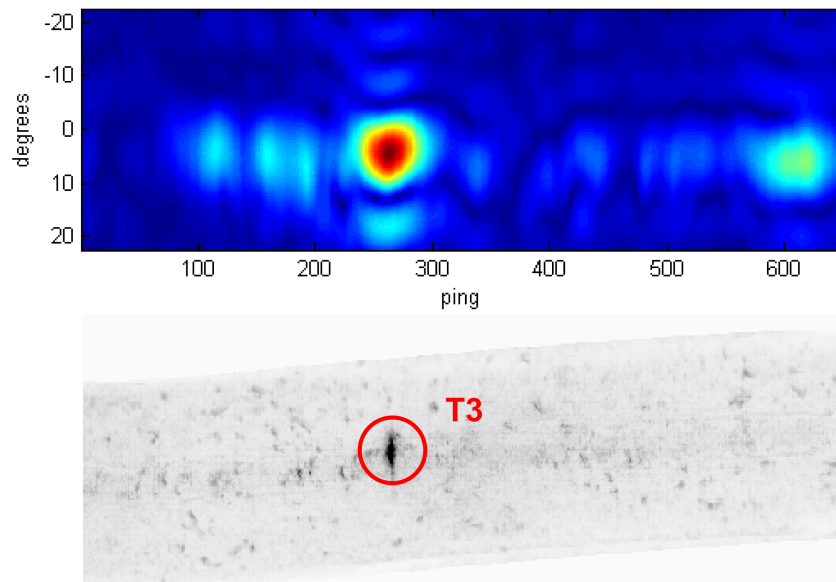


**Figure 5.7:** Azimuth angle estimation for BOSS Davis Point run T3. Top: angle estimation using least-squares approximation. Bottom: conventional delay-and-sum SAS image.

this new underwater target detection and localization algorithm to real sonar data are presented in Sections 5.3 and 5.4. The least-squares and OMP algorithms were applied to the PondEx10 data set using the same setup adopted during the simulations. For both solution methods, the sensor array length was kept the same. It was observed that the greedy OMP method is generally susceptible to the effects of noise and is likely impacted by the fact that the sources present are distributed in nature (i.e. the distribution in energy is not truly sparse as is assumed in the problem formulation). Conversely, for a sensor array of the same length the least-squares approximation was able to produce a good representation of target location. The BOSS Davis Point data set was also processed using the least-squares approach yielding SAS-like images representative of the locations of objects on the seafloor, and these results were contrasted with SAS images generated using a conventional delay-and-sum beamforming approach. This comparison indicated that the sparse representation-based method developed in Chapter 4 was able to produce images allowing for target localization, despite the effects of non-ideal seafloor conditions and non-uniform UUV-motion present in the Davis Point data.

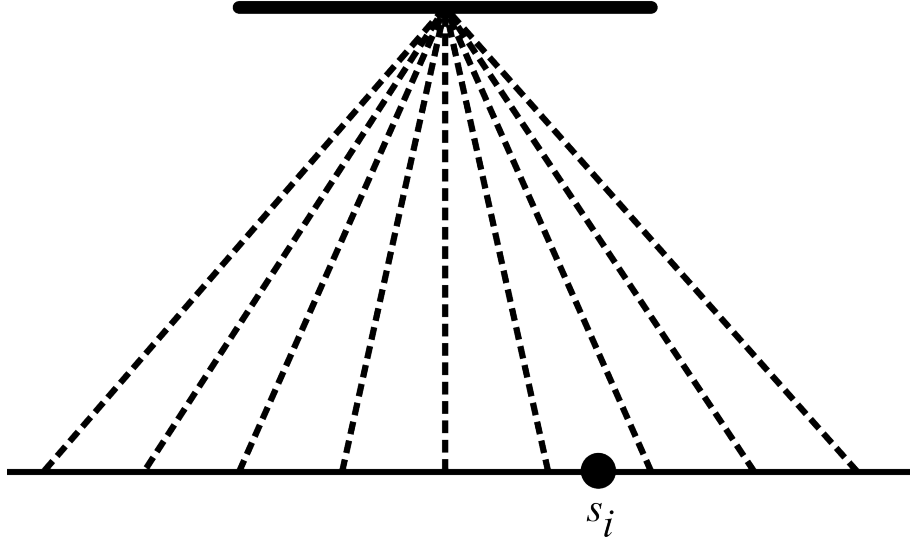
## CHAPTER 6

### BASIS MISMATCH INHERENT TO SONAR ARRAY PROCESSING

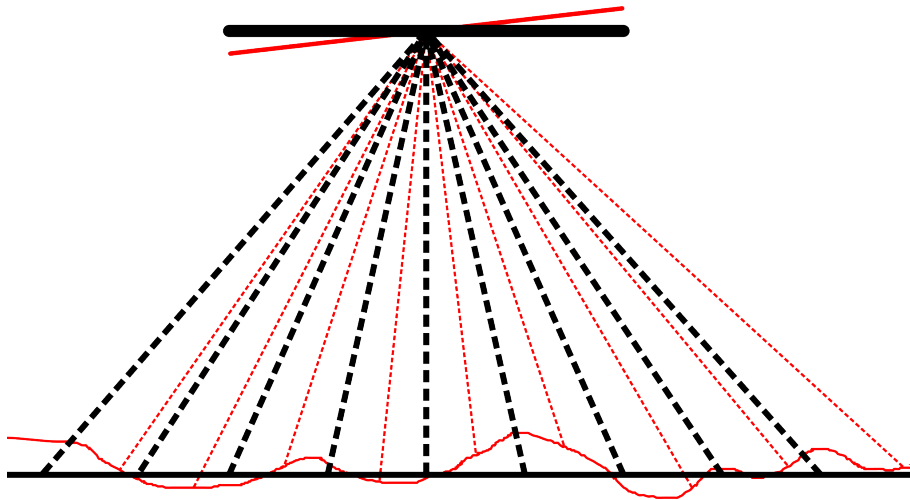
#### 6.1 Introduction

Sparse representation-based source localization methods suffer from many of the same limitations as traditional sonar processing techniques, such as sensitivity to the effects of sonar platform motion and other sources of phase error. In the context of sparse solution estimation, these types of uncertainty generally contribute to the degradation of the sparse estimation in two ways. The first type of error in estimation, which may proliferate from modeling errors or measurement uncertainty, arises when sources present in the array's field of view do not lie exactly on the defined discrete search grid. This is illustrated in Figure 6.1(a). In this case, the defined basis cannot adequately characterize the distribution of energy that is present in the search region, and sparse signal reconstruction using this non-ideal basis leads to degraded detection and localization results. The second type of estimation error may occur due to platform instability, errors in placement or calibration of sensors, and non-ideal seafloor conditions, among other ambiguities. From the perspective of sparse representation these types of uncertainty essentially manifest themselves as a discrepancy between the assumed sensor array manifold (which is used to construct the overcomplete basis) and the actual array manifold. This concept is illustrated in Figure 6.1(b). Essentially, platform instability or ambiguity of sensor position correspond to a scenario where the defined search grid does not represent the actual position of the sensor elements.

In the case of sonar array processing, both of these types of basis mismatch are often present, and the compound effects of these leads to diminished target localization ability. Without compensating for these types of errors, sparse representation-based angle of arrival estimation offers little or no advantage over the existing methods for detection of underwater objects. In this research the basis mismatch algorithm developed in [31], namely weighted-structured sparse total least-squares was evaluated for use in detection and localization of



(a) Source position is not captured by the defined search grid. Reconstruction using this non-ideal basis cannot estimate true target position.



(b) The defined search grid does not reflect the true platform orientation and neglects the effects of non-ideal seafloor conditions and other sources of error.

**Figure 6.1:** The effects of platform instability and other uncertainties on dictionary construction and sparse representation target localization.

underwater targets in sonar array data. This algorithm was applied to several sequences from the Davis Point data set, which exhibits the types of uncertainties that present challenges for the direct application of sparse representation-based angle of arrival estimation.

The motion compensation method implemented in this research is inspired from the work of [31]. This approach is motivated by past results showing that for the non-sparse overdetermined linear systems problem, the framework of total least-squares (TLS) provides a systematic approach to reconstructing solution vectors in the presence of perturbations of either the data vector or the dictionary matrix. TLS methods, however, cannot yield consistent approximations in the case of underdetermined systems, nor do they account for sparsity of the unknown solution vector. Therefore, the work of [31] focuses on extending the concepts of the TLS framework for sparse, underdetermined, perturbed linear models through what the authors have dubbed the sparse total least-squares (S-TLS) framework. Further, [31] describes that when the perturbations in the dictionary or the measurement vector exhibit a particular known structure, the general S-TLS problem may be reformulated to take advantage of the prior knowledge of perturbation. This algorithm, called weighted-structured S-TLS (WSS-TLS) subsumes the S-TLS algorithm for the case where the perturbation behavior is known to adhere to a specific structure, and ultimately allows for the recovery of provably convergent solutions using efficient sub-optimum solvers. The results of [31] demonstrate that gridding-based compressive sensing applications lend themselves naturally to the WSS-TLS problem formulation. Several practical simulations are provided in [31] to illustrate the merits of the S-TLS approach, including an angle-of-arrival demonstration which uses the WSS-TLS formulation.

The remainder of this chapter is organized as follows. In Section 6.2, the WSS-TLS approach developed in [31] is presented. In Section 6.3, this approach is demonstrated on several sequences from the the BOSS Davis Point data set, which is inherently prone to platform motion and other sources of error and uncertainty. Finally, conclusions are made in Section 6.4.

## 6.2 Sparsity Cognizant Total Least-Squares

Consider the underdetermined linear system of equations,  $\mathbf{Ax} = \mathbf{b}$ , where the unknown  $N \times 1$  vector  $\mathbf{x}$  is to be recovered from the given  $M \times 1$  data vector  $\mathbf{b}$ , and the  $M \times N$  matrix  $\mathbf{A}$ . If the unknown vector is sparse, sparse representation theory ensures recovery of  $\mathbf{x}$  even when  $M \ll N$  and the available  $\mathbf{b}$  is perturbed [47]. Specifically, the basis pursuit scheme [41] accounts for such perturbations by incorporating a sparsity-tuning parameter,  $\lambda$ . The basis pursuit sparse solvers can be equivalently written in the form of the least-squares criterion regularized by the  $\ell_1$ -norm, as

$$\begin{aligned} \{\hat{\mathbf{x}}, \hat{\mathbf{e}}\}_{BP} &:= \arg \min_{\mathbf{x}, \mathbf{e}} \|\mathbf{e}\|_2^2 + \lambda \|\mathbf{x}\|_1 \\ \text{s.t. } &\mathbf{b} + \mathbf{e} = \mathbf{Ax} \end{aligned} \tag{6.1}$$

where  $\mathbf{e}$  indicates the perturbation of  $\mathbf{b}$ .

In the context of sparse representation, perturbations can emerge due to disturbances in the measurement vector,  $\mathbf{b}$ , mismatch in the adopted dictionary,  $\mathbf{A}$ , or both [31]. The basis pursuit approach of (6.1) accounts for the former, but neglects the latter, i.e. it does not allow for the presence of dictionary mismatch. For the case of non-sparse overdetermined systems of equations, the total least-squares (TLS) framework provides a systematic approach for reconstructing solutions in the presence of either or both types of perturbation. TLS estimates are given by

$$\begin{aligned} \{\hat{\mathbf{x}}, \hat{\mathbf{E}}, \hat{\mathbf{e}}\}_{TLS} &:= \arg \min_{\mathbf{x}, \mathbf{E}, \mathbf{e}} \|\mathbf{[E e]}\|_F^2 \\ \text{s.t. } &\mathbf{y} + \mathbf{e} = (\mathbf{A} + \mathbf{E})\mathbf{x} \end{aligned} \tag{6.2}$$

where  $\mathbf{e}$  again denotes the perturbation of the measurement vector,  $\mathbf{E}$  indicates the error term associated with the basis, and  $\|\cdot\|_F^2$  denotes the Frobenius norm, which for an  $M \times N$  matrix,  $\mathbf{Z}$ , is defined as the square root of the sum of the absolute squares of its elements, i.e.  $\|\mathbf{Z}\|_F^2 = \sum_{i,j} |z_{ij}|^2$ .

Motivated by the TLS result for non-sparse overdetermined systems, the work in [31] develops a sparsity-cognizant TLS method (S-TLS) which provides a means of handling perturbed, underdetermined systems with unknown sparse solutions. To allow for perturbations in the measurement vector and dictionary mismatch while exploiting sparsity, the S-TLS approach amounts to finding

$$\begin{aligned} \{\hat{\mathbf{x}}, \hat{\mathbf{E}}, \hat{\mathbf{e}}\}_{S-TLS} &:= \arg \min_{\mathbf{x}, \mathbf{e}, \mathbf{E}} \|\mathbf{E}\mathbf{e}\|_F^2 + \lambda \|\mathbf{x}\|_1 \\ s.t. \quad \mathbf{b} + \mathbf{e} &= (\mathbf{A} + \mathbf{E})\mathbf{x} \end{aligned} \quad (6.3)$$

where  $\lambda > 0$  is a sparsity-tuning constant and  $\mathbf{e}$  and  $\mathbf{E}$  are defined as previously. Similarly to basis pursuit, the S-TLS estimates in (6.3) are universal, meaning that perturbations can be random or deterministic, and with or without a priori known structure. However, in contrast to the basis pursuit expression in (6.1), the S-TLS constraint (6.3) considers both  $\mathbf{b}$  and  $\mathbf{A}$  [31].

In [31], the constrained S-TLS formulation in (6.3) is shown to be equivalent to two unconstrained non-convex optimization problems. The first involves the sparse solution vector,  $\mathbf{x}$ , and the dictionary error term,  $\mathbf{E}$ ,

$$\{\hat{\mathbf{x}}, \hat{\mathbf{E}}\}_{S-TLS} = \arg \min_{\mathbf{x}, \mathbf{E}} [\|\mathbf{b} - (\mathbf{A} + \mathbf{E})\mathbf{x}\|_2^2 + \|\mathbf{E}\|_F^2 + \lambda \|\mathbf{x}\|_1] \quad (6.4)$$

and the second involves only the vector  $\mathbf{x}$ .

$$\hat{\mathbf{x}}_{S-TLS} := \arg \min_{\mathbf{x}} \frac{\|\mathbf{b} - \mathbf{A}\mathbf{x}\|_2^2}{1 + \|\mathbf{x}\|_2^2} + \lambda \|\mathbf{x}\|_1 \quad (6.5)$$

Supporting derivations and proofs are provided in [31]. Based on the problem formulation of (6.4) and (6.5), several solution methods for the S-TLS problem are examined, including a bisection-based algorithm, an alternating descent method, and a coordinate descent method.

Generally, each of these solvers iterates over (6.4) and (6.5) to dynamically update the estimated basis matrix and the corresponding sparse solution vector.

Working from the derivations of the S-TLS method, [31] demonstrates that the performance of the sparsity cognizant total least-squares framework may be improved by exploiting prior knowledge of the structure of the measurement and basis perturbations,  $\mathbf{e}$  and  $\mathbf{E}$ . Hence, the authors broaden the scope of S-TLS by examining weighted and structured error terms. It is noted therein that some applications, particularly gridding-based problems, naturally motivate such an extension of the S-TLS framework based on structured error terms. In the work of [31], structure is defined as follows

**Definition 1** *The  $M \times (N + 1)$  data matrix  $[\mathbf{A} \ \mathbf{b}]$  has a structure,  $\mathbf{S}(p)$ , characterized by an  $N_p \times 1$  parameter vector  $\mathbf{p}$ , if and only if there is a mapping such that  $\mathbf{p} \in \mathbb{R}^{N_p} \rightarrow [\mathbf{A} \ \mathbf{b}] := \mathbf{S}(\mathbf{p}) \in \mathbb{R}^{M \times (N+1)}$ .*

For problems where the error terms  $\mathbf{e}$  and  $\mathbf{E}$  are assumed to adhere to Definition 1, the S-TLS criterion of (6.3) may be recast in terms of the parameter vector,  $\mathbf{p}$ , and its associated perturbation vector denoted by  $\epsilon \in \mathbb{R}^{N_p}$ . The Frobenius norm in the cost function of (6.3) is mapped to the  $\ell_2$ -norm of  $\epsilon$ . To allow for weighting the perturbation vector using a symmetric positive definite matrix,  $\mathbf{W} \in \mathbb{R}^{N_p \times N_p}$ , the weighted counterpart of  $\|[\mathbf{E} \ \mathbf{e}]\|_2^F$  in (6.3) becomes  $\epsilon^T \mathbf{W} \epsilon$ . The structure definition of Definition 1 implies a perturbed matrix of the form  $\mathbf{S}(\mathbf{p} + \epsilon) = [\mathbf{A} + \mathbf{E} \ \mathbf{b} + \mathbf{e}]$ , hence the constraint of (6.3) is rewritten as  $[\mathbf{A} + \mathbf{E} \ \mathbf{b} + \mathbf{e}][\mathbf{x}^T, -1]^T = \mathbf{0}$  or correspondingly,  $\mathbf{S}(\mathbf{p} + \epsilon)[\mathbf{x}^T, -1]^T = \mathbf{0}$ . Combining these relationships leads to the weighted and structured (WS)S-TLS version of (6.3)

$$\begin{aligned} \{\hat{\mathbf{x}}, \hat{\epsilon}\}_{WSS-TLS} &:= \arg \min_{\mathbf{x}, \epsilon} \epsilon^T \mathbf{W} \epsilon + \lambda \|\mathbf{x}\|_1 \\ s.t. \quad &\mathbf{S}(\mathbf{p} + \epsilon) [\mathbf{x}^T, -1]^T = \mathbf{0} \end{aligned} \tag{6.6}$$

With the WSS-TLS problem formulation in mind, the goal of [31] becomes to develop an efficient algorithm to solve it, which is challenging because this problem is generally

non-convex. To render this problem tractable, a specific subset of structure mappings is considered which helps to simplify the WSS-TLS problem. To achieve this simplification, two constraints are imposed on the perturbation structure, namely they must be affine (i.e. linear) and separable. These conditions are imposed on the structure defined in Definition 1 as follows [31]

The structure mapping,  $\mathbf{S}(\mathbf{p})$ , in Definition 1 is separable, meaning that with  $\mathbf{p} = [(\mathbf{p}^A)^T (\mathbf{p}^b)^T]^T$ , where  $\mathbf{p}^A \in \mathbb{R}^{N_A}$  and  $\mathbf{p}^b \in \mathbb{R}^{N_b}$ , it holds that  $\mathbf{S}(\mathbf{p}) := [\mathbf{A} \ \mathbf{b}](\mathbf{p}) = [\mathbf{A}(\mathbf{p}^A) \ \mathbf{b}(\mathbf{p}^b)]$ . In addition, the separable structure mapping is linear (more precisely affine), if and only if the  $\mathbf{S}(\mathbf{p})$  matrix is composed of known structural elements, namely “matrix atoms”  $\mathbf{S}_0$ ,  $\{\mathbf{S}_k^A\}_{k=1}^{N_A}$  and “vector atoms”  $\{\mathbf{s}_k^b\}_{k=1}^{N_b}$  so that

$$\mathbf{S}(\mathbf{p}) = \mathbf{S}_0 + \left[ \sum_{k=1}^{N_A} p_k^A \mathbf{S}_k^A \quad \sum_{k=1}^{N_b} p_k^b \mathbf{s}_k^b \right] \quad (6.7)$$

where  $p_k^A(p_k^b)$  denotes the  $k$ th entry of  $\mathbf{p}^A(\mathbf{p}^b)$ .

For notational simplicity, the respective collections of matrix atoms and vectors atoms are given as

$$\mathbf{S}^A := [\mathbf{S}_1^A \dots \mathbf{S}_{N_A}^A] \quad \text{and} \quad \mathbf{S}^b := [\mathbf{s}_1^b \dots \mathbf{s}_{N_b}^b] \quad (6.8)$$

The linearity condition allows one to write  $\mathbf{S}(\mathbf{p} + \epsilon) = \mathbf{S}(\mathbf{p}) + \mathbf{S}(\epsilon)$  which may in turn be used to rewrite the constraint of (6.6) as  $\mathbf{S}(\epsilon) [\mathbf{x}^T, -1]^T = -\mathbf{S}(\mathbf{p}) [\mathbf{s}^T, -1]^T = \mathbf{b} - \mathbf{A}\mathbf{x}$ . The separability constraint implies that

$$\begin{aligned} \mathbf{S}(\epsilon) [\mathbf{x}^T, -1]^T &= \left[ \sum_{k=1}^{N_A} \epsilon_k^A \mathbf{S}_k^A \quad \sum_{k=1}^{N_b} \epsilon_k^b \mathbf{s}_k^b \right] [\mathbf{x}^T, -1]^T \\ &= \mathbf{S}^A (\mathbf{I} \otimes \mathbf{x}) \epsilon^A - \mathbf{S}^b \epsilon^b \end{aligned} \quad (6.9)$$

where the notation of (6.8) and the definition  $\epsilon = [(\epsilon^A)^T (\epsilon^b)^T]^T$  are used. The significance of (6.9) lies in the fact that the error terms  $\epsilon^A$  and  $\epsilon^b$  are effectively decoupled by imposing an affine and separable structure requirement. This separability of perturbations in  $\mathbf{A}$  and

$\mathbf{b}$  ultimately allows for the WSS-TLS problem to be rewritten as

$$\begin{aligned} \min_{\mathbf{x}, \epsilon^A, \epsilon^b} & \begin{bmatrix} \epsilon^A \\ \epsilon^b \end{bmatrix}^T \mathbf{W} \begin{bmatrix} \epsilon^A \\ \epsilon^b \end{bmatrix} + \lambda \|\mathbf{x}\|_1 \\ \text{s.t.} & [\mathbf{S}^A(\mathbf{I} \otimes \mathbf{x}) - \mathbf{S}^b] \begin{bmatrix} \epsilon^A \\ \epsilon^b \end{bmatrix} = \mathbf{b} - \mathbf{A}\mathbf{x} \end{aligned} \quad (6.10)$$

or more succinctly as

$$\begin{aligned} \min_{\mathbf{x}, \epsilon} & \epsilon^T \mathbf{W} \epsilon + \lambda \|\mathbf{x}\|_1 \\ \text{s.t.} & \mathbf{G}(\mathbf{x})\epsilon = \mathbf{r}(\mathbf{x}) \end{aligned} \quad (6.11)$$

where  $\mathbf{G}(\mathbf{x}) := [\mathbf{S}^A(\mathbf{I} \otimes \mathbf{x})\mathbf{S}^b]$  and  $\mathbf{r}(\mathbf{x}) := \mathbf{b} - \mathbf{A}\mathbf{x}$ .

It is further asserted in [31] that, like the S-TLS formulation, the constrained WSS-TLS form of (6.11) is equivalent to two unconstrained non-convex optimization problems, one of which involves the sparse solution,  $\mathbf{x}$ , and the dictionary perturbation,  $\epsilon^A$ , and one which only involves  $\mathbf{x}$ . These two optimization problems for the special case of affine and separable perturbation structure are expressed as

$$\{\hat{\mathbf{x}}, \hat{\epsilon}^A\}_{wsstls} = \arg \min_{\mathbf{x}, \epsilon^A} \begin{bmatrix} \epsilon^A \\ \mathbf{F} \end{bmatrix}^T \mathbf{W} \begin{bmatrix} \epsilon^A \\ \mathbf{F} \end{bmatrix} \quad \text{and} \quad \mathbf{F} = (\mathbf{S}^b)^\dagger [\mathbf{S}^A(\mathbf{I} \otimes \mathbf{x})\epsilon^A - \mathbf{r}(\mathbf{x})] \quad (6.12)$$

$$\hat{\mathbf{x}}_{wsstls} = \arg \min_{\mathbf{x}} \{\mathbf{r}^T(\mathbf{x}) [\mathbf{G}(\mathbf{x})\mathbf{W}^{-1}\mathbf{G}^T(\mathbf{x})]^\dagger \mathbf{r}(\mathbf{x}) + \lambda \|\mathbf{x}\|_1\} \quad (6.13)$$

Complete derivations and proofs are provided in [31], as well as verification of the existence of a convergent solution. One important characteristic of (6.12) and (6.13) is that the variables of interest are the sparse solution,  $\mathbf{x}$  and the perturbation of the dictionary,  $\epsilon^A$ . Therefore at each iteration over this set of equations, the dictionary error term is computed and the sparse solution estimate is updated accordingly.

In [31], a block coordinate descent (CD) solver is adopted which alternatively optimizes over  $\epsilon^A$  and  $\mathbf{x}$  by iteratively updating and solving (6.12) and (6.13). The steps of this CD solution approach are outlined in [31] as well as in [33]. Several numerical examples are provided in [31] illustrating the merits of the WSS-TLS algorithm for several classes of problems.

### 6.3 Localization of Targets in Davis Point BOSS Data Set

The problem of target localization may be framed as a WSS-TLS problem by considering a perturbed version of (4.17), i.e.

$$\mathbf{s}_{xy} + \mathbf{e} = (\mathbf{A}_0 + \mathbf{E})\Gamma_0 \quad (6.14)$$

where  $\mathbf{e}$  and  $\mathbf{E}$  denote measurement perturbation and dictionary mismatch, respectively. As was previously discussed, for the specific application of sonar processing, variabilities such as measurement error and platform instability manifest themselves as contributions to these error terms,  $\mathbf{e}$  and  $\mathbf{E}$ . By exploiting the structural constraints described in the previous section, the optimization problem that arises from (6.14) may be posed in the form of (6.12) and (6.13) and then solved using a coordinate descent algorithm as proposed in [31].

In this work, the WSS-TLS approach was evaluated on several sequences of the Davis Point BOSS data. Results are shown in Figures 6.2, 6.3, and 6.4 for Davis Point sequences T4, T10, and T3, respectively. T4 is an iron cylinder, T3 is a bomb-shaped target, and T10 is a bomb-shaped marker. The subarray length was set to  $M = 10$  by using every other element on the 20-element hydrophone arrays on the two wings of the UUV-mounted BOSS system. Frequency focusing was performed in the manner prescribed in Chapter 4 to effectively collapse the wideband data into a single narrowband problem at each ping. Figures 6.2, 6.3 and 6.4 compare the results of implementing the WSS-TLS approach of [31] with those generated using the method derived in Chapter 4 and the delay-and-sum beamformer [52,53].

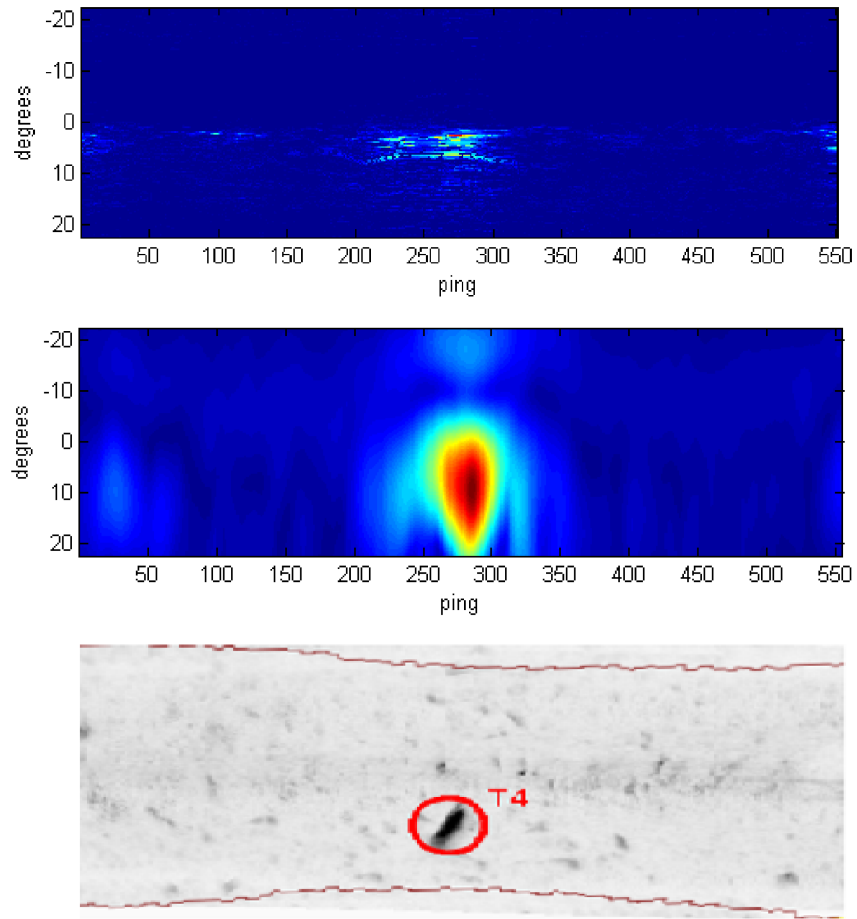


**Figure 6.2:** Azimuth angle estimation for BOSS Davis Point run T4. Top: angle estimation using WSS-TLS framework and coordinate descent solver. Middle: angle estimation using least-squares approximation. Bottom: conventional delay-and-sum SAS image.

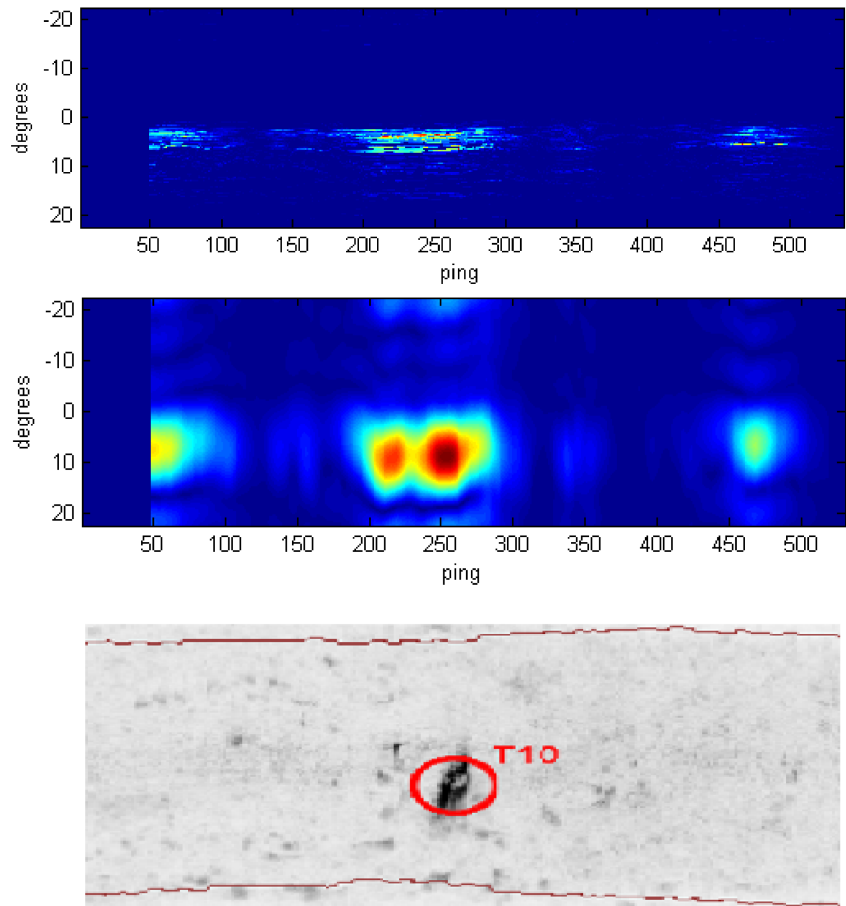


**Figure 6.3:** Azimuth angle estimation for BOSS Davis Point run T10. Top: angle estimation using WSS-TLS framework and coordinate descent solver. Middle: angle estimation using least-squares approximation. Bottom: conventional delay-and-sum SAS image.

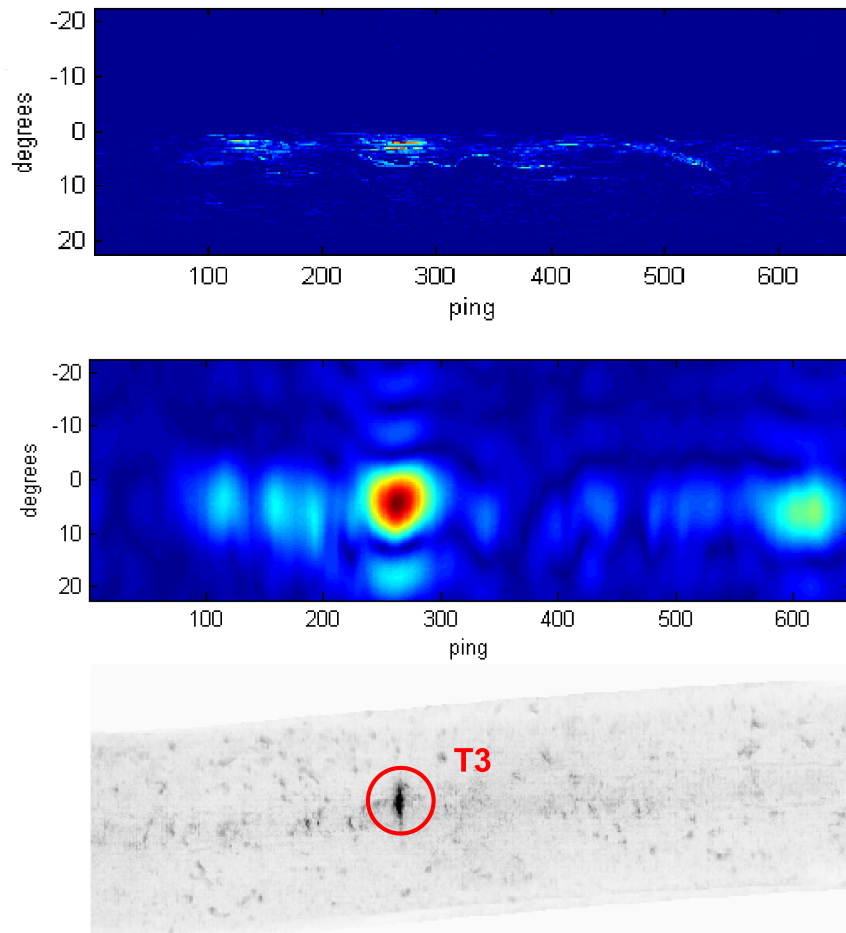


**Figure 6.4:** Azimuth angle estimation for BOSS Davis Point run T3. Top: angle estimation using WSS-TLS framework and coordinate descent solver. Middle: angle estimation using least-squares approximation. Bottom: conventional delay-and-sum SAS image.

While the results obtained here are interesting, it is apparent that for the current application a solution method which enforces strict sparsity is perhaps not ideal. Object T3 in particular is obscured in these results and in all three examples there is energy present in regions of the images that don't correspond to target positions. The poor image quality of these results may be attributed at least in part to the fact that the targets under consideration are not point sources, as is assumed in the derivations of Chapter 4, therefore a strictly sparse solution provides a poor estimate of the distribution of energy, even when methods such as WSS-TLS are employed to estimate an optimum basis matrix.

## 6.4 Conclusions

Platform motion and other non-ideal effects present in sonar data present a challenge for source localization and detection using sparse representation-based methods. Subarray motion and other measurement uncertainties manifest themselves as a discrepancy between the defined search grid and the physical search scene, resulting in degraded imaging capability. Several algorithms have been developed to alleviate the impact of these degrading effects [31,32]. In this chapter, one such algorithm was evaluated and demonstrated on several sequences of the Davis Point BOSS data, which is especially sensitive to the mismatch problem due to the nature of the UUV-mounted data acquisition system. The algorithm examined here, known as weighted-structured sparse total least-squares (WSS-TLS) [32] extends the total least-squares framework for the specific application of sparse representation problems and considers the special case of perturbations with specific known structures. However, applying this motion compensation technique to the Davis Point BOSS sonar data highlighted the fact that a solution approach that enforces a strictly sparse solution is perhaps not ideal for localizing underwater targets in sonar data. In this specific application, a strictly sparse representation is not necessarily appropriate, because the physical sources are distributed in nature and do not lie on individual discrete grid points as the point source model suggests. The sparse representation-based detection and localization approach arises

from the assumption that the signal energy may be characterized as emanating from a relatively few distinct points in a discrete grid. This point source assumption does not fit the data under consideration, and therefore sparse representation of the data is inherently erroneous. Algorithms such as that in [31, 32] are intended to find an overcomplete basis which allows for accurate sparse representation of the measurement vector. In our case, the data cannot be accurately represented as a strictly sparse vector, so the improvement offered by dictionary learning approaches like [31, 32] is limited.

## CHAPTER 7

### CONCLUSIONS AND SUGGESTIONS FOR FUTURE WORK

#### 7.1 Summary and Conclusions

This work focused on the development and implementation of an algorithm for the detection and localization of underwater objects using wideband sonar. Specifically, a new near-field target localization method was developed which leverages concepts from the sparse representation framework. Sparse reconstruction has previously been implemented for the purpose of target bearing estimation, however existing works have failed to address the specific challenges presented by sonar data processing. To extend the existing sparse representation-based angle of arrival work, three specific contributions were made through this research.

First, a *near-field* array signal model was developed by examining the relationship between signals impinging on two uniform linear sensor arrays, resulting in an elegant transformation of the near-field localization problem into a problem independent of the target range. Exploiting this relationship and examining the cross-covariance of the signals between corresponding elements in the two linear subarrays led to the formulation of an underdetermined linear systems problem, which are generally considered intractable. However, with the added constraint that the number of sources present resulted in a sparse distribution of energy, this near-field localization problem was then tackled using tools from the sparse representation framework.

Secondly, a frequency focusing approach was developed in order to convert the problem of *wideband* sonar processing into a narrowband problem. In the focusing approach used in this work, a single focused cross-covariance matrix was formed for the wideband data prior to estimation of the target bearing, which allowed for only a single angle of arrival estimation to be performed at each ping using the sparse solution finding methods.

Lastly, strategies were examined for improving the robustness of the sparse recovery method to the effects of sonar platform motion and other measurement uncertainties. From

the perspective of sparse representation-based localization, platform motion and other non-ideal effects manifest themselves as a mismatch between the assumed array manifold (which is used to construct the overcomplete dictionary from which a sparse solution is sought) and the actual array manifold. A mismatch-compensating algorithm from [31] was investigated in this work. In [31], the true basis is treated as the combination of a known, fixed basis matrix with an unknown and variable error matrix, which must be estimated from the data. To attempt to alleviate the degrading effects of basis mismatch, a sparse total least-squares approach is adopted which takes advantage of the structured nature of the dictionary mismatch and measurement perturbations that occur in gridding-based sparse representation applications.

Details of the development and implementation of these methods are summarized in the following sections.

### 7.1.1 Detection and Localization Using Sparse Representation

This task focused on the development and implementation of an algorithm for the detection and localization of underwater objects using broadband sonar. Specifically, a new near-field target localization method was developed which leverages on concepts from the sparse representation framework. Sparse reconstruction has previously been implemented for the purpose of target bearing estimation, however existing works have failed to address the specific challenges presented by sonar data processing. To extend the existing sparse representation-based angle of arrival estimation for sonar data, two specific contributions were made through this research task. First, a *near-field* array signal model was developed which examined the relationship between signals impinging on two uniform linear sensor subarrays, resulting in an elegant transformation of the near field localization problem into a problem independent of the target range provided that the platform elevation is known a priori. Using this relationship, and examining the cross-covariance of the signals between corresponding elements in the two linear subarrays led to the formulation of an under-determined linear systems problem, which are generally considered intractable. However,

with the added constraint that the number of sources present results in a sparse distribution of energy, this near-field problem was then tackled using tools from the sparse representation framework. Second, the source localization method was extended to allow for the wideband nature of the sonar data. In this work, a frequency transformation was applied to transform each frequency (or frequency subband) present in the data to a single effective frequency using the focusing idea presented in [69]. In this manner, a computationally effective frequency focusing algorithm was derived which is a very simple and efficient extension of the narrowband source localization routine.

In Chapter 4, simulations were performed on synthetic data to validate the sparse representation problem formulation and compare two different sparse solution-finding methods namely the greedy algorithm using the orthogonal matching pursuit (OMP) and a convex relaxation technique using the least-squares approximation. These simulations demonstrated that the OMP method is highly susceptible to noise, but provides excellent reconstruction under low noise levels with even a fairly short sensor array length. The least-squares approximation, on the other hand, was found to be highly robust to noise, but was impacted more significantly by the length of the sensor subarray used. This is a rather intuitive result since it was shown that relaxing the sparse estimation problem to the  $\ell_2$ -norm approximation requires that the dictionary exhibit adequate mutual coherence. In the case of array signal processing, mutual coherence increases as the number of sensors in the array increases.

These simulation results were further confirmed by applying the sparse representation-based detection and localization method to two real sonar data sets in Chapter 5. The least-squares and OMP algorithms were applied to the PondEx10 data set using the same processing conditions used during simulation. For both sparse solution approaches, the sensor array length was kept the same and it was observed that the OMP method is sensitive to the effects of noisy data, whereas the least-squares approximation was able to produce a good representation of target location. The BOSS Davis Point data set was also processed using the least-squares approach yielding SAS-like images representative of locations of objects on

the seafloor, and these results were contrasted with the standard (delay-and-sum) SAS and SAS-like acoustic color images. These results show the capability of the proposed method for producing SAS-like images without incorporating any motion estimation or compensation. In comparing the images generated using OMP and the least-squares approach, it is evident that the least-squares approach is a more capable method for the problem in hand. This result arises at least in part due to the fact that the targets under consideration cannot be characterized as point sources, as is assumed in the model of Chapter 4. In keeping with the essence of the sparse representation framework, the OMP algorithm seeks the sparsest representation of the observation vector; the data under consideration here cannot be accurately represented as a sparse solution vector.

### 7.1.2 SAS-like Image Generation with Platform Motion

A serious downfall of the sparse representation-based target detection and localization method lies in the fact that the problem inherently requires defining a discrete overcomplete basis. Problems arise when either the discrete grid does not capture the positions of sources present, or when the defined search grid does not match the layout of the physical search region, i.e. the grid is defined by projecting an angle dictionary onto a presumed flat surface, but the true search region is uneven. This discrepancy between the assumed measurement environment and the physical environment manifests itself as a mismatch between the defined overcomplete basis and the true basis. The result is that the defined discrete grid can not accurately characterize the true source signals, and the localization results obtained using this non-ideal basis are degraded.

In Chapter 6, a sparsity cognizant total least-squares algorithm from [31] was evaluated for use in sparse representation-based sonar imaging. The algorithm developed in [31] is an extension of the total least-squares framework for use in sparse representation applications where dictionary gridding leads to structured behavior of the basis mismatch and measurement perturbation. The resulting problem formulation, called weighted-structured total least-squares (WSS-TLS) ultimately reduces the perturbed sparse representation problem to

a set of two unconstrained nonconvex optimization problems which may be solved efficiently using sub-optimum solvers. In the work of [31], a coordinate descent algorithm was used to solve the WSS-TLS problem. In this work, the WSS-TLS approach was applied to several sequences of the Davis Point BOSS data. Unfortunately, the WSS-TLS approach performed poorly as compared to least-squares algorithm. Comparing the images generated using the two methods, it is clear the least-squares approach provides better detection and localization of the target objects.

Similarly to the greedy OMP algorithm evaluated in Chapter 5, the coordinate descent solution for the WSS-TLS problem enforces  $k$ -sparsity, which does not characterize the physical nature of the sources under consideration, as was previously discussed. The general idea of algorithms such as the sparsity cognizant total least-squares approach in [31] is to construct an overcomplete basis matrix that characterizes the true measurement environment (in our case the array steering vectors) so as to allow for improved sparse representation of the measurement vector. In the sonar signal processing problem at hand, however, the distribution of energy is not strictly sparse and hence it is difficult to accomplish dictionary learning to improve the sparse representation, and in fact such an approach may be altogether unsuitable.

## 7.2 Future Work

Because target localization using the sparse representation framework is a relatively new research topic, this area offers many opportunities for new developments and improvements on existing work. This is especially true of the specific problem of SR-based sonar signal processing, which presents unique challenges to the implementation of sparse solution methods. Candidate research problems in this area include, but are not limited to:

- Expansion of the understanding of the fundamental relationships between sensor array geometry, the construction of angle of arrival dictionaries, and the convergence to a sparse angle of arrival estimate. That is, for a given array geometry, what angle range and angular resolution may be used to construct a dictionary which guarantees

a unique angle of arrival solution? Or conversely, if a localization application requires a particular angular resolution or angle search range, and one wishes to use a sparse representation localization approach, how must the sensor array be constructed? While the physical limitations of classical beamforming (resolution and beampattern as related to array geometry) are well understood, these relationships are not well-defined for the localization problem posed using the sparse representation framework. As was briefly presented in Chapter 2, sparse solution methods provide convergent solutions when the solution vector is sufficiently sparse and when the defined dictionary matrix meets certain basic requirements (i.e. mutual coherence / orthogonality of columns in the over-complete basis). As with traditional array processing methods, it is evident that the angle range and angular resolution are dictated by some relationship with the array geometry, (i.e. number of sensor elements per array, interelement spacing, and subarray separation in the case of symmetric subarray processing). However, from a sparse representation perspective, angle range and angular resolution also dictate the formation of the overcomplete dictionary and as such may be quantified in terms of measures such as mutual coherence and/or restricted isometry, which are fundamental measures of the guarantee of estimating a unique sparse solution vector. The existing work in the area of sparse representation target localization lacks fundamental definition of the relationship between array geometry and recovery of a unique sparse solution. It is also interesting to consider how these relationships may relate to the resolution and search range limitations of traditional array processing methods.

- Development of a sparse representation detection and localization method based on a distributed source model, rather than the point source model implemented in this work. The use of an alternative physical model may allow for improved characterization of the target objects of interest and thus improved detection capability. The detection method developed in Chapter 4 arises directly from the point source model used there, therefore it is natural to assume that starting from an alternative model

may lead to a problem that does not lend itself readily to the application of sparse solution methods. However, one possible strategy is to pose a distributed source localization problem from the perspective of ‘block-sparsity’ [72], i.e. sparse signals that exhibit non-zeros elements in clusters or blocks. Recovery of block-sparse solutions is a special subset of the sparse representation framework which has received a fair amount of attention [72, 73], [62] due to the fact that making explicit use of block-sparsity can yield better reconstruction properties than treating the signal as being sparse in the conventional sense. In addition to possible application to a distributed source localization problem, block-sparsity arises naturally in wideband signals, as well as in the multiple measurement vector (MMV) problem, which deals with the measurement of a set of vectors that share a joint sparsity pattern. Sonar array signal processing is an excellent candidate problem for the application of block-sparsity methods.

- Development of a target classification method based on the sparse representation framework. In the context of the specific problems examined in this work, one plausible approach is to take advantage of the wideband nature of the sonar returns under consideration. In the imaging algorithm developed in this work, wideband data from each sonar ping is ‘focused’ to a single effective frequency, and then coherent averaging of the cross-covariance matrix is performed across the full frequency spectrum to produce a single angle of arrival problem for a given ping. These single ping results are then combined sequentially to yield a ping versus angle of arrival image for each sonar data sequence. In this imaging approach, the information available at each distinct frequency is essentially lost during averaging. As an alternative strategy, each frequency band may be treated as a distinct sparse representation problem, and the frequency information available at each ping could be retained and potentially used to achieve target classification in addition to detection and localization. Such an approach yields results with dimension (ping  $\times$  angle  $\times$  frequency). Much like the work

of [7, 8] wherein classification is performed using the canonical correlation versus frequency relationship at each frequency band of each ping, one reasonable strategy for classifying target objects may be to analyze their angle of arrival versus frequency characteristics. The derivations in Section 4.4, which describe the manner in which wideband data was handled in this project, might provide a useful starting point for developing a classification system based on sparse angle of arrival estimates at each frequency sub-band.

- Investigation of the applicability of mismatch-compensated SR detection and localization to problems in other areas of signal processing, communications, radar, etc. Basis mismatch induced by array motion is an important consideration when processing sonar data. However basis mismatch may also be introduced by a variety of other sources of error, i.e. inexact sensor placement, which may be evident in other sensor array-based data acquisition and processing approaches. As such, fields such as radar or acoustic array processing may benefit to some degree from mismatch-compensating algorithms such as those explored in Chapter 6 of this work. Such studies would also allow for further characterization of the advantages and disadvantages of the methods proposed in this thesis with respect to specific target detection problems in various fields.

## REFERENCES

- [1] J. E. Thorner, "Approaches to sonar beamforming," *Proc. of IEEE Southern Tier Technical Conference*, pp. 69–78, April 1990.
- [2] C. A. Speirs, D. T. Highes, J. L. Mather, and A. R. Green, "Practical considerations of using adaptive beamforming with real sonar data," *Proc. of Seventh International Conference on Electronic Engineering in Oceanography*, pp. 120–127, June 1997.
- [3] J. Bourdelais, "An adaptive beamforming algorithm for broadband active sonar," *Proc. of IEEE International Conference on Acoustics, Speech and Signal Processing (ICASSP)*, 1998.
- [4] B. G. Ferguson and R. J. Wyber, "Generalized framework for real aperture, synthetic aperture, and tomographic sonar imaging," *IEEE Journal of Oceanic Engineering*, vol. 34, no. 3, pp. 225–238, July 2009.
- [5] B. L. Douglas and H. Lee, "Synthetic-aperture sonar imaging with a multiple-element receiver array," *Proc. of IEEE International Conference on Acoustics, Speech, and Signal Processing (ICASSP)*, vol. 5, pp. 445–448, April 1993.
- [6] M. P. Hayes and P. T. Gough, "Synthetic aperture sonar: a review of current status," *IEEE Journal of Oceanic Engineering*, vol. 34, no. 3, pp. 207–224, July 2009.
- [7] N. Wachowski and M. R. Azimi-Sadjadi, "A new synthetic aperture sonar processing method using coherence analysis," *IEEE Journal of Oceanic Engineering*, vol. 36, no. 4, pp. 665–678, October 2011.
- [8] N. Wachowski and M. R. Azimi-Sadjadi, "Buried underwater target classification using frequency subband coherence analysis," *Proc. of MTS/IEEE Oceans*, pp. 1–8, September 2008.

- [9] C. Yuan, M. R. Azimi-Sadjadi, J. Wilbur and G. J. Dobeck, "Underwater target detection using multichannel subband adaptive filtering and high-order correlation schemes," *IEEE Journal of Oceanic Engineering*, vol. 25, no. 1, pp. 192–205, January 2000.
- [10] S. Kim, B. Ku, W. Hong and H. Ko, "Performance comparison of target localization for active sonar systems," *IEEE Trans. on Aerospace and Electronic Systems*, vol. 44, no. 4, pp. 1371–1380, October 2008.
- [11] L. Bai, C. Peng and S. Biswas, "Association of DOA estimation from two ULAs," *IEEE Trans. on Instrumentation and Measurement*, vol. 57, no. 6, pp. 1094–1101, June 2008.
- [12] A. J. Weiss and B. Friedlander, "DOA and steering vector estimation using a partially calibrated array," *IEEE Trans. on Aerospace and Electronic Systems*, vol. 32, no. 3, pp. 1047–1057, July 1996.
- [13] T. Liu and J. M. Mendel, "Azimuth and elevation direction finding using arbitrary array geometries," *IEEE Trans. on Signal Processing*, vol. 46, no. 7, pp. 2061–2065, July 1998.
- [14] Q. Zhao, J. Wang and B. Wang, "2D DOA estimation for coherently distributed source," *Proc. of International Conference on Computer Design and Applications (ICCCA)*, vol. 4, pp. 366–369, June 2010.
- [15] N. Li, J. Gu, and P. Wei, "2-D DOA estimation via matrix partition and stacking technique," *EURASIP Journal of Advanced Signal Processing*, pp. 13–16, January 2009.
- [16] M. R. Azimi-Sadjadi and D. Yao and G. J. Dobeck, "Underwater target classification using wavelet packets and neural networks," *IEEE Trans. on Neural Networks*, vol. 11, no. 3, pp. 784–794, May 2000.
- [17] Z. Wang and P. Willett, "All-Purpose and Plug-In Power-Law Detectors for Transient Signals," *IEEE Trans. on Signal Processing*, vol. 49, no. 11, pp. 2454–2466, November 2001.

- [18] R. Heremans, M. Acheroy, and Y. Dupont, "Motion compensation on synthetic aperture sonar images, Ed. 3B-6," *IEEE Ultrasonics Symposium*, pp. 152–155, October 2006.
- [19] A. J. Poulsen, D. P. Eickstedt and J. P. Lanniello, "Bearing stabilization and tracking for an AUV with an acoustic line array," *Proc. of MTS/IEEE Oceans*, pp. 1–6, September 2006.
- [20] X. Wang and C. Sun and B. Liu and S. Su, "An improved motion error estimation algorithm for SAS using a displaced phase center antenna," *Proc. of 8th International Conference on Signal Processing*, vol. 4, 2006.
- [21] W. Liu, C. Zhang, and J. Liu, "Improved synthetic aperture sonar motion compensation combined DPCA with sub-aperture image correlation," *Journal of Electronics (China)*, vol. 26, pp. 191–197, 2009.
- [22] H. J. Callow, M.P. Hayes and P. T. Gough, "Autofocus of multi-band, shallow-water synthetic aperture sonar imagery using shear-averaging," *Proc. of IEEE International Geoscience and Remote Sensing Symposium (IGARSS)*, vol. 4, pp. 1601–1603, 2001.
- [23] D. Malioutov, M. Cetin, A. S. Willsky, "A sparse signal reconstruction perspective for source localization with sensor arrays," *IEEE Trans. on Signal Processing*, vol. 53, no. 8, pp. 3010–3022, August 2005.
- [24] I. F. Gorodnitsky and B. D. Rao, "Sparse signal reconstruction from limited data using FOCUSS: a re-weighted minimum norm algorithm," *IEEE Trans. on Signal Processing*, vol. 45, no. 3, pp. 600–616, March 1997.
- [25] Z. Wang and W. Wang, "Fast and adaptive method for SAR superresolution imaging based on point scattering model and optimal basis selection," *IEEE Trans. on Image Processing*, vol. 18, no. 7, pp. 1477–1486, July 2009.

- [26] J. Wang, Z. Huang, and Y. Zhou, "Direction-of-Arrival Estimation Based on Joint Sparsity," *Sensors*.
- [27] P. T. Boufounos, P. Smaragdis, and B. Raj, "Joint sparsity models for wideband array processing," *Proc. of Society of Photo-Optical Instrumentation Engineers (SPIE)*, 2011.
- [28] Z. Tang, G. Blacchiere, and G. Leus, "Aliasing-free wideband beamforming using sparse signal representation," *IEEE Trans. on Signal Processing*, vol. 59, no. 7, pp. 3464–3469, July 2011.
- [29] H. Zhang, N. Feng, and L. Ma, "A CS based high resolution DOA estimation method for sonar targets," *International Journal of Advancements in Computing Technology (IJACT)*, vol. 3, no. 9, pp. 181–187, October 2011.
- [30] Y. Zhao, A. Dinstel, M. R. Azimi-Sadjadi, and N. Wachowski, "Localization of near-field sources in sonar data using the sparse representation framework," *Proc. of MTS/IEEE Oceans*, pp. 1–6, September 2011.
- [31] H. Zhu, G. Leus, and G. B. Giannakis, "Sparsity-cognizant total least-squares for perturbed compressive sampling," *IEEE Trans. on Signal Processing*, vol. 59, no. 5, pp. 2002–2016, May 2011.
- [32] K. Sun, Y. Liu, H. Meng, and X. Wang, "Adaptive sparse representation for source localization with gain/phase errors," *Sensors*, vol. 11, no. 5, pp. 4780–4793, 2011.
- [33] Y. Zhang, Q. Wan, A. Huang and W. Yang, "Observation data based DOA estimation with uncalibrated antenna array in perspective of sparse solution finding," *IEEE Region 10 Conference (TENCON)*, pp. 1–4, November 2007.
- [34] D. L. Donoho, "Compressed sensing," *IEEE Trans. on Information Theory*, vol. 52, no. 4, pp. 1289–1306, April 2006.

- [35] A. M. Bruckstein, D. L. Donoho, and M. Elad, “From sparse solutions of systems of equations to sparse modeling of signals and images,” *Society for Industrial and Applied Mathematics (SIAM)*, vol. 51, no. 1, pp. 34–81, February 2009.
- [36] K. Huang and S. Aviyente, “Sparse signal representation for signal classification,” *Advances in Neural Information Processing Systems*, 2006.
- [37] Y. Saad, “Iterative methods for sparse linear systems, 2E,” *Society for Industrial and Applied Mathematics (SIAM)*, 2003.
- [38] M. Lai, “On sparse solutions of underdetermined linear systems,” *University of Georgia*, January 2009.
- [39] Y. Tsaig, “Sparse solutions of underdetermined linear systems: algorithms and applications,” *PhD Dissertation, Stanford University*, 2007.
- [40] S. F. Cotter, B. D. Rao, K. Engan, and K. Kreutz-Delgado, “Sparse solutions to linear inverse problems with multiple measurement vectors,” *IEEE Trans. on Signal Processing*, vol. 53, no. 7, pp. 2477–2488, July 2005.
- [41] J. Adler, B. D. Rao, and K. Kreutz-Delgado, “Comparison of basis selection methods,” *Proc. of Asilomar Conference on Signals, Systems and Computers*, vol. 1, pp. 252–257, November 1996.
- [42] L. Mancera and J. Portilla, “L0-norm-based sparse representation through alternate projections,” *Proc. of IEEE International Conference on Image Processing (ICIP)*, pp. 2089–2092, October 2006.
- [43] D. L. Donoho and M. Elad, “Optimally sparse representation in general (non-orthogonal) dictionaries via  $\ell_1$  minimization,” *Proc. of National Academy of Science*, vol. 100, no. 5, pp. 2197–2002, March 2003.

- [44] J. A. Tropp and A. C. Gilbert, “Signal recovery from random measurements via orthogonal matching pursuit,” *IEEE Trans. on Information Theory*, vol. 53, no. 12, pp. 4655–4666, December 2007.
- [45] D. M. Malioutov, M. Cetin, and A. S. Willsky, “Optimal sparse representations in general overcomplete bases,” *Proc. of IEEE International Conference on Acoustics, Speech, and Signal Processing, (ICASSP)*, vol. 2, pp. 793–6, May 2004.
- [46] B. K. Natarajan, “Sparse approximate solutions to linear systems,” *Society for Industrial and Applied Mathematics (SIAM)*, vol. 24, pp. 227–234, 1995.
- [47] R. G. Baraniuk, “Compressive Sensing,” *IEEE Signal Processing Magazine*, vol. 24, no. 4, pp. 118–121, July 2007.
- [48] S. G. Kargl, K. L. Williams, T. M. Marston, J. L. Kennedy, and J. L. Lopes, “Acoustic response of unexploded ordnance (UXO) and cylindrical targets,” *Proc. of MTS/IEEE Oceans*, pp. 1–5, September 2010.
- [49] J. A. Bucaro, B. H. Houston, M. Saniga, L. R. Dragonette, T. Yoder, S. Dey, L. Kraus, and L. Carin, “Broadband acoustic scattering measurements of underwater unexploded ordnances,” *Journal of Acoustic Society of America*, vol. 123, pp. 738–746, 2008.
- [50] K. L. Williams, S. G. Kargl, E. I. Thorsos, D. S. Burnett, J. L. Lopes, M. Zampolli, and P. L. Marston, “Acoustic scattering from a solid aluminum cylinder in contact with a sand sediment: Measurements, modeling and interpretations,” *Journal of Acoustic Society of America*, vol. 127, pp. 3356–3371, 2010.
- [51] S. G. Kargl, K. L. Williams, E. I. Thorsos, and J. L. Lopes, “Bistatic synthetic aperture sonar measurements and preliminary analysis,” *Boundary Influences in High Frequency Shallow Water Acoustics*, pp. 137–143, September 2005.

- [52] S. G. Schock and J. Wulf, "Imaging performance of BOSS using SAS processing," *Proc. of MTS/IEEE Oceans*, pp. 1–5, September 2006.
- [53] S. G. Schock, A. Tellier, J. Wulf, J. Sara, and M. Ericksen, "Buried object scanning sonar," *IEEE Journal of Oceanic Engineering*, vol. 26, no. 4, pp. 677–689, October 2001.
- [54] S. G. Schock and J. Wulf, "Buried object scanning sonar for AUVs," *Proc. of MTS/IEEE Oceans*, vol. 1, pp. 494–499, September 2003.
- [55] S. G. Schock, J. Wulf, G. Quentin, and J. Sara, "Synthetic aperture processing of buried object scanning sonar data," *Proc. of MTS/IEEE Oceans*, pp. 2236–2241, 2005.
- [56] M. Yamada, J. Cartmill, and M. R. Azimi-Sadjadi, "Buried underwater target classification using the new BOSS and canonical correlation decomposition feature extraction," *Proc. of MTS/IEEE Oceans*, pp. 589–596, 2005.
- [57] G.I. Allen and G. Sulzberger and J.T. Bono and J.S. Pray and T.R. Clem, "Initial Evaluation of the New Real-time Tracking Gradiometer Designed for Small Unmanned Underwater Vehicles," *Proc. of MTS/IEEE Oceans*, vol. 3, pp. 1956–1962, 2005.
- [58] Z. Wang and P. Willett, "All-Purpose and Plug-In Power-Law Detectors for Transient Signals," *IEEE Trans. on Signal Processing*, vol. 49, no. 11, pp. 2454–2466, November 2001.
- [59] R. N. Challa and S. Shamsunder, "High-order subspace-based algorithms for passive localization of near-field sources," *Proc. of Asilomar Conference on Signals, Systems and Computers*, vol. 2, pp. 777–781, November 1995.
- [60] Y. Wu, H. C. So, C. Hou, and J. Li, "Passive localization of near-field sources with a polarization sensitive array," *IEEE Trans. on Antennas and Propagation*, vol. 55, no. 8, pp. 2402–2408, August 2007.

- [61] H. He, Y. Wang, and J. Saillard, "A high resolution method of source localization in near-field by using focusing technique," *Proc. of European Signal Processing Conference (EUSIPCO)*, August 2008.
- [62] W. Zeng, X. Li, H. Zou, and X. Zhang, "Near-field multiple source localization using joint diagonalization," *Elsevier B. V. Signal Processing*, vol. 89, pp. 232–238, 2009.
- [63] S. Shahbazpanahi, S. Valaee, and M. H. Bastani, "Distributed source localization using ESPRIT algorithm," *IEEE Trans. on Signal Processing*, vol. 49, no. 10, pp. 2169–2178, October 2001.
- [64] R. Roy, A. Paulraj, and T. Kailath, "ESPRIT-A subspace rotation approach to estimation of parameters of cisoids in noise," *IEEE Trans. on Acoustics, Speech and Signal Processing*, vol. 34, no. 5, pp. 1340–1342, October 1986.
- [65] Y. Han, J. Wang, and X. Song, "Generalized ESPRIT algorithm based on Schur-Hadamard product for DOA estimation of general-rank signals," *International Journal of Information and System Sciences*, vol. 4, no. 3, pp. 362–373, 2008.
- [66] M. R. Azimi-Sadjadi, A. Pezeshki, L. Scharf, and M. Hohil, "Wideband DOA estimation algorithms for multiple target detection and tracking using unattended acoustic sensors," *Proc. of SPIE Defense and Security Symposium, Unattended Ground Sensors*, vol. 5417, pp. 1–11, April 2004.
- [67] H. Hung and M. Kaveh, "Focusing matrices for coherent signal-subspace processing," *IEEE Trans. on Acoustics, Speech and Signal Processing*, vol. 36, no. 8, pp. 1272–1281, August 1988.
- [68] J. Cao, Z. Liu, and Y. Xu, "New algorithm requiring no preprocessing for wideband DOA estimation," *Proc. of International Conference on Signal Processing (ICSP)*, pp. 394–397, October 2008.

- [69] M. R. Azimi-Sadjadi, A. Pezeshki, and N. Roseveare, "Wideband DOA estimation algorithms for multiple moving sources using unattended acoustic sensors," *IEEE Trans. on Aerospace and Electronic Systems*, vol. 44, no. 4, pp. 1585–1599, October 2008.
- [70] H. Wang and M. Kaveh, "Coherent signal-subspace processing for the detection and estimation of angles of arrival of multiple wide-band sources," *IEEE Trans. on Acoustics, Speech and Signal Processing*, vol. 33, no. 4, pp. 823–831, August 1985.
- [71] J. Krolik, "Focused wideband array processing for spatial spectral estimation," *Advances in spectrum analysis and array processing, Prentice-Hall*, vol. II, 1991.
- [72] Y. C. Eldar, P. Kuppinger, and H. Bolcskei, "Block-sparse signals: uncertainty relations and efficient recovery," *IEEE Trans. on Signal Processing*, vol. 58, no. 6, pp. 3042–3054, June 2010.
- [73] X. S. Guo, Q. Wan, B. Wu and W. L. Yang, "Parameters localisation of coherently distributed sources based on sparse signal representation," *The Institute of Engineering and Technology, Radar and Sonar Navigation*, vol. 1, no. 4, pp. 261–265, March 2007.